

Light-Metal-Based Nanostructures for Energy and Biomedical Applications

Guest Editors: Jianxin Zou, Craig Buckley, Huaiyu Shao, Gang Ji, and Kemin Zhang





Light-Metal-Based Nanostructures for Energy and Biomedical Applications

Light-Metal-Based Nanostructures for Energy and Biomedical Applications

Guest Editors: Jianxin Zou, Craig Buckley, Huaiyu Shao, Gang Ji, and Kemin Zhang



Copyright © 2013 Hindawi Publishing Corporation. All rights reserved.

This is a special issue published in “Journal of Nanomaterials.” All articles are open access articles distributed under the Creative Commons Attribution License, which permits unrestricted use, distribution, and reproduction in any medium, provided the original work is properly cited.

Editorial Board

Katerina Aifantis, Greece
Nageh K. Allam, USA
Margarida Amaral, Portugal
Xuedong Bai, China
Enrico Bergamaschi, Italy
Theodorian Borca-Tasciuc, USA
C. Jeffrey Brinker, USA
Christian Brosseau, France
Xuebo Cao, China
Sang-Hee Cho, Republic of Korea
Shafiul Chowdhury, USA
Cui ChunXiang, China
Miguel A. Correa-Duarte, Spain
Shadi A. Dayeh, USA
Ali Eftekhari, USA
Claude Estournes, France
Alan Fuchs, USA
Lian Gao, China
Russell E. Gorga, USA
Hongchen Chen Gu, China
Mustafa O. Guler, Turkey
John Zhanhu Guo, USA
Smrati Gupta, Germany
Michael Harris, USA
Zhongkui Hong, USA
Michael Z. Hu, USA
David Hui, USA
Y.-K. Jeong, Republic of Korea
Sheng-Rui Jian, Taiwan
Wanqin Jin, China
Rakesh K. Joshi, India
Zhenhui Kang, China

Fathallah Karimzadeh, Iran
Do Kyung Kim, Republic of Korea
Kin Tak Lau, Australia
Burtrand Lee, USA
Benxia Li, China
Jun Li, Singapore
Shijun Liao, China
Gong Ru Lin, Taiwan
J.-Y. Liu, USA
Jun Liu, USA
Tianxi Liu, China
Songwei Lu, USA
Daniel Lu, China
Jue Lu, USA
Ed Ma, USA
Gaurav Mago, USA
Sanjay R. Mathur, Germany
Nobuhiro Matsushita, Japan
A. McCormick, USA
Vikas Mittal, UAE
Weihai Ni, Germany
Sherine Obare, USA
Edward Andrew Payzant, USA
Kui-Qing Peng, China
Anukorn Phuruangrat, Thailand
Ugur Serincan, Turkey
Huaiyu Shao, Japan
Donglu Shi, USA
Suprakas Sinha Ray, South Africa
Vladimir Sivakov, Germany
Marinella Striccoli, Italy
Bohua Sun, South Africa

Saikat Talapatra, USA
Nairong Tao, China
Titipun Thongtem, Thailand
Somchai Thongtem, Thailand
Valeri P. Tolstoy, Russia
Tsung-Yen Tsai, Taiwan
Takuya Tsuzuki, Australia
Raquel Verdejo, Spain
Mat U. Wahit, Malaysia
Shiren Wang, USA
Yong Wang, USA
Cheng Wang, China
Zhenbo Wang, China
Jinquan Wei, China
Ching Ping Wong, USA
Xingcai Wu, China
Guodong Xia, Hong Kong
Zhi Li Xiao, USA
Ping Xiao, UK
Shuangxi Xing, China
Yangchuan Xing, USA
N. Xu, China
Doron Yadlovker, Israel
Ying-Kui Yang, China
Khaled Youssef, USA
Kui Yu, Canada
Haibo Zeng, China
Tianyou Zhai, Japan
Renyun Zhang, Sweden
Yanbao Zhao, China
Lianxi Zheng, Singapore
Chunyi Zhi, Japan

Contents

Light-Metal-Based Nanostructures for Energy and Biomedical Applications, Jianxin Zou, Craig Buckley, Huaiyu Shao, Gang Ji, and Kemin Zhang
Volume 2013, Article ID 203542, 2 pages

Formation of Surface Nano- and Textured Austenite Induced by Pulsed Electron Beam Irradiation under Melting Mode, K. M. Zhang and J. X. Zou
Volume 2013, Article ID 503256, 8 pages

Effect of Nano-Magnesium Hydride on the Thermal Decomposition Behaviors of RDX, Miao Yao, Liping Chen, Guoning Rao, Jianxin Zou, Xiaoqin Zeng, and Jinhua Peng
Volume 2013, Article ID 864985, 8 pages

Applied Pressure on Altering the Nano-Crystallization Behavior of $\text{Al}_{86}\text{Ni}_6\text{Y}_{4.5}\text{Co}_2\text{La}_{1.5}$ Metallic Glass Powder during Spark Plasma Sintering and Its Effect on Powder Consolidation, X. P. Li, M. Yan, G. Ji, and M. Qian
Volume 2013, Article ID 101508, 6 pages

Surface Nanocrystallization of 3Cr13 Stainless Steel Induced by High-Current Pulsed Electron Beam Irradiation, Zhiyong Han, Le Ji, Jie Cai, Hui Zou, Zhiping Wang, and Qingfeng Guan
Volume 2013, Article ID 603586, 6 pages

Nanostructure Formations and Improvement in Corrosion Resistance of Steels by Means of Pulsed Electron Beam Surface Treatment, K. M. Zhang, J. X. Zou, and T. Grosdidier
Volume 2013, Article ID 978568, 8 pages

Antibacterial TiO_2 Coating Incorporating Silver Nanoparticles by Microarc Oxidation and Ion Implantation, Peng Zhang, Zhiguo Zhang, and Wei Li
Volume 2013, Article ID 542878, 8 pages

Thermodynamic Property Study of Nanostructured Mg-H, Mg-Ni-H, and Mg-Cu-H Systems by High Pressure DSC Method, Huaiyu Shao, Gongbiao Xin, Xingguo Li, and Etsuo Akiba
Volume 2013, Article ID 281841, 7 pages

Low Temperature Synthesis of Hexagonal Shaped $\alpha\text{-Al}_2\text{O}_3$ Using a Solvothermal Method, A-Young Kim, Hyun Soo Kim, No-Kuk Park, Tae Jin Lee, Won Gun Lee, Heun Duk Kim, Jun Woo Park, and Misook Kang
Volume 2012, Article ID 907503, 7 pages

Study on Nanostructures Induced by High-Current Pulsed Electron Beam, Bo Gao, Yi Hao, Ganfeng Tu, and Wenyan Wu
Volume 2012, Article ID 480482, 5 pages

Preparation and Hydrogen Storage Properties of Mg-Rich Mg-Ni Ultrafine Particles, Jianxin Zou, Haiquan Sun, Xiaoqin Zeng, Gang Ji, and Wenjiang Ding
Volume 2012, Article ID 592147, 8 pages

Editorial

Light-Metal-Based Nanostructures for Energy and Biomedical Applications

Jianxin Zou,¹ Craig Buckley,² Huaiyu Shao,³ Gang Ji,⁴ and Kemin Zhang⁵

¹ National Engineering Research Center of Light Alloy Net Forming, School of Materials Science and Engineering, Shanghai Jiao Tong University, Shanghai 200240, China

² Department of Imaging and Applied Physics, Curtin University, GPO Box U 1987, Perth 6845, WA, Australia

³ International Institute for Carbon-Neutral Energy Research, Kyushu University, Japan

⁴ Unité Matériaux Et Transformations (UMET), CNRS UMR 8207, Université Lille 1, 59655 Villeneuve d'Ascq, France

⁵ School of Materials Engineering, Shanghai University of Engineering Science, Shanghai 201620, China

Correspondence should be addressed to Jianxin Zou; zoujx@sjtu.edu.cn

Received 9 April 2013; Accepted 9 April 2013

Copyright © 2013 Jianxin Zou et al. This is an open access article distributed under the Creative Commons Attribution License, which permits unrestricted use, distribution, and reproduction in any medium, provided the original work is properly cited.

Light metals, such as Li, Mg, and Ti, are now receiving increasing attention as functional materials owing to their superior functional properties for energy and biomedical applications. For example, Mg has a high hydrogen storage capacity up to 7.6 wt%, a high specific capacity as battery electrodes, and a good biocompatibility as biodegradable implants. These superior properties render the possibility of applying light-metal-based alloys/compounds in energy and biomedical industries. However, light-metal-based materials are also facing some serious disadvantages when used for energy and biomedical applications, which strongly limit their further industrial applications. In this issue, different approaches were used to create nanostructures in several light-metal-based materials in order to improve their properties.

The paper “Preparation and hydrogen storage properties of Mg-rich Mg-Ni ultrafine particles” by J. Zou et al. used an arc plasma method to prepare a Mg-rich Mg-Ni ultrafine powder. The hydrogen storage properties and the formation/decomposition of Mg_2NiH_4 in the Mg-Ni powder were carefully analyzed and discussed in detail.

The paper “Thermodynamic property study of nanostructured Mg-H, Mg-Ni-H, and Mg-Cu-H systems by high pressure DSC method” by H. Shao et al. analyzed some nanostructured Mg hydrides, such as Mg-H, Mg-Ni-H, and Mg-Cu-H using the high pressure DSC technique. A good

agreement in the thermodynamic data was obtained between DSC measurements and PCT measurements.

The paper “Effect of nano-magnesium hydride on the thermal decomposition behaviors of RDX” by M. Yao et al. has analyzed the decomposition behaviors of RDX with and without the addition of nano-Mg hydride. The change in thermodynamic data of the RDX/MgH₂ mixture was measured using DSC and ARC techniques, and mechanisms were discussed.

The paper “Applied pressure on altering the nanocrystallization behavior of $\text{Al}_{86}\text{Ni}_6\text{Y}_{4.5}\text{Co}_2\text{La}_{1.5}$ metallic glass powder during spark plasma sintering and its effect on powder consolidation” by X. P. Li et al. prepared dense bulk materials using spark plasma sintering method from metallic powders. The microstructure of the consolidated powders was analyzed by the TEM technique and nanocrystallization behaviors with regards to the applied pressure during sintering were investigated.

The paper “Low temperature synthesis of hexagonal shaped $\alpha\text{-Al}_2\text{O}_3$ using a solvothermal method” by A. Y.-Kim et al. prepared $\alpha\text{-Al}_2\text{O}_3$ particles through a solvothermal method. The change in microstructure and properties associated with the variation in pH values during preparation was carefully analyzed.

The paper “Antibacterial TiO_2 coating incorporating silver nanoparticles by microarc oxidation and ion implantation” by

P. Zhang et al. used microarc oxidation and ion implantation method to prepare TiO_2 coatings containing Ag nanoparticles on Ti. The microstructure, phase components and antibacterial property of the TiO_2 coatings were investigated.

The paper *"Nanostructure formations and improvement in corrosion resistance of steels by means of pulsed electron beam surface treatment"* by K. M. Zhang et al. reviewed the formation of nanostructures in the surface layers of some steels induced by pulsed electron beam treatment. In particular, the mechanisms of nanostructure formations and improvement in corrosion resistance of steels were discussed in detail.

The paper *"Formation of surface nano- and textured austenite induced by pulsed electron beam irradiation under melting mode"* by K. M. Zhang and J. X. Zou studied the formation of nano- and textured austenite on the D2 mould steel and NiTi alloy after the pulsed electron beam treatment. The generation of nanostructured austenite with special texture state was investigated and the related mechanisms were proposed.

The paper *"Study on nanostructures induced by high-current pulsed electron beam"* by B. Gao et al. analyzed the formation of surface nanostructures in Mg-Zn-Y and Al-Si alloys induced by pulsed electron beam irradiation. TEM and EBSD techniques were used to characterize the nanostructures and related mechanisms of nanostructure formations in these light alloys.

The paper *"Surface nanocrystallization of 3Cr13 stainless steel induced by high-current pulsed electron beam irradiation"* by Z. Han et al. investigated the surface nanocrystallization of a 3Cr13 stainless steel induced by the pulsed electron beam treatment. It was observed that the formation of nanostructures was related to the carbide dissolution, rapid melting, solidification, and high thermal stresses in the surface layers during the beam treatment.

Jianxin Zou
Craig Buckley
Huaiyu Shao
Gang Ji
Kemin Zhang

Research Article

Formation of Surface Nano- and Textured Austenite Induced by Pulsed Electron Beam Irradiation under Melting Mode

K. M. Zhang¹ and J. X. Zou^{2,3}

¹ School of Materials Engineering, Shanghai University of Engineering Science, Shanghai 201620, China

² Shanghai Engineering Research Center of Mg Materials and Applications & National Engineering Research Center of Light Alloy Net Forming, Shanghai Jiao Tong University, Shanghai 200240, China

³ State Key Laboratory of Metal Matrix Composite & School of Materials Science and Engineering, Shanghai Jiao Tong University, Shanghai 200240, China

Correspondence should be addressed to K. M. Zhang; zhangkm@sues.edu.cn

Received 18 December 2012; Accepted 25 January 2013

Academic Editor: Gang Ji

Copyright © 2013 K. M. Zhang and J. X. Zou. This is an open access article distributed under the Creative Commons Attribution License, which permits unrestricted use, distribution, and reproduction in any medium, provided the original work is properly cited.

We report in this paper an interesting phenomenon associated with low-energy high-current pulsed electron beam (LEHCPEB) treatment: surface nanograined and textured austenite formation under the melting treatment mode. The treatment induces superfaster heating and melting followed by a rapid solidification and cooling of the material surfaces. As a result, nano-structured surface layers can be achieved quite easily. Examples of nanoaustenite formation with special texture state in the modified surface layer of AISI D2 steel and NiTi alloy will show the potential for surface nanocrystallization of materials with improved properties by LEHCPEB technique.

1. Introduction

Recently, the application of energetic beams such as ion, electron, laser, and plasma has been of increasing interest to modify the surface of metallic materials [1–3]. The main feature of these pulsed systems lies in their high power density of 10^9 – 10^{12} W/cm² acting at the target surface within short durations. Among these pulsed beam techniques, the low-energy high-current pulsed electron beam (LEHCPEB) is relatively new [3, 4]. The simplicity and reliability are the advantages of this technique over pulsed laser and ion beam treatments, with potential industrial applications [3]. The high-density electron pulses of short durations induce dynamic temperature fields in the surface layers, leading to the superfaster heating, possible melting, and even evaporation. This is followed by a rapid solidification and cooling of the material surface. As a result, nonequilibrium microstructures, such as supersaturated solid solution, nanosized grain, and even amorphous phase formations, can be achieved in the resolidified layer. In addition, a dynamic stress field is

formed that causes intense deformation in the material sub-layers [5]. These mechanisms can generate a surface layer with improved physical, chemical, and strength properties that are often unattainable with conventional surface treatment techniques [3, 4].

During the past few decades, nanostructured materials have been studied extensively due to the fact that they have many advantages over conventional coarse-grained materials [6]. Especially, nanoaustenization has long been the objective of metallurgists to achieve combined high toughness of the austenite phase and high strength of the nanostructure. Rapid solidification and severe plastic deformation may be two alternative candidates for such a purpose. In some previous works, fine structured austenite steels were obtained by various solidification-related techniques, such as thermal spray, melt spinning, and laser treatment with the aim of producing the so-called “super steel” high strength steel with high ductility [7–9]. However, fine austenitic steel with a single phase structure is not achieved below 400 nm yet due to many factors concerning difficulties of preparation

techniques and designing of fabrication route. Severe plastic deformation methods, such as equal channel angular processing and mechanical attrition treatment, are known to be able to produce nanostructured materials with grain size down to several nm [10, 11]. However, austenite is usually metastable; that is, it tends to transform into martensite. For example, by using repeated cold rolling and equal channel angle processing, austenitic stainless steels can be nanocrystallized [7, 8], but the final microstructure always presents a mixture of martensite and austenite due to the strain-induced martensitic transformation during these processing. Further high-temperature annealing is necessary to revert the martensite to austenite. As a side effect, the size of the austenite grains will increase to micrometer size at the same time.

In many cases, the nature of the material surface is of major importance, in particular for fatigue, corrosion, and wear resistance properties which are of interests for industrial applications. Therefore, instead of producing bulk nanostructured materials, nanocrystallization of the surface can be an optimum alternative [10–12]. K. Lu and J. Lu first proposed the concept of surface nanocrystallization of materials through chemical, physical, and mechanical methods [10]. By using mechanical attrition treatment, they obtained nanostructured surface layers having better mechanical and chemical properties on different metallic materials [11]. The purpose of the present work is to show the surface nanoaustenite formations in metallic materials induced by the LEHCPEB treatment.

2. Experimental Procedure

2.1. Starting Materials. Two kinds of materials were selected to be treated by LEHCPEB, a cold worked die steel (AISI D2) and an NiTi shape memory alloy. The chemical composition of the D2 steel is C 1.4–1.6200 wt%, Cr 11–13 wt%, Mo 0.7–1.2 wt%, V ~1 wt%, Mn 0.6 wt%, Si 0.6 wt%, Fe balance. The D2 steel samples were austenitized at 1020°C for 30 min followed by water quenching [13]. The steel was subsequently tempered at 200°C for 3 hours. The above treatment procedure results in an initial structure of mixed carbides (Cr_7C_3 type) and tempered martensite. The as-received Ni(50.6 at%)Ti shape memory alloy was hot rolled at 750°C by multipasses in the form of a nearly rounded bar having a diameter of about 12 mm [14]. This processing led to a recrystallized structure having a very weak (less than two times random) and broad $\langle 110 \rangle$ fiber texture // to the rolling direction. The initial grain size was about 10–50 μm . The specimens for the LEHCPEB treatment were cut perpendicularly to the rolling axis into 2 mm thick discs. Prior to the LEHCPEB treatments, the disc surfaces were polished down to 1 μm diamond paste, and the specimens were ultrasonically cleaned in acetone.

2.2. Experimental Conditions. The electron beam system used in this work is a “Nadezhda-2-” type LEHCPEB source. It can produce electron beams with the following characteristics: an electron energy of 10 to 40 keV; a pulse duration of about 1 μs ; an energy density ranging from 0.5

to 5 J/cm^2 ; and a cross-section area that can be adjusted between 10 and 50 cm^2 . The electron beam is generated at an explosive emission graphite cathode. The accelerating voltage, magnetic field intensity, and the anode-collector distance are the controlling parameters for the beam energy density. For more details about the LEHCPEB system, the readers can refer to references [3, 4]. The electron-beam treatment parameters were as follows: an accelerating voltage of 27 kV and an energy density of $\sim 2.5 \text{ J}/\text{cm}^2$. The samples investigated here were treated for 5, 10, and 20 pulses and with a pulse duration of 1.5 μs . The dwell time between each pulse was 10 s. The parameters were set so that in both cases the materials' surfaces were treated under “melting” mode, which is different from the “evaporating” mode where the surface can reach boiling point during treatment.

2.3. Microstructure and Phase Characterization. Conventional X-ray diffraction (θ - 2θ mode) was carried out with a $\text{Cu-K}\alpha$ radiation source on a SHIMADZU XRD-6000 apparatus to analyze the phase state at the sample surface. The texture analysis on D2 steel samples was carried out using a D8 Advance Bruker AXS X-ray goniometer equipped with an Eulerian cradle χ stage. The $\text{Cr-K}\alpha$ radiation was selected for the texture analysis in order to better distinguish and separate the peaks from the α and γ phases. In some cases, to limit the X-ray penetration depth and thereby investigate only the thin melted layer present at the surface, low incident beam X-ray diffraction was done with an incident angle set at 2°. A JEOL 6500F-type field emission gun scanning electron microscope (FEG-SEM) equipped with an electron backscattering diffraction (EBSD) attachment was used to observe surface morphologies and gain more information about the microstructure and texture state of the melted zone on NiTi samples. For the EBSD analysis, the SEM was operated at 15 kV with the sample tilted by 70°.

3. Results

3.1. Nano- and Textured Austenite in Irradiated D2 Steel. Figure 1(a) shows the evolution of the XRD patterns of LEHCPEB-treated D2 steel samples with the number of pulses [15]. The starting material contained two phases: ferrite (α -Fe) and carbide having the Cr_7C_3 structure. After the LEHCPEB bombardment, the XRD patterns are observed to be changed somehow dramatically. Concerning the Cr_7C_3 phase, it is clear that the carbide peaks tend to disappear after the LEHCPEB treatments. Concerning the α phase, it is interesting to note that some of the peaks in the sample treated for 5 pulses have close neighbours. A splitting of the (200) peak is usually found in newly formed martensite having sufficient amount of C to reveal its quadraticity. It is interesting to note that this peak splitting is no longer observed after 25 pulses of LEHCPEB treatment. Finally, some new peaks are present in the XRD patterns. They were verified to be from the γ -Fe phase. The peak intensity of the γ -Fe phase increases with the number of pulses, indicating that the volume fraction of the γ phase detected by XRD increases.

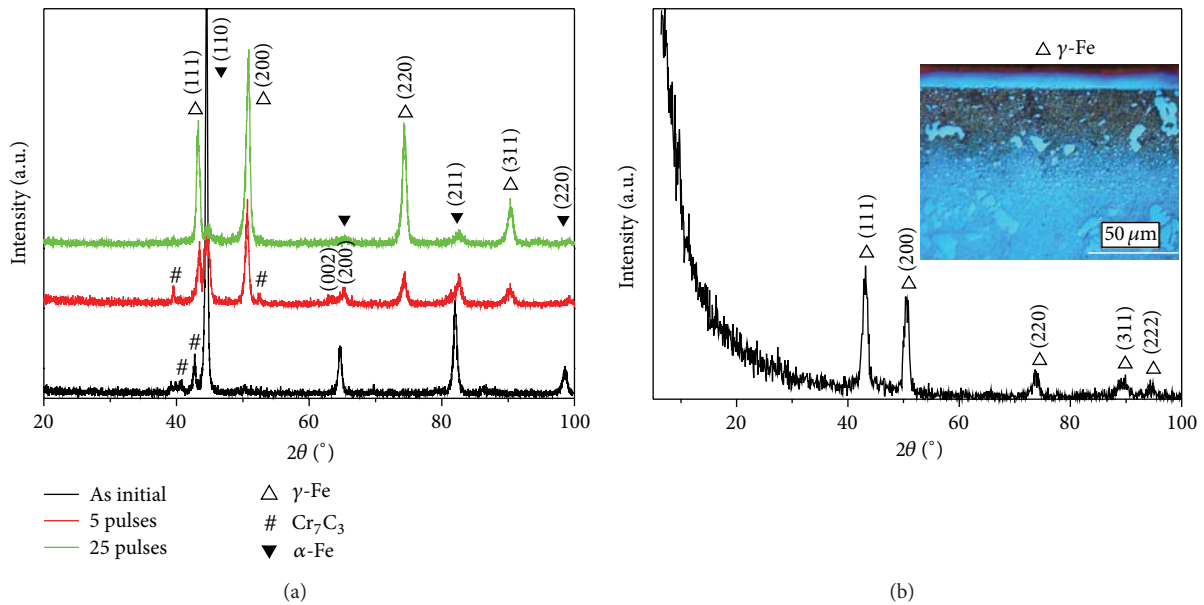


FIGURE 1: (a) XRD patterns of the untreated and treated D2 steel samples. (b) Low incident beam XRD pattern of the 25-pulsed sample; a typical cross-sectional OM picture is shown inset.

Figure 1(b) shows the low incidence beam X-ray diffractogram recorded on the sample treated for 25 pulses. It only shows the presence of the γ peaks. This indicates that the surface layer is mainly composed of the γ phase. The typical cross-sectional micrograph of the etched sample after the LEHCPEB treatment for 25 pulses is shown in the inset of Figure 1(b). The “white” layer visible on the surface, which appears with a completely different contrast from the rest of the material, corresponds to the melted layer. No carbides or grain boundaries could be observed in this layer even after deep etching. The average depth of the melted layer is 4.4 μm after 25 pulses. Below the melted layer are the heat affected zone and substrate containing large amount of carbides.

Figure 2 shows a typical SEM micrograph taken on the 5-pulsed sample. Needle-like structures are clearly observed, which tend to be grouped and connected to each other. This needle-like aspect suggests the presence of martensite. It was confirmed by EBSD measurements that those needle-like structures are martensite and the rest are austenite [15]. A high magnification SEM-FEG image of the 25 pulses treated D2 steel is shown in Figure 2(b). It reveals very fine grains or subgrains having a size of about 100–150 nm, which cover the whole surface. Figure 2(c) shows a typical TEM bright field image from the melted layer of the 25-pulsed sample. The majority of the structure consisted of the γ phase, which was directly grown from the melt and was retained down to room temperature. Although the cooling rate was as high as 10^7 K/s, the martensitic transformation was completely suppressed [16]. Such an effect is due to the increased stability of the austenite phase by grain size constraining effect and by the austenite stabilized alloying of C into the melt. Various TEM images, taken from different locations in the thin foil, showed that the cell size of the γ phase was in the range of 50–200 nm. A careful look at the micrograph in Figure 2(c) reveals also

very fine precipitates. Their size is below 10 nm. They are often present at the grain boundaries and in particular most often at triple junctions, as arrowed in Figure 2(c).

Figure 3 shows the normalized inverse pole figure corresponding to the γ phase on the 25-pulsed sample measured by XRD goniometer [14]. The intensity in the vicinity of (200) pole is about 1.8 is slowly decreasing when approaching the other two poles. This indicates the presence of a $\langle 200 \rangle$ fiber texture component parallel to the normal direction of the sample with a large spread around this ideal orientation. In addition, the higher intensity around (220) pole (about 2.1) and its fast decreasing show also the presence of a sharper $\langle 220 \rangle$ component. Although clearly depicted, these two texture components are rather weak, having maximum slightly above 2 times random. The very low intensity at (111) pole confirms the two fibers and indicates that the $\langle 220 \rangle$ and $\langle 200 \rangle$ crystallographic directions along the normal direction of the sample are created at the expense of orientations in the vicinity of $\langle 111 \rangle$.

3.2. Nano- and Textured Austenite in Irradiated NiTi Alloy. XRD analysis was also carried out on the NiTi alloy samples before and after the LEHCPEB treatments. Examples of diffractograms are shown in Figure 4. For the initial state, the observed peaks correspond to the NiTi (B2 structure) austenite phase and the NiTi_2 precipitates. After the LEHCPEB treatment with 5 pulses, peaks corresponding to the NiTi martensitic phase ($\text{B}19'$) are present. In addition, it is also clearly visible that the diffraction peaks of the NiTi_2 phase have disappeared, which is a consequence of the surface purification effect from precipitates in the surface layer [17]. However, the intensity of the peaks corresponding to NiTi martensite became weaker after 10 pulses and almost

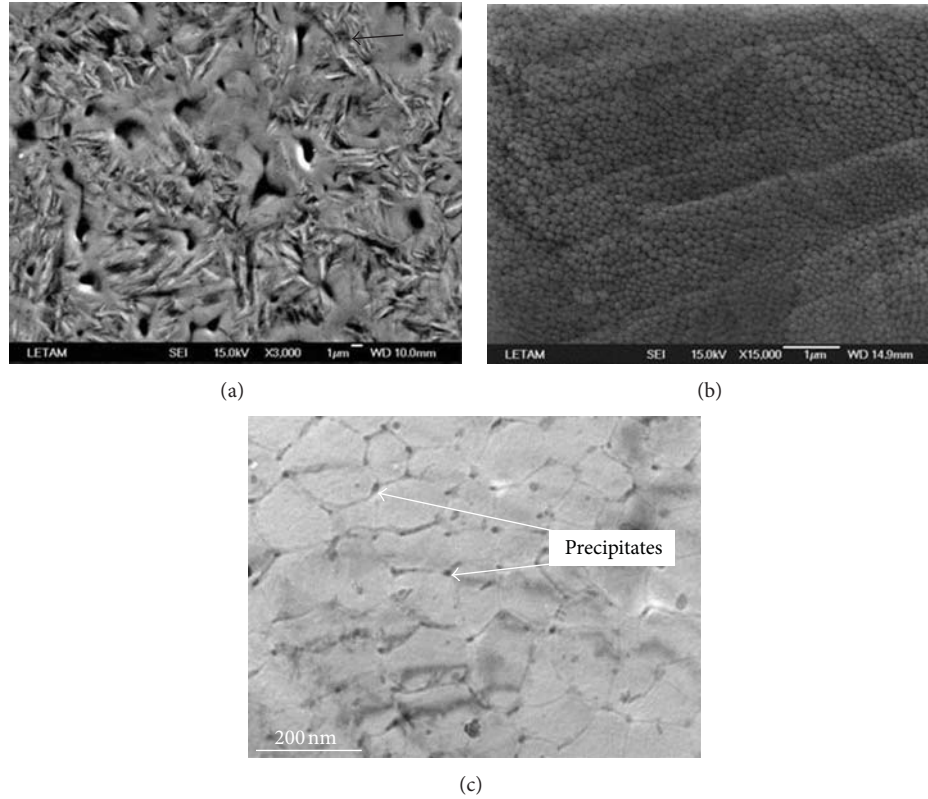


FIGURE 2: Typical SEM surface morphology on the 5-pulsed D2 sample (a) and high magnification SEI (b) surface morphologies of the sample treated with 25-pulses. Typical TEM morphology in the melted layer of the 25 pulsed sample (c).

disappeared after 20 pulses. This indicates that the fraction of martensite in the surface layer decreases with the number of pulses, a similar case to that observed on the D2 steel samples.

To gain more information about the microstructure and texture issued from the solidification of the surface melted zone, FEG-SEM observations and EBSD analysis were carried out at the top surface of the treated NiTi samples. Figure 5 shows a typical SEM micrograph of the sample LEHCPEB treated for 5 pulses under backscattering condition. Some straight bands having brighter contrast are clearly visible, close to the crater formation region. This is reasonable because the martensitic transformation in this alloy was triggered by the high stress field induced by the LEHCPEB treatment, and the stress field near crater formation region is higher due to the shock wave formation [18]. The dark spots, often located in the crater centers, are NiTi_2 precipitates, which are the initial sites for crater formations. The rest area is covered by fine grains and a network of fine shrinkage voids. Much like the 25-pulsed D2 steel sample, a high magnification SEM-FEG image of the 20 pulses treated NiTi (Figure 5(b)) reveals again very fine grains having a size of about $100\text{ nm} \sim 1\text{ }\mu\text{m}$, which cover the whole surface.

Figures 6(a) and 6(b) give a typical EBSD OIM map on the 20 pulses treated NiTi sample as well as its related pole figures. All the grains on the top surface were indexed as corresponding to the NiTi austenitic phase having the B2 structure and no martensitic phase could be indexed. Indeed,

the map in Figure 6(a) is almost completely dominated by grains having a green color (medium gray), which corresponds to grains having a $\{110\}$ plane perpendicular to the normal direction. Besides, some red-colored grains (deep gray), having their $\{100\}$ plane perpendicular to the normal direction, are also present. The pole figures (Figure 6(b)), containing rings, depict a fiber type of texture. It consists in fact of two major components: a major $\langle 110 \rangle // \text{ND}$ component to which it is associated with a very weak $\langle 100 \rangle // \text{ND}$ one. The size distribution of the austenite phase grains is shown in Figure 6(c). After the LEHCPEB treatment with 20 pulses, the rapid solidification leads to a fine grain structure with mean grain size of about 380 nm .

4. Discussion

Usually, the LEHCPEB-modified surface layer can be divided into three regions from the cross-sectional view having different depths in the treated material [19–21]: (i) a melted and rapidly solidified layer on the top surface ($\sim 1\text{--}10\text{ }\mu\text{m}$), (ii) a heat affected zone (HAZ $\sim 10\text{--}100\text{ }\mu\text{m}$), and (iii) a stress wave affected zone ($\sim 100\text{--}1000\text{ }\mu\text{m}$).

During the pulsed electron beam irradiation, the material adjacent to the zone of energy transfer is rapidly heated, leading to the formation of a nonequilibrium temperature field propagating into the material. Simultaneously, two kinds of stresses are generated, that is, the thermoelastic stress and

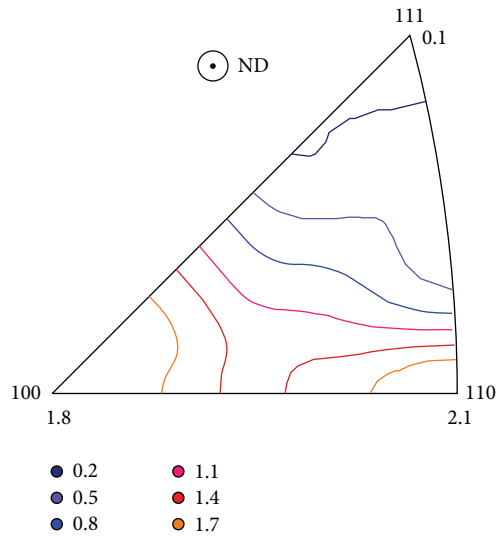


FIGURE 3: Inverse pole figure of the austenite on the 25-pulsed D2 steel sample measured by XRD.

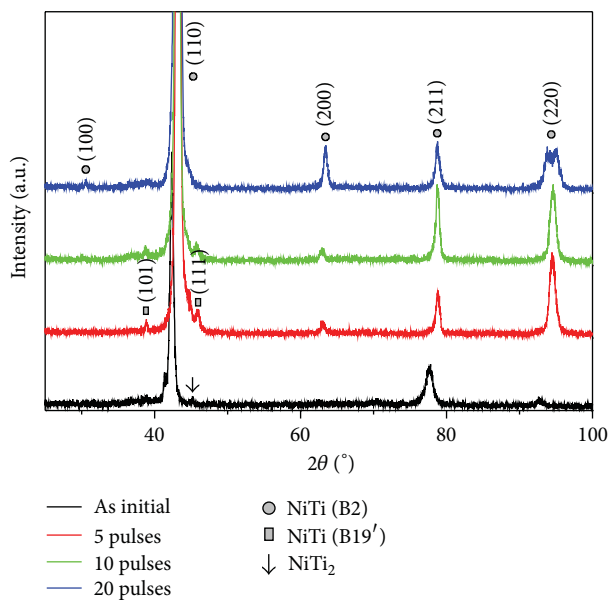


FIGURE 4: XRD patterns of the untreated and treated NiTi alloy samples.

the quasi-static thermal stress [18, 22]. When the material top surface layer is heated up, local melting can also occur preferentially below the surface at preferential sites such as second phase particles or crystallographic discontinuities. During the melting, the constrained melted pockets of material can be expelled towards the outer covering solid surface, leading to the eruptive cratering phenomena, and a recoiled impulsion will be exerted against the underlying substrate [18]. This leads to the formation of local high-gradient stress fields in the vicinity of these structural discontinuities. The stress is thus generated during the process of eruption namely, the shock thermal stress can propagate along the direction

of the electron beam in the material matrix and fade away when the eruption event finishes. When the electron beam pulse is completed, the surface layer cools down rapidly while the thermoelastic and quasi-static thermal stresses evolve temporally until the heat balance is reached in the sample [22].

The nanostructured austenite formation after LEHCPEB treatment can be mainly attributed to the rapid solidification that occurs at the surface layer. As mentioned before, the Cr and C contents in the melted layer of D2 sample increase with the number of pulses, and, thereby, the melt composition becomes closer to the eutectic point. Therefore, the melt gets stabilized, and the undercooling during rapid solidification increases [23]. This must lead to an increase in the nucleation rate within the melt with the number of pulses. In addition, it was also shown that the addition of small-sized atoms, for example, B into $\text{Ni}_{70}\text{Cu}_{30}$ alloy, can favour the grain refinement effect by reducing the crystal growth rate [23]. In this case, carbon will play the same role, as already shown in an Mg alloy [24]. Thus, the drastic grain refinement observed here with the pulse numbers must result from the combined effects of an increased nucleation rate and a lower grain growth. An interesting phenomenon found in the present work was the stabilization of austenite after the repeated actions of the beam and the rapid solidification process. This phase directly grows from the melt. Because of the very high cooling rate ($\sim 10^7$ K/s) and high thermal stress (hundreds of MPa) undergone at the surface of the sample, it is expected that the high temperature γ phase transforms into martensite undercooling. In the case of D2 steel, however, it is likely that the dissolution of the large carbide was almost complete so that the amount of C in the austenite must have significantly depressed the Ms temperature, and, consequently, the martensitic transformation was avoided. Besides, the inhibition of the martensitic transformation is also suppressed due to the ultrafine grain size of the austenite phase formed in this melted layer by the rapid solidification process [16].

In both cases, we have noticed that the phase transformation route with the number of pulses is similar. The martensitic transformation occurred only at the early stage of treatment, that is, 5 pulses. Then it was suppressed by dissolution of carbides or by the grain size constraining effect with sufficient number of pulses. Here, martensitic transformation may play an important role for the grain refining process. It can divide one grain into some separate parts and by which the grain can be refined. This process occurred repeatedly during each pulse, until the grain is fine enough that martensitic transformation cannot occur any more. The grains showed somehow an “inherent” behaviour.

Another interesting observation revealed in this work is the presence of the mixed $\langle 100 \rangle + \langle 110 \rangle$ fiber texture for the rapidly solidified D2 steel and NiTi B2 layers. Generally, a growth process is done along the thermal gradient direction following well-defined crystallographic directions which, for cubic materials, are the $\langle 100 \rangle$ directions [25–27]. The texture development can be influenced at the two stages controlling the solidification process that starts by nucleation and continues with growth. As the LEHCPEB

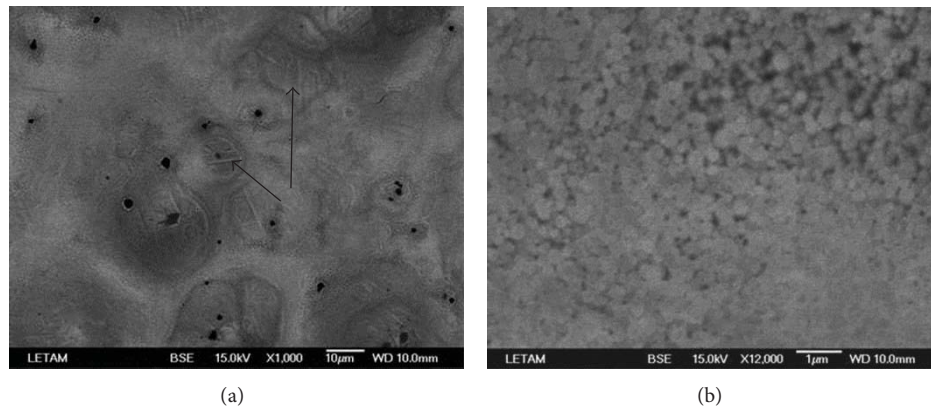


FIGURE 5: Typical BSE surface morphology on the 5-pulsed NiTi sample (a) and high magnification BSE (b) surface morphology of the sample treated with 20 pulses.

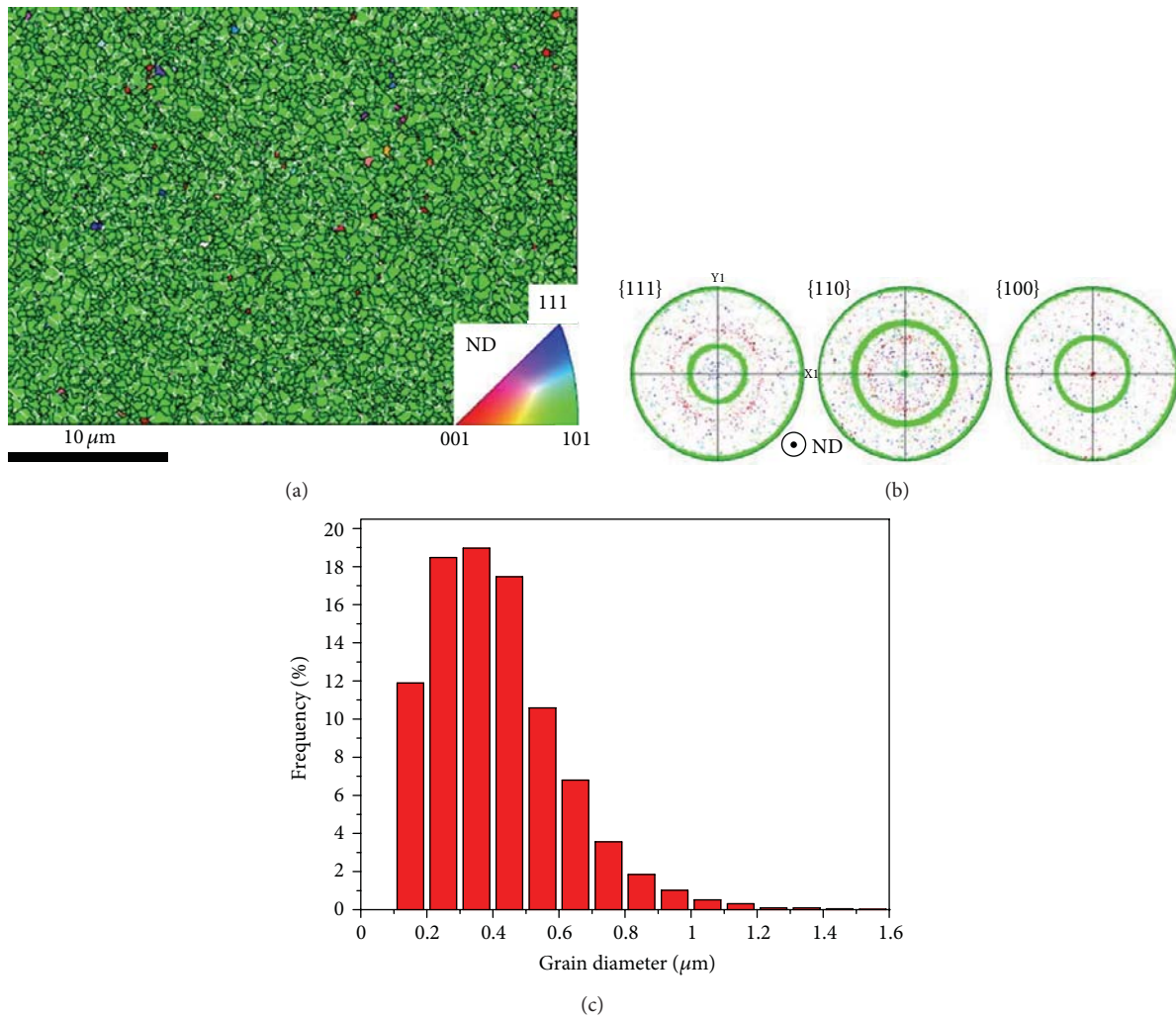


FIGURE 6: Typical EBSD OIM image of the surface 20-pulsed NiTi sample (a), its corresponding pole figures (b) and the grain size distribution (c).

process leads to resolidification onto an unmelted substrate, the nucleation stage can be affected by the orientation of the material from which the melted layer resolidifies. However, the initial D2 steel does not have a specific texture, and the initial NiTi alloy shows that only a very weak (110) fiber. This means that the growth of the austenite from melt is not an epitaxial one. Changes in the growth directions with respect to solidification conditions have been reported in transparent materials [28] as well as in Al alloys [25]. In particular, EBSD analysis has revealed that the growth direction can change from $\langle 100 \rangle$ to $\langle 110 \rangle$ in Al alloys directionally solidified in high thermal gradients [26]. This was considered to be associated with a modification of the atom attachment kinetics when supersaturation is increased. In our cases, the high growth rate together with the supersaturation of Ti in the B2 phase in our alloy and C, Cr in the D2 steel, may favour different growth directions. Indeed, further theoretical and experimental analyses concerning the LEHCPEB are required to fully understand the growth mechanisms of these grains since it is clear that their nature cannot be explained by conventional growth mechanisms.

The fine austenite structure contributes to the improved tribological properties and corrosion resistance [29–33]. It is already established that the metastable austenite can transform to martensite during wear process and thereby hardens the worn zone and improves the wear resistance. In the case of corrosion, the nanoaustenite will show better corrosion resistance by accelerating the formation of passive film on it. On the other hand, textured surface will also be a positive factor for improving corrosion resistance due to the homogenisation of grains.

5. Conclusions

This work has shown the surface nano-structured austenite with specific texture state induced by LEHCPEB irradiation in melting mode through the examples of modified surface layers of AISI D2 steel and NiTi shape memory alloy. In both cases, nanograined austenite with a $\langle 100 \rangle + \langle 110 \rangle$ fiber texture is formed on the materials after sufficient number of pulses. The results gathered here show the very strong potential for surface nanocrystallization of materials with improved properties by LEHCPEB technique. The mechanisms were identified to produce nanostructures from the melted liquid by taking advantage of the rapid thermal cycle and martensitic transformation generated by the action of the LEHCPEB process.

Acknowledgments

Professor Kemin Zhang would like to acknowledge the support of the Top Discipline Plan for Mechanical Engineering of Shanghai Municipal Education Commission (YLJX12-2). This work is partially supported by the Special Foundation of the Shanghai Science and Technology Committee for Nano-Materials Research (no. 1052nm05000) and National Natural Science Foundations (nos. 51101096, 51271121). The work of Y. Cai is acknowledged.

References

- [1] A. D. Pogrebnjak, V. T. Shablya, N. V. Sviridenko, A. N. Valyaev, S. V. Plotnikov, and M. K. Kylyshkanov, "Study of deformation states in metals exposed to intense-pulsed-ion beams (IPIB)," *Surface and Coatings Technology*, vol. 111, no. 1, pp. 46–50, 1999.
- [2] M. Sorescu, "The role of magnetostriction in pulsed laser irradiation of amorphous alloys," *Journal of Alloys and Compounds*, vol. 280, no. 1-2, pp. 251–254, 1998.
- [3] D. I. Proskurovsky, V. P. Rotshtein, G. E. Ozur et al., "Pulsed electron-beam technology for surface modification of metallic materials," *Journal of Vacuum Science and Technology A*, vol. 16, no. 4, pp. 2480–2488, 1998.
- [4] C. Dong, A. Wu, S. Hao et al., "Surface treatment by high current pulsed electron beam," *Surface and Coatings Technology*, vol. 163-164, pp. 620–624, 2003.
- [5] Y. Qin, J. X. Zou, C. Dong et al., "Temperature-stress fields and related phenomena induced by a high current pulsed electron beam," *Nuclear Instruments and Methods in Physics Research Section B*, vol. 225, no. 4, pp. 544–554, 2004.
- [6] H. Gleiter, "Nanostructured materials: basic concepts and microstructure," *Acta Materialia*, vol. 48, no. 1, pp. 1–29, 2000.
- [7] M. Tokizane, K. Ameyama, and K. Takao, "Ultra-fine austenite grain steel produced by thermomechanical processing," *Scripta Metallurgica*, vol. 22, no. 5, pp. 697–701, 1988.
- [8] M. Karimi, A. Najafzadeh, A. Kermanpur, and M. Eskandari, "Effect of martensite to austenite reversion on the formation of nano/submicron grained AISI 301 stainless steel," *Materials Characterization*, vol. 60, no. 11, pp. 1220–1223, 2009.
- [9] D. Aisman, H. Jirkova, L. Kucerova, and B. Masek, "Metastable structure of austenite base obtained by rapid solidification in a semi-solid state," *Journal of Alloys and Compounds*, vol. 509, no. 1, pp. S312–S315, 2011.
- [10] K. Lu and J. Lu, "Surface nanocrystallization of metallic materials," *Journal of Materials Science & Technology*, vol. 15, no. 3, pp. 193–196, 1999.
- [11] K. Lu and J. Lu, "Nanostructured surface layer on metallic materials induced by surface mechanical attrition treatment," *Materials Science and Engineering A*, vol. 375-377, no. 1-2, pp. 38–45, 2004.
- [12] G. Stähli and C. Sturzenegger, "On the formation of austenitic boundary layers by short laser-pulse reaction with steel," *Scripta Metallurgica*, vol. 12, no. 7, pp. 617–622, 1978.
- [13] J. X. Zou, T. Grosdidier, B. Bolle, K. M. Zhang, and C. Dong, "Texture and microstructure at the surface of an AISI D2 steel treated by high current pulsed electron beam," *Metallurgical and Materials Transactions A*, vol. 38, no. 9, pp. 2061–2071, 2007.
- [14] K. M. Zhang, D. Z. Yang, J. X. Zou, T. Grosdidier, and C. Dong, "Improved in vitro corrosion resistance of a NiTi alloy by high current pulsed electron beam treatment," *Surface and Coatings Technology*, vol. 201, no. 6, pp. 3096–3102, 2006.
- [15] J. X. Zou, T. Grosdidier, K. M. Zhang, and C. Dong, "Mechanisms of nanostructure and metastable phase formations in the surface melted layers of a HCPEB-treated D2 steel," *Acta Materialia*, vol. 54, no. 20, pp. 5409–5419, 2006.
- [16] Q. P. Meng, Y. H. Rong, and T. Y. Hsu, "Nucleation barrier for phase transformations in nanosized crystals," *Physical Review B*, vol. 65, no. 17, Article ID 174118, pp. 1741181–1741187, 2002.
- [17] J. X. Zou, K. M. Zhang, C. Dong, Y. Qin, S. Hao, and T. Grosdidier, "Selective surface purification via crater eruption under pulsed electron beam irradiation," *Applied Physics Letters*, vol. 89, no. 4, Article ID 041913, 2006.

- [18] Y. Qin, J. X. Zou, C. Dong et al., "Temperature stress field and related phenomena induced by a high current pulsed electron beam," *Nuclear Instruments and Methods in Physics Research Section B*, vol. 255, no. 4, pp. 544–554, 2004.
- [19] S. Z. Hao, B. Gao, A. M. Wu et al., "Surface modification of steels and magnesium alloy by high current pulsed electron beam," *Nuclear Instruments and Methods in Physics Research Section B*, vol. 240, no. 3, pp. 646–652, 2005.
- [20] K. M. Zhang, J. X. Zou, T. Grosdidier, C. Dong, and D. Z. Yang, "Improved pitting corrosion resistance of AISI 316 L stainless steel treated by high current pulsed electron beam," *Surface and Coatings Technology*, vol. 201, no. 3–4, pp. 1393–1400, 2006.
- [21] K. M. Zhang, J. X. Zou, T. Grosdidier et al., "Mechanisms of structural evolutions associated with the high current pulsed electron beam treatment of a NiTi shape memory alloy," *Journal of Vacuum Science and Technology A*, vol. 25, no. 1, pp. 28–36, 2007.
- [22] J. X. Zou, Y. Qin, C. Dong, X. G. Wang, A. M. Wu, and S. Z. Hao, "Numerical simulation of thermal-mechanical process of high current pulsed electron beam treatment," *Journal of Vacuum Science & Technology A*, vol. 22, no. 3, pp. 545–552, 2004.
- [23] H. Jones, *Rapid Solidification of Metals and Alloys*, institution of metallurgists, London, UK, 1982.
- [24] Q. L. Jin, J. P. Eom, S. G. Lim, W. W. Park, and B. S. You, "Grain refining mechanism of a carbon addition method in a Mg-Al magnesium alloy," *Scripta Materialia*, vol. 49, no. 11, pp. 1129–1132, 2003.
- [25] S. Henry, P. Jarry, and M. Rappaz, "⟨110⟩ dendrite growth in aluminum feathery grains," *Metallurgical and Materials Transactions A*, vol. 29, no. 11, pp. 2807–2817, 1998.
- [26] T. Haxhimali, A. Karma, F. Gonzales, and M. Rappaz, "Orientation selection in dendritic evolution," *Nature Materials*, vol. 5, no. 8, pp. 660–664, 2006.
- [27] A. Sémoroz, Y. Durandet, and M. Rappaz, "EBSD characterization of dendrite growth directions, texture and misorientations in hot-dipped Al-Zn-Si coatings," *Acta Materialia*, vol. 49, no. 3, pp. 529–541, 2001.
- [28] E. Ben-Jacob and P. Garik, "The formation of patterns in non-equilibrium growth," *Nature*, vol. 343, no. 6258, pp. 523–530, 1990.
- [29] K. M. Zhang, J. X. Zou, T. Grosdidier, and C. Dong, "Crater formation induced metastable structure in an AISI D2 steel treated with a pulsed electron beam," *Vacuum*, vol. 86, no. 9, pp. 1273–1277, 2012.
- [30] J. X. Zou, K. M. Zhang, S. Z. Hao, C. Dong, and T. Grosdidier, "Mechanisms of hardening, wear and corrosion improvement of 316 L stainless steel by low energy high current pulsed electron beam surface treatment," *Thin Solid Films*, vol. 519, no. 4, pp. 1404–1415, 2010.
- [31] Y. Hao, B. Gao, G. F. Tu, H. Cao, S. Z. Hao, and C. Dong, "Surface modification of Al-12.6Si alloy by high current pulsed electron beam," *Applied Surface Science*, vol. 258, no. 6, pp. 2052–2056, 2012.
- [32] Y. Hao, B. Gao, G. F. Tu, S. W. Li, S. Z. Hao, and C. Dong, "Surface modification of Al-20Si alloy by high current pulsed electron beam," *Applied Surface Science*, vol. 257, no. 9, pp. 3913–3919, 2011.
- [33] K. M. Zhang and J. X. Zou, "Formation of ultrafine twinned austenite on a cold rolled 316 L stainless steel induced by pulsed electron beam treatment under heating mode," *Thin Solid Films*, vol. 526, pp. 28–33, 2012.

Research Article

Effect of Nano-Magnesium Hydride on the Thermal Decomposition Behaviors of RDX

Miao Yao,¹ Liping Chen,¹ Guoning Rao,¹ Jianxin Zou,² Xiaoqin Zeng,² and Jinhua Peng¹

¹ School of Chemical Engineering, Nanjing University of Science & Technology, Nanjing, Jiangsu 210094, China

² Shanghai Engineering Research Center of Magnesium Materials and Application, School of Materials Science and Engineering, Shanghai Jiao Tong University, Shanghai 200240, China

Correspondence should be addressed to Liping Chen; clp2005@hotmail.com

Received 10 December 2012; Revised 4 February 2013; Accepted 18 February 2013

Academic Editor: Kemin Zhang

Copyright © 2013 Miao Yao et al. This is an open access article distributed under the Creative Commons Attribution License, which permits unrestricted use, distribution, and reproduction in any medium, provided the original work is properly cited.

In order to improve the detonation performance of hexahydro-1,3,5-trinitro-1,3,5-triazine (RDX) explosive, additives with high heat values were used, and magnesium hydride (MgH_2) is one of the candidates. However, it is important to see whether MgH_2 is a safe additive. In this paper, the thermal and kinetic properties of RDX and mixture of RDX/ MgH_2 were investigated by differential scanning calorimeter (DSC) and accelerating rate calorimeter (ARC), respectively. The apparent activation energy (E) and frequency factor (A) of thermal explosion were calculated based on the data of DSC experiments using the Kissinger and Ozawa approaches. The results show that the addition of MgH_2 decreases both E and A of RDX, which means that the mixture of RDX/ MgH_2 has a lower thermal stability than RDX, and the calculation results obtained from the ARC experiments data support this too. Besides, the most probable mechanism functions about the decomposition of RDX and RDX/ MgH_2 were given in this paper which confirmed the change of the decomposition mechanism.

1. Introduction

Metal hydrides belong to the hydrogen storage material, which have been widely applied for energy storage carriers in recent years. However, metal hydrides are also attracting significant attention as one of the potential fuel components of energetic materials due to their peculiar properties. Metal hydrides have high activity and they can provide high heat values in the process of explosion.

In middle of 1960s, the former Soviet Union conducted the research on the application of metal hydrides for energetic materials. It was found that the metal hydrides gave off a large amount of heat when they were burning and caused relatively lower flame temperature due to the generation of light molecular weight gases. As a result, adding metal hydrides to propellants is likely to lead higher energetic density. For example, propellants containing aluminum hydride (AlH_3) have 9.8 to 39.2 N·s/kg higher specific impulses than propellants containing Be. Recently, Russia has applied it to solid propellants and fuel air explosive weapons [1].

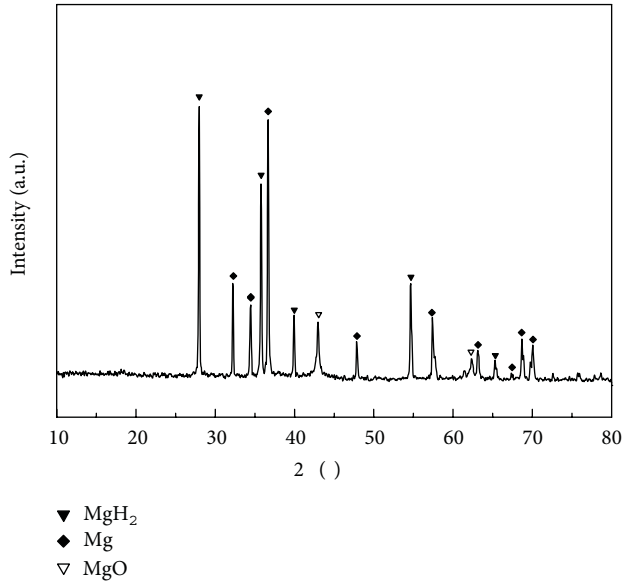
Nitrocellulose propellant composition containing AlH_3 was proposed in 1970s in USA [2]. It was also reported that adding magnesium hydride (MgH_2) in some explosives such as TNT, tetryl, and C-4 will increase the total work capacity generated by organic, noninitiating explosives [3]. Selezenev et al. [4] considered the influence of aluminum, magnesium and their hydride powders on the detonation characteristics of the compositions based on ammonium nitrate, hexahydro-1,3,5-trinitro-1,3,5-triazine (RDX), and cyclotetramethylene-tetranitramine (HMX). It concluded that the detonation velocity in the compositions with hydride powders were higher than in the composition with metal powders. Besides, MgH_2 was also applied as a pyrotechnic composition which provides improved ignition rates and increased burning time without reduction in luminous intensity [5].

From the above-mentioned researches, it can be found that metal hydrides have great potential as additive components for energetic materials. Among all the metal hydrides, MgH_2 has a high hydrogen storage capacity up to 7.6 wt%.

TABLE 1: Data of DSC analyses on RDX and RDX/MgH₂ mixture.

Sample	β	m/mg	Melting process		Decomposition process	
			$T_{\text{onset}}/^\circ\text{C}$	$T_{p1}/^\circ\text{C}$	$T_{p2}/^\circ\text{C}$	$\Delta H_d/\text{J}\cdot\text{g}^{-1}$
RDX	1	1.07	203.00	—	225.86	2179.06
	2	1.13	201.88	—	232.22	2619.00
	4	1.15	201.79	232.41	239.76	1763.61
	8	0.94	198.95	—	242.72	2558.51
RDX + 10 wt% MgH ₂	1	1.14	200.94	—	223.22	4027.00
	2	1.07	202.29	—	231.92	2512.24
	4	1.03	203.05	234.26	240.65	2048.55
	8	1.20	198.60	—	244.41	2045.80

Where β means the heating rate, the subscripts 1 and 2 are for the first peak and the second peaks respectively, T_{onset} is the initial decomposing temperature, and T_p is the peak temperature. ΔH_d is the heat release in decomposition process.

FIGURE 1: XRD pattern of MgH₂ powder.

However, as an additive, MgH₂ should be of a good compatibility with the original explosives or propellants and possess a satisfactory thermal stability. In this paper, thermal behaviors of RDX and the mixture of RDX/MgH₂ were investigated by differential scanning calorimeter (DSC) and accelerating rate calorimeter (ARC). In addition, the hazard characterizations of the mixtures were analyzed in order to ensure the safe application of MgH₂ in RDX.

2. Experimental

2.1. Materials. Nano-MgH₂ used in this paper was obtained from Shanghai Engineering Research Center of Magnesium Materials and Applications [6]. It was prepared through a DC Arc Plasma method followed by hydrogenation under high hydrogen pressure at 400°C. The details about the preparation and microstructures of the MgH₂ can be found

in the references [7]. RDX was dried at 60°C to constant weight.

2.2. Powder X-ray Diffraction. X-ray diffraction (XRD) was utilized to analyze the phase components of the hydrides. The XRD apparatus used was made by Bruker (type: D8 ADVANCE, Cu K α radiation source).

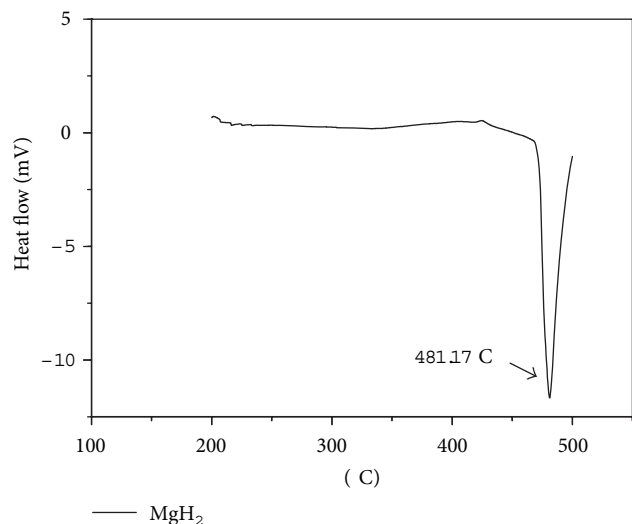
2.3. DSC Analysis. DSC is a routine tool to study the thermal stability, heat generation caused by phase transition and chemical reaction, kinetic parameters, decomposition of reactive substances, and so forth. In this paper, the DSC apparatus used was made by Mettler Toledo (type: DSC1). MgH₂ powder was tested at 10°C/min and the mixtures of RDX/MgH₂ were heated at a constant rate (1, 2, 4, 8°C/min) in nitrogen atmosphere from 25 to 500°C. The stain steel crucible was used.

2.4. ARC Analysis. ARC is an effective tool for hazards evaluation of reactive substance. Compared with DSC, ARC possesses the characteristic of larger sample quality and adiabatic experimental environment. A lightweight spherical titanium bomb was used in the experiment. The instrument used was made by Thermal Hazard Technology (type: esARC). The ARC experiments were started at ambient pressure of air. The standard ARC procedure of heat-wait-search was used [8].

3. Results and Discussion

3.1. XRD Result. The XRD pattern of MgH₂ is shown in Figure 1. Besides MgH₂, the existence of Mg and MgO was also detected in the powder.

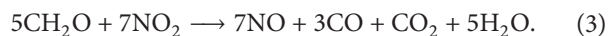
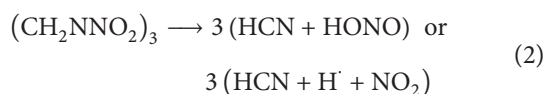
3.2. Thermal Behaviors of MgH₂ Powder. The DSC curve of MgH₂ powder is shown in Figure 2. An endothermic peak of MgH₂ appears at 481°C, which is different from the values reported in the literature [9, 10]. It is because metal hydrides release hydrogen at different temperatures due to the various surface conditions from different preparation methods. For instance, Huot et al. [9] found that MgH₂ made

FIGURE 2: DSC curve of MgH_2 powder.

by ball milling began to decompose at 396°C , while MgH_2 synthesized through a direct-hydriding method decomposed at about 287°C [10].

3.3. DSC Analyses on RDX and RDX/ MgH_2 Mixture. The DSC curves of RDX and RDX containing 10 wt% MgH_2 at different heating rates of 1, 2, 4, and $8^\circ\text{C}/\text{min}$ are shown in Figures 3(a)–3(d). The decomposition temperatures of these samples are shown in Table 1 also with the quantities of the heat release. It can be seen from the curves that adding nano- MgH_2 powder has no significant effect on the melt point of RDX. As for the decomposition process of RDX, it has at least two stages which can be observed obviously from Figures 3(a)–3(c). This result confirms to the literature research [11]. However, there is only one exothermic peak in the DSC curve of RDX at $8^\circ\text{C}/\text{min}$.

Brill and Brush [12] investigated the mechanism of thermal decomposition of RDX, HMX, and some other cyclic nitramine explosives based on the T-jump/FTIR and SMATCH/FTIR spectroscopy. The mechanism of thermal decomposition was presented that the C–N and N–N bonds break at the same time, as shown in formula of (1) and (2). It is considered that the low temperature and slow heating rate are benefit to the breakdown of C–N bonds and make the RDX go through a long decomposition in molten state which is favorable for the generation of CH_2O . Formula (1) is an exothermic reaction (-212.3 kJ/mol). In addition, high temperature and rapid heating are helpful to the breakdown of N–N bonds, and it is an endothermic reaction ($+117.2\text{ kJ/mol}$). At last, the following reaction shown in formula (3) releases a lot of heat:



Based on the above theory, different peak shapes of RDX in Figures 3(a)–3(c) can be explained. When the heating rate is slow, the breakdown of C–N bonds is the dominant reaction and this causes a gentle and slow heat release in the early stage of decomposition. Then, the reaction shown in formula (3) occurs and forms a short spike in DSC curve. On the contrary, when the heating rate increases to $8^\circ\text{C}/\text{min}$, the reaction shown in formula (2) becomes dominant and absorbs part of heat which may be due to the slight concave between 210°C to 230°C in curve (d) of RDX. Therefore, the two stages of RDX's decomposition are not observed in Figure 3(d).

As shown in the graphs, adding 10 wt% of MgH_2 has some effect on the peak shape of RDX's decomposition. Adding MgH_2 makes the shoulder peak become sharper especially at the heating rate of $1^\circ\text{C}/\text{min}$. However, the hydrogen releasing temperatures of MgH_2 used in this paper are far below the decomposition temperature of RDX. So, it can be considered that the effect on the peak shape is mainly due to the metal hydride itself but not the resolved products.

MgH_2 used in this paper was prepared through hydrogenation of Mg ultrafine powders and the high transformation-induced lattice distortion will cause intense cracks in the powder particles. As a result, lots of hydrogen atoms exist in the gaps on the surface of crystal cells [10]. Palopoli and Brill [13] proposed a opinion about the breakdown of N–N bonds of cyclic nitramine that the H atoms in the $-\text{CH}_2-$ group transfer to nearby $-\text{NO}_2$ group firstly, which results in N–N bonds' breakdown. Therefore, lots of H atoms in the gaps of MgH_2 may increase the opportunity for the interaction between H atoms and $-\text{NO}_2$ group and promote the generation of NO_2 . As a strong oxidizer, NO_2 can react with MgH_2 and provide extra heat which makes the second exothermic peak of RDX become obvious [14].

3.4. Kinetic Parameters Getting from DSC. Potential hazards always associate with the thermal behavior of energetic materials, so it is essential to evaluate the stability and carry out the decomposition kinetic. In this paper, kinetic parameters were determined using the Kissinger approach [15] and the Ozawa approach [16] in the meantime as shown in formulas (4) and (5), respectively, the results are shown in Table 2,

$$\ln\left(\frac{\beta}{T_p^2}\right) = \ln\left(\frac{RA}{E}\right) - \frac{E}{R} \frac{1}{T_p}, \quad (4)$$

$$\lg\beta = \lg\frac{AE}{RF(\alpha)} - 2.315 - 0.4567 \frac{E}{RT_p}. \quad (5)$$

As shown in Table 2, the values of E calculated by the Kissinger method are in good agreement with the values calculated by the Ozawa method. Adding 10 wt% MgH_2 decreases the activation energy of RDX from 260.57 kJ/mol to 202.74 kJ/mol . The frequency factors are also following this order. Therefore, the thermal stability lowered to a certain extent after adding MgH_2 to RDX.

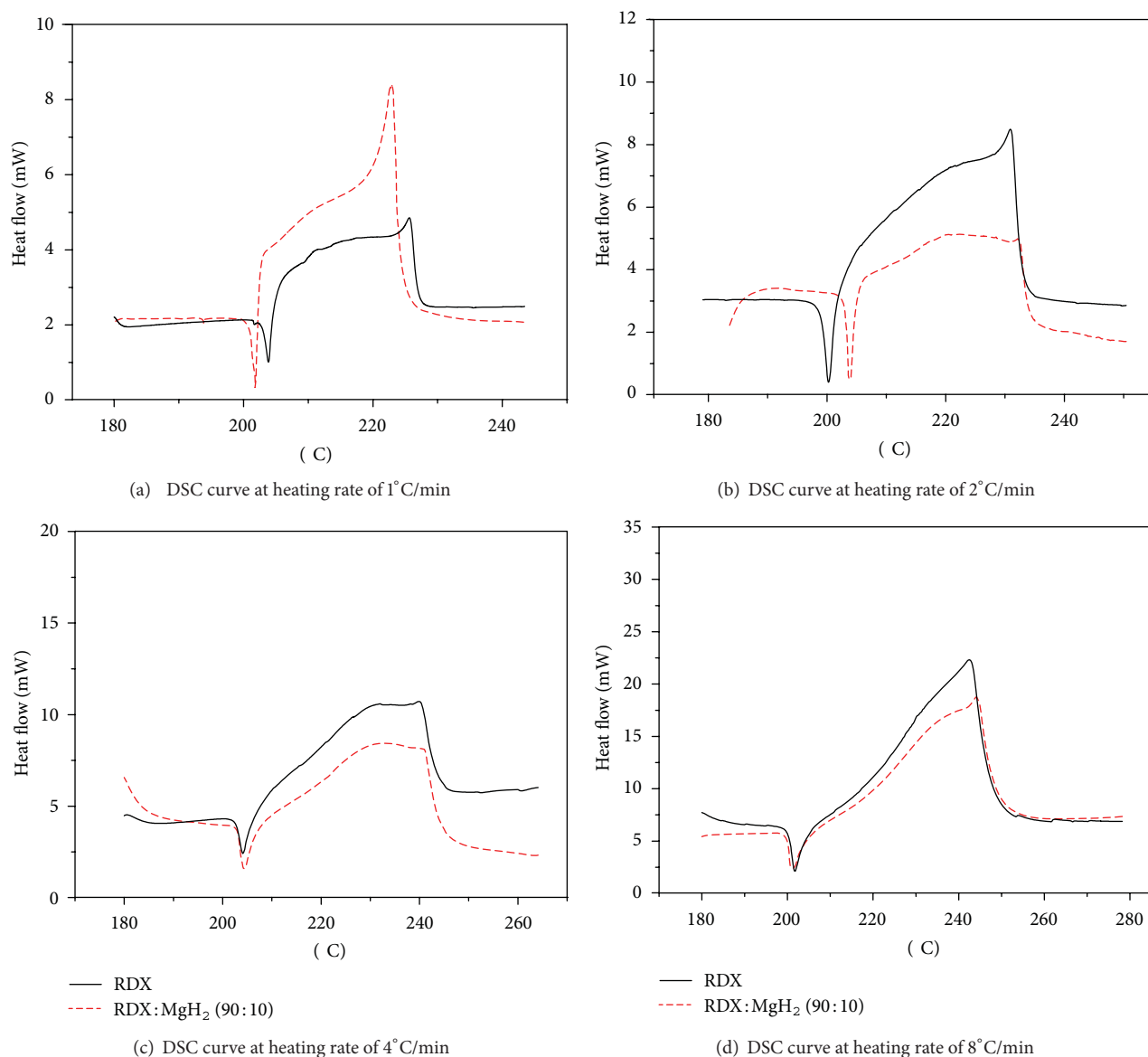
FIGURE 3: DSC curves of RDX and RDX/MgH₂ mixture at different heating rate.

TABLE 2: Kinetic parameters obtained by Kissinger and Ozawa approaches.

Sample	E (kJ/mol)	Kissinger $\ln A$ (s ⁻¹)	r^2	Ozawa E (kJ/mol)	r^2
RDX	260.57	55.93	0.98006	255.81	0.98127
RDX + 10 wt% MgH ₂	202.74	42.06	0.99331	200.80	0.99389

Where E is the activation energy, A is the frequency factor, and r^2 is the linear correlation coefficient.

3.5. ARC Results. The experimental conditions and results are listed in Table 3. The curves of temperature-time, pressure-time, self-heating-rate-temperature, and so forth are drawn in Figures 4 and 5.

The sample quantities for ARC test were smaller than usual, which was constrained by the fierce reaction of the explosive samples. As a result, the thermal inertia was big, and it may lead to higher ignited temperature and smaller

pressure. The heat release should be correct because of the heat evolution that was used to heat the titanium ball. Whereas, the data from the ARC test still had some reference significance to analyze the thermal stability of these mixtures.

Since the amount of sample is fairly small, the influence caused by a different sample weight was great. In this case, it may be improper to draw a conclusion from the data in Table 3 directly. However, it is feasible to compare the thermal

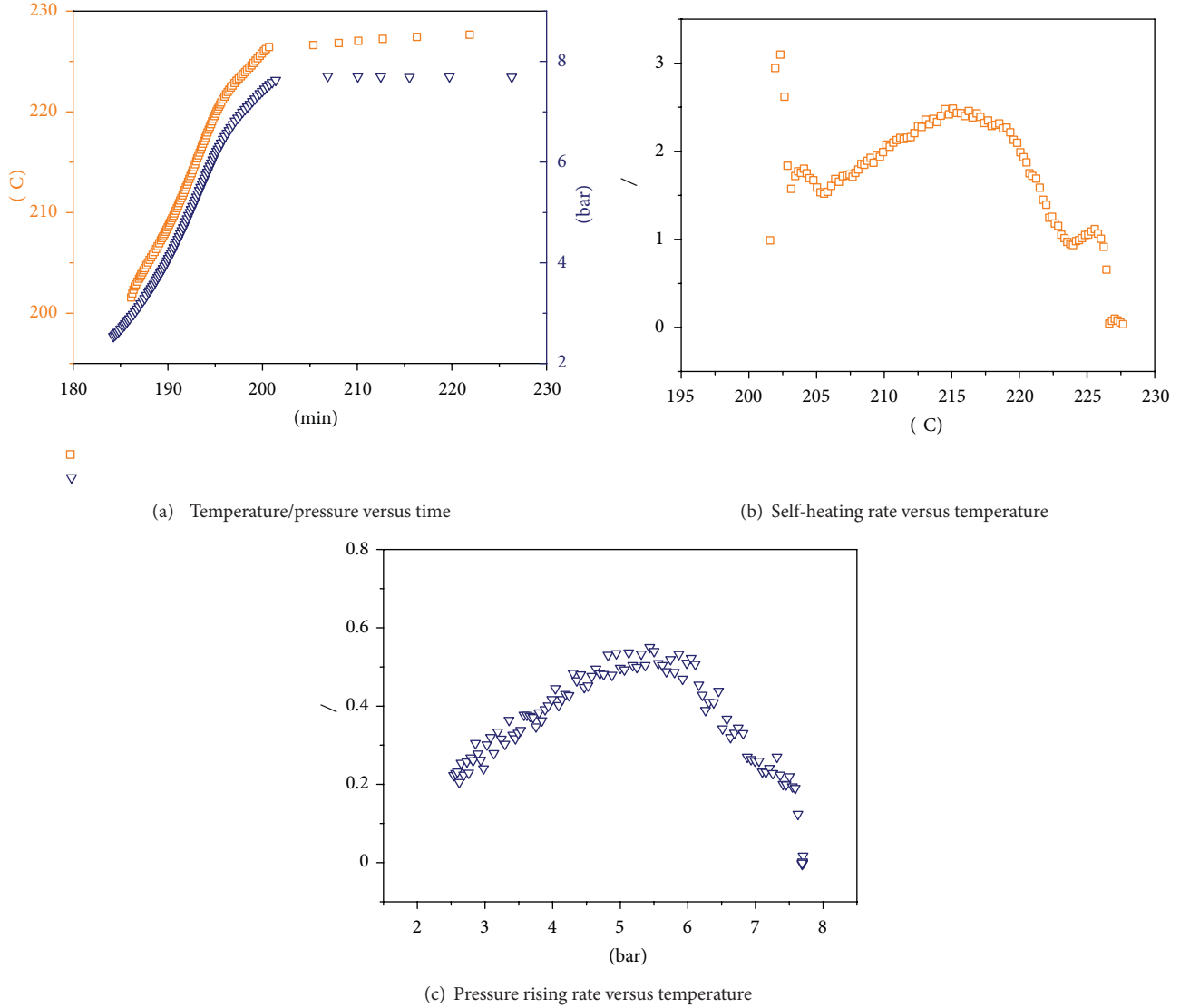


FIGURE 4: Adiabatic decomposition curves of RDX.

TABLE 3: Data of ARC analyses on RDX and RDX/MgH₂ mixture.

Sample	RDX	RDX + 5 wt% MgH ₂
M (g)	0.071	0.063
T_0 (°C)	201.569	199.220
T_f (°C)	227.653	221.791
ΔT (°C)	26.084	22.571
m_0 (°C·min ⁻¹)	0.020	0.020
m_m (°C·min ⁻¹)	2.485	1.901
T_m (°C)	215.082	219.657
P_m (bar)	7.698	6.714
ΔP (bar)	5.160	4.012

Where M is mass of sample; T_0 is the initial temperature; T_f is the final temperature; ΔT is the adiabatic temperature rise; m_0 and m_m are self-heat at T_0 and self-heat at T_f ; T_m is temperature at maximum rate; P_m is the maximum pressure; ΔP is the adiabatic pressure rise.

stability of these two samples by the kinetic parameters getting from the data.

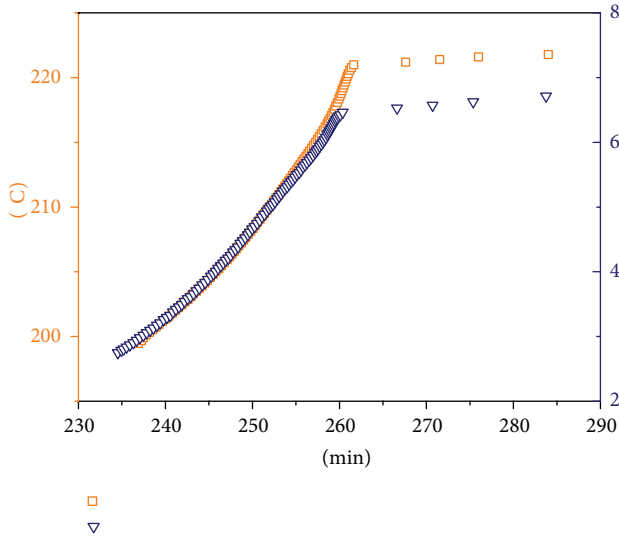
Figures 4(b) and 5(b) show the different variation of self-heating rate between RDX and RDX/MgH₂ mixture. Similar change of the variation of pressure rising rate can be observed in Figures 4(c) and 5(c). From the figures, the self-heating rate of RDX achieves its maximum at the middle of the decomposition process and drops at the high-temperature period. However, the self-heating rate of RDX/MgH₂ mixture achieve maximum at the high-temperature period as well as the pressure rising rate. That is to say, adding MgH₂ influences the decomposition process of RDX in the high temperature stage, and it is consistent with the conclusion of DSC experiments.

In this paper, the apparent activation energy of adiabatic decomposition process was calculated by a method using pressure data [17], and the following formula (6) was used:

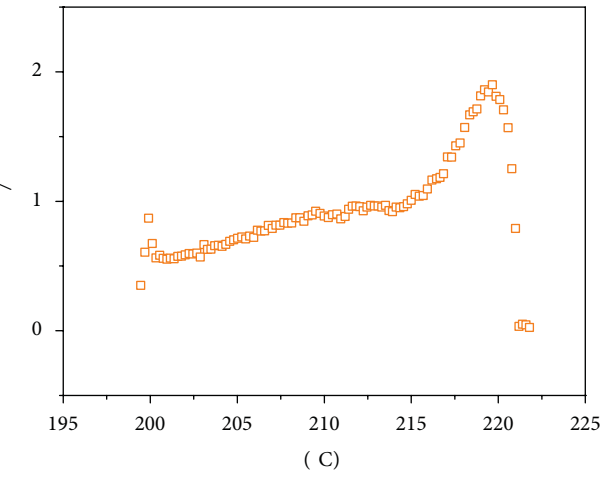
$$\ln \frac{m_p}{f((p - p_0)/\Delta p)} = \ln(A \cdot \Delta p) - \frac{E}{R} \cdot \frac{1}{T}, \quad (6)$$

TABLE 4: 29 kinetic models.

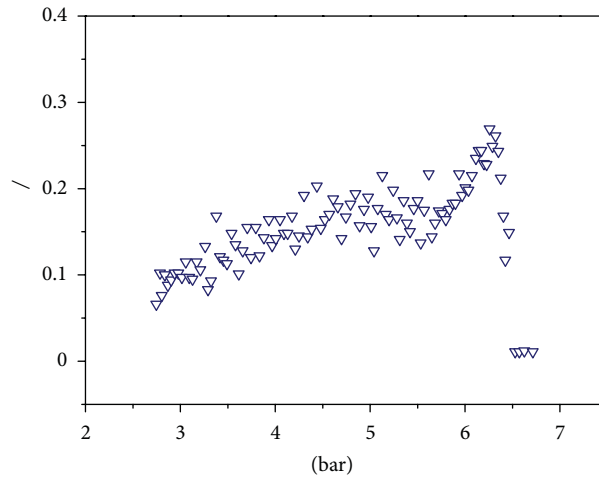
No.	$f(\alpha)$	No.	$f(\alpha)$	No.	$f(\alpha)$	No.	$f(\alpha)$
1, 2	$(1 - \alpha)^m, m = 1, 2$	9	$1/3(1 - \alpha)^{-2}$	16	$[-\ln(1 - \alpha)]^{-1}$	23	$(1/4)(1 - \alpha)[- \ln(1 - \alpha)]^{-3}$
3	1	10	$(1/4)(1 - \alpha)^{-3}$	17	$3/2(1 - \alpha)[- \ln(1 - \alpha)]^{1/3}$	24	$(3/2)[(1 - \alpha)^{-1/3} - 1]^{-1}$
4	$2(1 - \alpha)^{1/2}$	11	$(2/3)\alpha^{1/2}$	18	$2(1 - \alpha)[- \ln(1 - \alpha)]^{1/2}$	25	$3/2(1 - \alpha)^{2/3}[1 - (1 - \alpha)^{1/3}]^{-1}$
5	$2(1 - \alpha)^{3/2}$	12	$(1/2)\alpha^{-1}$	19	$3(1 - \alpha)[- \ln(1 - \alpha)]^{2/3}$	26	$6(1 - \alpha)^{2/3}[1 - (1 - \alpha)^{1/3}]^{1/2}$
6	$3(1 - \alpha)^{2/3}$	13	$2\alpha^{1/2}$	20	$4(1 - \alpha)[- \ln(1 - \alpha)]^{3/4}$	27	$4(1 - \alpha)^{1/2}[1 - (1 - \alpha)^{1/2}]^{1/2}$
7	$4(1 - \alpha)^{3/4}$	14	$3\alpha^{1/2}$	21	$(1/2)(1 - \alpha)[- \ln(1 - \alpha)]^{-1}$	28	$(3/2)(1 + \alpha)^{2/3}[(1 + \alpha)^{1/3} - 1]^{-1}$
8	$\frac{1}{2}(1 - \alpha)^{-1}$	15	$4\alpha^{1/2}$	22	$(1/3)(1 - \alpha)[- \ln(1 - \alpha)]^{-2}$	29	$(3/2)(1 - \alpha)^{4/3}[(1 - \alpha)^{-1/3} - 1]^{-1}$



(a) Temperature/pressure versus time



(b) Self-heating rate versus temperature



(c) Pressure rising rate versus temperature

FIGURE 5: Adiabatic decomposition curves of RDX + 5 wt% MgH₂.

where p is the pressure at t ; $m_p = dp/dt$; $\Delta p = p_f - p_0$ is the pressure rise; $f(\cdot)$ symbolizes the kinetic model in form of differential equation. The plot of $\ln(m_p/f((p - p_0)/\Delta p))$ versus T^{-1} should give a straight line with a slope $-E/R$ providing the kinetic model which is correctly chosen.

Different kinetic models are used to try to find the best linear fitting, from which the activation energy can be calculated. The 29 kinetic models are listed in Table 4.

By applying the 29 kinetic models in formula (6) and plot $\ln(m_p/f((p - p_0)/\Delta p))$ versus T^{-1} , the best linear fitting

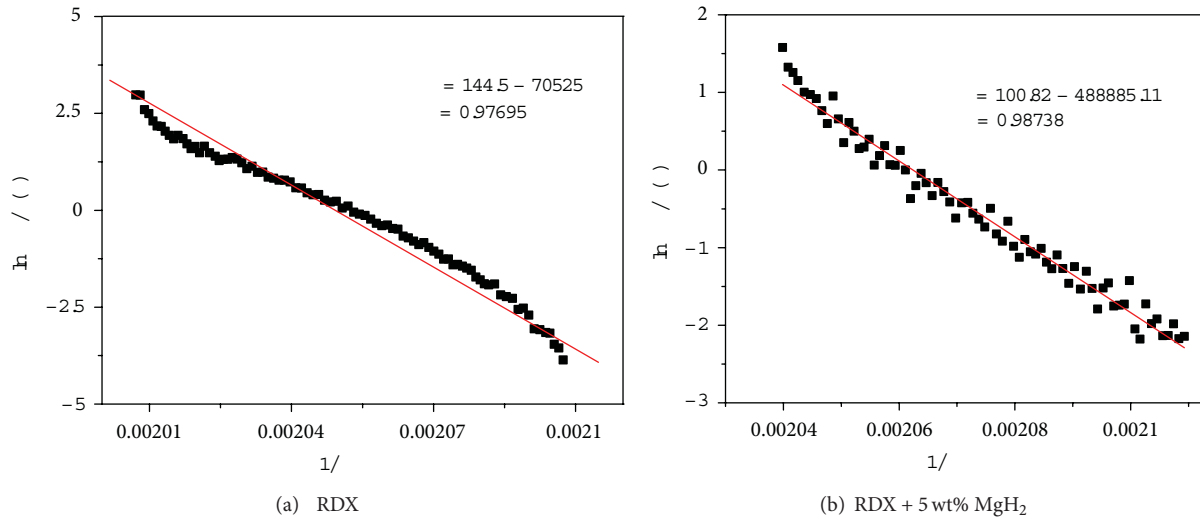


FIGURE 6: Simulating lines which have highest correlation with original data.

TABLE 5: Regression results of kinetic parameters.

Sample	E (kJ/mol)	$\ln A$ (s^{-1})	$f(\alpha)$	r
RDX	586.34	142.86	21	0.97695
RDX + 5 wt% MgH_2	406.43	99.18	2	0.98738

result can be screened. The highest correlation coefficient and the corresponding kinetic model are shown in Table 5 as well as the activation energy and frequency factor. Figure 6 shows the simulating lines which have the highest correlation with original data.

Samples used here were not exactly the same as the samples used for DSC experiment, the metal hydride content was 5 wt%. Meanwhile, the values of E and A in Table 5 are quite different from the value mentioned above. It is also due to the high thermal inertia. However, the kinetic parameters calculated from the ARC's data show the same rules as the kinetic parameters calculated from the DSC's data. Adding 5 wt% MgH_2 decreased the values of E and A obviously. Besides, the most probable mechanism function has also changed.

4. Conclusions

- (1) The addition of 10 wt% MgH_2 to RDX has no obvious or regular effect on the melt point and the initial decomposition temperature of RDX. The second exothermic peak grows dramatically after the addition of MgH_2 to RDX, and the exothermic heat quantity increases at the low heating rate.
- (2) Kinetic parameters obtained from the DSC data show that the mixture of RDX/ MgH_2 has the lower values of E and A , which means that the stability of mixture RDX/ MgH_2 is worse than RDX. The reason of the reduction may be due to the catalytic effect of the

hydrogen atoms existing in the gaps on the surface of crystal cells.

- (3) The conclusion from the ARC experiment is similar to the result obtained from DSC. The apparent activation energy of the mixture RDX/ MgH_2 is also lower than that of RDX. The most probable mechanism function changed too. Therefore, it is necessary to ensure the safety of the mixture RDX/ MgH_2 before applying it to large-scale experiment.

Acknowledgments

Professor Zou would like to thank the financial support from Research Funds for the Doctoral Program of Higher Education of China (no. 20100073120007) and from Shanghai Education Commission (no. 12ZZ017). This work is partly supported by projects from the Science and Technology Committee of Shanghai under nos. 10JC1407700, 11ZR1417600, and "Pujiang" project under no. 11PJ1406000.

References

- [1] N. E. Matzek and H. C. Roehrs, "Stabilization of light metal hydride," USP 3857922, 1974.
- [2] J. P. Flynn, G. A. Lane, and J. J. Plomer, "Nitrocellulose propellant composition containing aluminum hydride," USP 3844856, 1974.
- [3] J. R. Hradel, "Enhanced organic explosives," USP 3012868, 1961.
- [4] A. A. Selezenev, V. N. Lashkov, and V. N. Lobanov, "Effect of Al/ AlH_3 and Mg/ MgH_2 components on detonation parameters of mixed explosives," in *Proceedings of the 12th Detonation Symposium*, San Diego, Calif, USA, 2002.
- [5] J. R. Ward, " MgH_2 and $Sr(NO_3)_2$ pyrotechnic composition," USP 4302259, 1981.
- [6] J. X. Zou, X. Q. Zeng, Y. J. Ying, and W. J. Ding, "Preparation and hydrogen sorption properties of a nano-structured Mg based Mg-La-O composite," *International Journal of Hydrogen Energy*, vol. 37, pp. 13067–13073, 2012.

- [7] S. Phetsinorath, J. X. Zou, X. Q. Zeng, H. Q. Sun, and W. J. Ding, "Preparation and hydrogen storage properties of ultrafine pure Mg and Mg-Ti particles," *Transactions of Nonferrous Metals Society of China*, vol. 22, no. 8, pp. 1849–1854, 2012.
- [8] D. I. Townsend and J. C. Tou, "Thermal hazard evaluation by an accelerating rate calorimeter," *Thermochimica Acta*, vol. 37, no. 1, pp. 1–30, 1980.
- [9] J. Huot, G. Liang, S. Boily, A. Van Neste, and R. Schulz, "Structural study and hydrogen sorption kinetics of ball-milled magnesium hydride," *Journal of Alloys and Compounds*, vol. 293, pp. 495–500, 1999.
- [10] L. L. Liu, F. S. Li, C. L. Zhi, H. C. Song, and P. Li, "Effect of magnesium based hydrogen storage materials on the properties of composite solid propellant," *Chinese Journal of Energetic Materials*, vol. 17, no. 5, pp. 501–504, 2009.
- [11] Z. R. Liu, Y. Liu, X. P. Fan, F. Q. Zhao, and C. M. Yin, "Thermal decomposition of rdx and hmx part i: characteristic values of thermal analysis," *Chinese Journal of Explosives and Propellants*, vol. 27, no. 2, pp. 63–72, 2004.
- [12] T. B. Brill and P. J. Brush, "Condensed phase chemistry of explosives and propellants at high temperature: HMX, RDX and BAMO," *Philosophical Transactions of the Royal Society*, vol. 339, pp. 377–385, 1992.
- [13] S. F. Palopoli and T. B. Brill, "Thermal decomposition of energetic materials 52. On the foam zone and surface chemistry of rapidly decomposing HMX," *Combustion and Flame*, vol. 87, no. 1, pp. 45–60, 1991.
- [14] S. Bouaricha, J. Huot, D. Guay, and R. Schulz, "Reactivity during cycling of nanocrystalline Mg-based hydrogen storage compounds," *International Journal of Hydrogen Energy*, vol. 27, no. 9, pp. 909–913, 2002.
- [15] H. E. Kissinger, "Reaction kinetics in differential thermal analysis," *Analytical Chemistry*, vol. 29, no. 11, pp. 1702–1706, 1957.
- [16] T. Ozawa, "A new method of analyzing thermogravimetric data," *Bulletin of the Chemical Society of Japan*, vol. 38, no. 11, pp. 1881–1886, 1965.
- [17] X. M. Qian, L. Liu, and C. G. Feng, "Calculating apparent activation energy of adiabatic decomposition process using pressure data," *Acta Physico*, vol. 21, no. 2, pp. 134–138, 2005.

Research Article

Applied Pressure on Altering the Nano-Crystallization Behavior of $\text{Al}_{86}\text{Ni}_6\text{Y}_{4.5}\text{Co}_2\text{La}_{1.5}$ Metallic Glass Powder during Spark Plasma Sintering and Its Effect on Powder Consolidation

X. P. Li,¹ M. Yan,¹ G. Ji,² and M. Qian¹

¹ The University of Queensland, School of Mechanical and Mining Engineering, ARC Centre of Excellence for Design in Light Metals, Brisbane, QLD 4072, Australia

² Unité Matériaux et Transformations, UMR CNRS 8207, Université Lille 1, Bâtiment C6, 59655 Villeneuve d'Ascq, France

Correspondence should be addressed to M. Yan; m.yan2@uq.edu.au

Received 19 December 2012; Accepted 25 January 2013

Academic Editor: Jianxin Zou

Copyright © 2013 X. P. Li et al. This is an open access article distributed under the Creative Commons Attribution License, which permits unrestricted use, distribution, and reproduction in any medium, provided the original work is properly cited.

Metallic glass powder of the composition $\text{Al}_{86}\text{Ni}_6\text{Y}_{4.5}\text{Co}_2\text{La}_{1.5}$ was consolidated into 10 mm diameter samples by spark plasma sintering (SPS) at different temperatures under an applied pressure of 200 MPa or 600 MPa. The heating rate and isothermal holding time were fixed at 40°C/min and 2 min, respectively. Fully dense bulk metallic glasses (BMGs) free of particle-particle interface oxides and nano-crystallization were fabricated under 600 MPa. In contrast, residual oxides were detected at particle-particle interfaces (enriched in both Al and O) when fabricated under a pressure of 200 MPa, indicating the incomplete removal of the oxide surface layers during SPS at a low pressure. Transmission electron microscopy (TEM) revealed noticeable nano-crystallization of face-centered cubic (fcc) Al close to such interfaces. Applying a high pressure played a key role in facilitating the removal of the oxide surface layers and therefore full densification of the $\text{Al}_{86}\text{Ni}_6\text{Y}_{4.5}\text{Co}_2\text{La}_{1.5}$ metallic glass powder without nano-crystallization. It is proposed that applied high pressure, as an external force, assisted in the breakdown of surface oxide layers that enveloped the powder particles in the early stage of sintering. This, together with the electrical discharge during SPS, may have benefitted the viscous flow of metallic glasses during sintering.

1. Introduction

Metallic glasses (MGs) have been investigated for decades due to their intrinsically unique physical and chemical properties [1]. Al-based MGs are promising advanced materials which have attracted increasing attention for their ultrahigh specific strength and relatively low cost compared with most other MGs [2]. However, due to their low glass forming ability (GFA), fabrication of Al-based BMGs through a conventional cooling process from liquid has proved to be challenging [3–5]. The first conceptual Al-based BMG with 1 mm diameter was fabricated using a copper mold casting approach in 2009 [6] since the Al-based MG was first reported in 1988 [7] and the alloy reported [6] remains to be the best glass forming Al-based BMG to date. The slow development of Al-based BMGs in terms of their GFA impedes the potential application of these materials.

Since MG powder can be readily prepared by gas-atomization [8], powder metallurgy (PM), especially the spark plasma sintering (SPS) technique, offers an alternative to the fabrication of BMGs. Fully dense Ti-, Ni-, Cu-, and Fe-based BMGs with >10 mm diameters have been fabricated using SPS [9–12]. These MGs have much higher glass transition temperatures (T_g) [1, 3] compared to Al-based MGs and therefore can be readily consolidated at high sintering temperatures without nano-crystallization. As for Al-based BMGs, because their T_g temperatures are generally <300°C, nano-crystallization is easy to occur during SPS. Hence, few studies have succeeded in fabricating fully dense Al-based BMGs without crystallization [13–15]. On the other hand, a previous study [16] has revealed that MG powder is enveloped by an oxide layer which would inhibit viscous flow of the amorphous material for full densification. As a result, it is essential to remove this surface oxide layer to enable viscous

flow for full densification of Al-based MG powder at low temperatures.

It has been proposed [17] that the electrical discharge during SPS has a cleaning effect which can help to remove the surface oxide layers on metallic powders. In general, the higher the heating rate during SPS, the more effective the cleaning effect will be [18]. However, due to the low T_g of Al-based MGs ($<300^\circ\text{C}$), it is difficult to accurately control the temperature rise and avoid overshoot when a very high heating rate ($>40^\circ\text{C}/\text{min}$) is used. Consequently, it is necessary to consider employing other options such as the use of high pressure to assist in the breakdown of surface oxide layers that envelope the powder particles. In addition, applying high pressure during SPS is expected to favor the viscous flow between the Al-based MG powder particles for enhanced densification. No study has been reported on looking into the role of applying high pressure during the SPS of Al-based MG powder from these two perspectives.

In this study, a 10 mm diameter ($\Phi 10$ mm) $\text{Al}_{86}\text{Ni}_6\text{Y}_{4.5}\text{Co}_2\text{La}_{1.5}$ BMG was fabricated using SPS. The influence of applied pressure on the densification of $\text{Al}_{86}\text{Ni}_6\text{Y}_{4.5}\text{Co}_2\text{La}_{1.5}$ MG powder was investigated through detailed characterization of the as-sintered samples using scanning electron microscopy (SEM) and transmission electron microscopy (TEM) by focusing on selected particle-particle interfaces. The underlying reasons were discussed.

2. Experimental Procedure

Nitrogen-gas-atomized $\text{Al}_{86}\text{Ni}_6\text{Y}_{4.5}\text{Co}_2\text{La}_{1.5}$ MG powder was used. To ensure a fully amorphous state, only powder particles that are finer than $25\ \mu\text{m}$ in diameter were used based on a previous study of the powder [8, 17]. The amorphous nature of the selected powder was further confirmed by X-ray diffraction (XRD) (D/max III, CuK_α target, operated at 40 kV and 60 mA).

The surfaces of the starting powder were studied using X-ray photoelectron spectroscopy (XPS) (Kratos Axis ULTRA XPS, monochromatic Al X-ray, C 1s at 285 eV was used as a standard). XPS survey scans were taken at an analyzer pass energy level of 160 eV and carried out over the binding energy range of 1200–0 eV with 1.0 eV steps and 100 ms dwell time at each step. The base pressure in the analysis chamber was maintained in the range of 1.33×10^{-7} Pa to 1.33×10^{-6} Pa during analysis.

The SPS experiments were conducted on an SPS-1030 made by SPS SYNTEX INC, Japan. A tungsten carbide (WC) die (outer diameter 30 mm, inner diameter 10 mm, and height 20 mm) was used. The T_g temperature of the $\text{Al}_{86}\text{Ni}_6\text{Y}_{4.5}\text{Co}_2\text{La}_{1.5}$ MG powder varies with heating rate and was recorded to be 270°C at $40^\circ\text{C}/\text{min}$ in argon [8]. To avoid temperature overshoot and maximize the cleaning effect of SPS, the heating rate was fixed at $40^\circ\text{C}/\text{min}$, based on a few preliminary heating trials with the SPS machine. The isothermal holding time was fixed to be 2 min. To study the influence of sintering temperature and pressure on the densification of the $\text{Al}_{86}\text{Ni}_6\text{Y}_{4.5}\text{Co}_2\text{La}_{1.5}$ MG powder, a range of sintering temperatures was chosen, 248.5, 258.5,

TABLE 1: SPS experimental parameters used for this study.

Sintering temperature ($^\circ\text{C}$)	248.5	258.5	268.5	278.5	288.5	298.5	308.5
Pressure (MPa)	200, 600			200			
Holding time (min)				2			
Heating rate ($^\circ\text{C}/\text{min}$)				40			

268.5, 278.5, 288.5, 298.5, and 308.5°C . The pressure applied was 200 MPa or 600 MPa. Table 1 summarizes the sintering parameters used.

The sintered density was measured using the Archimedes method. The SPS-processed samples were cut, ground, and polished. They were then characterized using SEM (JEOL 7001F, accelerating voltage 15 kV and working distance 10 mm) and TEM (JEOL JEM 2100, operated at 200 kV), where the TEM samples were prepared using a precision ion polishing system (Gatan's PIPS, operated at -50°C).

3. Results and Discussion

Figure 1(a) shows the morphology of the starting powder and the XPS results are shown in Figure 1(b). Strong oxide signals are detected on the MG powder surfaces, consistent with the observations reported by Yan et al. [16]. An SPS-processed 10 mm diameter $\text{Al}_{86}\text{Ni}_6\text{Y}_{4.5}\text{Co}_2\text{La}_{1.5}$ BMG sample (4 mm in height) is shown in Figure 1(c), which was fabricated by heating the powder to 248.5°C at $40^\circ\text{C}/\text{min}$ and held at temperature for 2 min under 600 MPa. The XRD results shown in Figure 1(c) indicate that the as-sintered $\text{Al}_{86}\text{Ni}_6\text{Y}_{4.5}\text{Co}_2\text{La}_{1.5}$ BMG is essentially amorphous.

Figure 2 shows the density of SPS-processed $\text{Al}_{86}\text{Ni}_6\text{Y}_{4.5}\text{Co}_2\text{La}_{1.5}$ BMGs achieved at different sintering temperatures and pressures. Under an applied pressure of 200 MPa, the density of the BMGs increased with increasing sintering temperature from 248.5°C to 278.5°C . But further increasing the sintering temperature to 308.5°C , which is above the T_g of the alloy and also above the peak temperature for the first crystallization stage of the $\text{Al}_{86}\text{Ni}_6\text{Y}_{4.5}\text{Co}_2\text{La}_{1.5}$ MG powder [8], resulted in little increase in the sintered density. In contrast, increasing the applied pressure from 200 MPa to 600 MPa led to a substantial increase in the sintered density at each of the three temperatures tested. Increasing pressure was much more effective than increasing sintering temperature. This implies that sintering pressure plays a key role in the densification of $\text{Al}_{86}\text{Ni}_6\text{Y}_{4.5}\text{Co}_2\text{La}_{1.5}$ MG powder during SPS. In fact, the near full density achieved by increasing pressure is difficult to achieve by increasing sintering temperature alone without nano-crystallization. To find out the underlying reasons for this big difference, the as-sintered microstructure was analyzed in detail using SEM and TEM, with a special focus being placed on the interfaces between powder particles.

X-ray mapping was applied to all the constituent elements (i.e., Al, Ni, Y, Co, and La) as well as O in the samples that

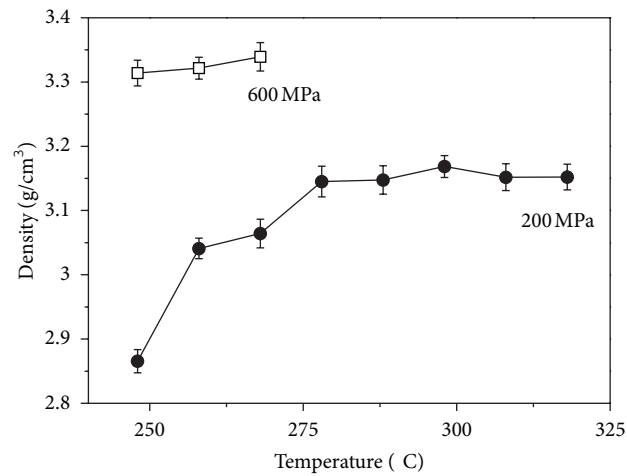
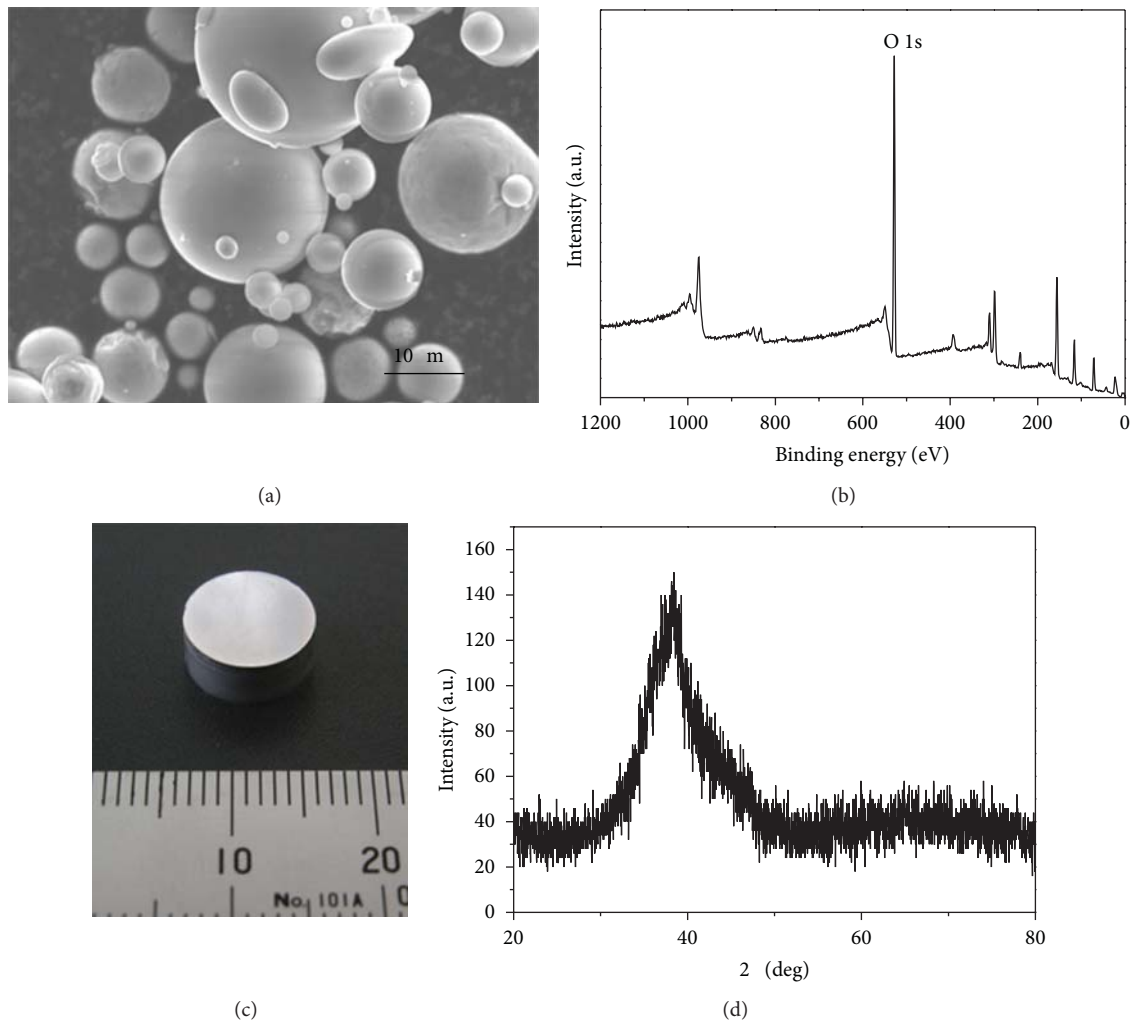


FIGURE 2: Sintered densities of the SPS-processed samples as a function of SPS sintering temperature and pressure.

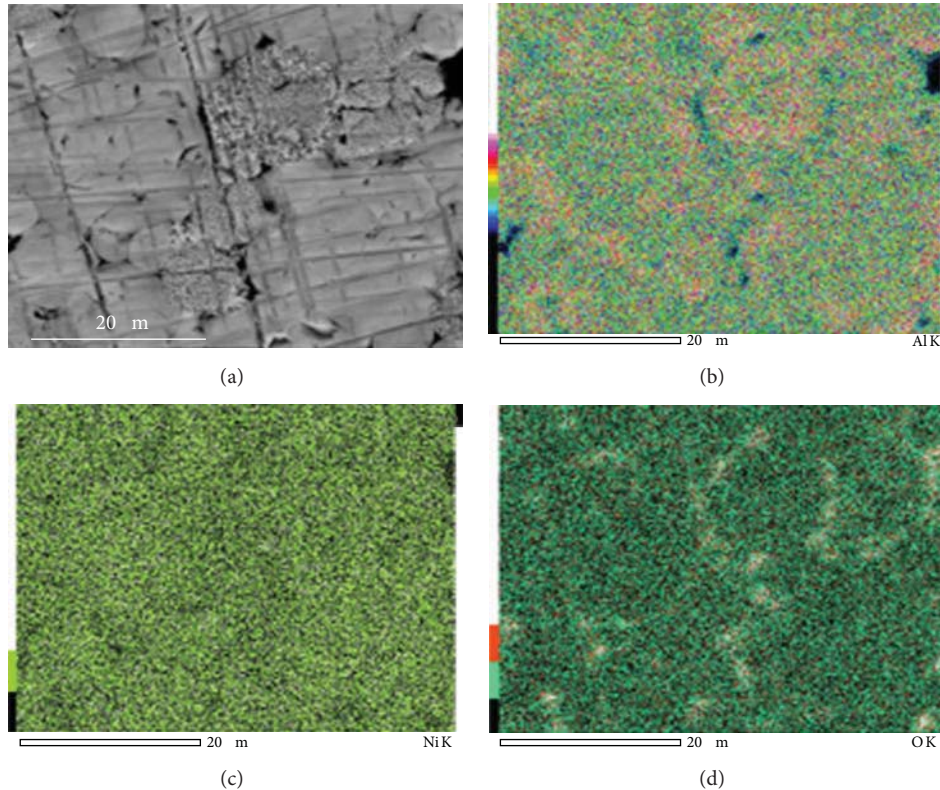


FIGURE 3: SEM mapping results of Al and Ni as well as O in a selected area of an SPS-processed sample sintered at 248.5°C for 2 min under 200 MPa. The distribution of Y, Co, and La is generally homogeneous and similar to that of Ni.

were sintered at 248.5°C under 200 MPa. Figure 3 shows the results of Al, Ni, and O. The distribution of Ni, Y, Co, and La is homogenous in the microstructure, showing few features. However, Al and O are clearly enriched in areas close to the initial particle-particle interfaces (see Figures 3(b) and 3(d)). Furthermore, these Al- and O-enriched areas underwent only limited sintering, where the sintering necks are still recognizable between neighboring particles (see Figure 3(a)), compared to those well-sintered oxygen-deficient areas. It can be deduced that the surface oxide layers have hindered the densification process of the $\text{Al}_{86}\text{Ni}_6\text{Y}_{4.5}\text{Co}_2\text{La}_{1.5}$ MG powder during SPS, and that the 200 MPa of applied pressure can only ensure limited removal of these oxide surface layers. To confirm this inference, TEM was used to investigate the interfaces between the particles in the SPS-processed sample, and the results are shown in Figures 4 and 5.

Figure 4(a) shows that the interface between two particles in the same SPS-processed sample (sintered at 248.5°C under 200 MPa) has undergone noticeable crystallization. The interface layer is about 50 nm thick and oxygen can be detected at the interface using TEM energy dispersive X-ray (EDX) (see Figure 4(c)). This further confirms that the oxide surface layers were not completely removed during SPS under the applied pressure of 200 MPa. In contrast, clean interfaces between particles were uniformly observed in the SPS-processed samples under an applied pressure of 600 MPa. An example is shown in Figure 4(b).

Figure 5(a) shows a detailed view of the aforementioned crystallized interface area (Figure 4(a)) together with the surrounding amorphous matrix. Based on the selected area electron diffraction (SAED) patterns (inset in Figure 5(a)), these crystallized phases are indexed to be fcc-Al. Figure 5(b) shows a high-resolution TEM image of these fcc-Al nanocrystals which are about 10 nm in size. In contrast, no crystallization was detected in samples that were sintered at the same temperature (248.5°C) but under 600 MPa (see Figure 4(b)). The difference can be explained below. Under an applied pressure of 200 MPa and a heating rate of 40°C/min, it is difficult to completely remove the surface oxide layers on powder particles, as evidenced by the results shown in Figures 3 and 4. The remaining oxide surface layers prevent viscous flow between the powder particles and therefore inhibit full densification. Consequently, the sintering necks between the neighboring particles, because of the surrounding pores, will have relatively high electrical resistance. As a result, this will cause high local Joule heat (or enhanced temperature gradient) in these local contact areas [19–21], resulting in severe local nano-crystallization as shown above. With a high applied pressure of 600 MPa, the combined effect of the pressure and the electrical discharge during SPS can effectively disrupt the oxide surface layers on the powder particles leading to a complete removal of the surface oxides. Without the oxide surface layers, viscous flow occurs making full densification possible. This eliminates overheated local areas and therefore prevents local nano-crystallization.

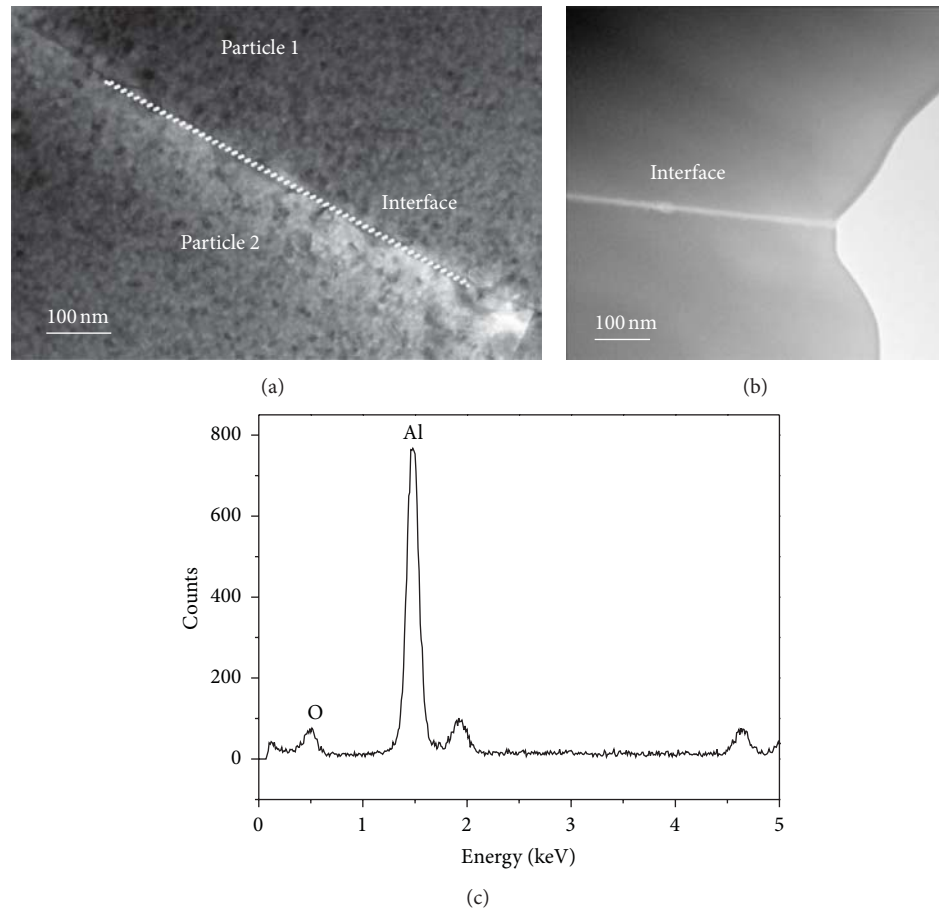


FIGURE 4: TEM bright field (BF) images of particle-particle interfaces in SPS-processed samples: (a) sintered at 248.5°C under 200 MPa; (b) sintered at 248.5°C under 600 MPa, free of crystallization; and (c) TEM-EDX results obtained from the interface shown in (a), indicative of noticeable crystallization of fcc-Al.

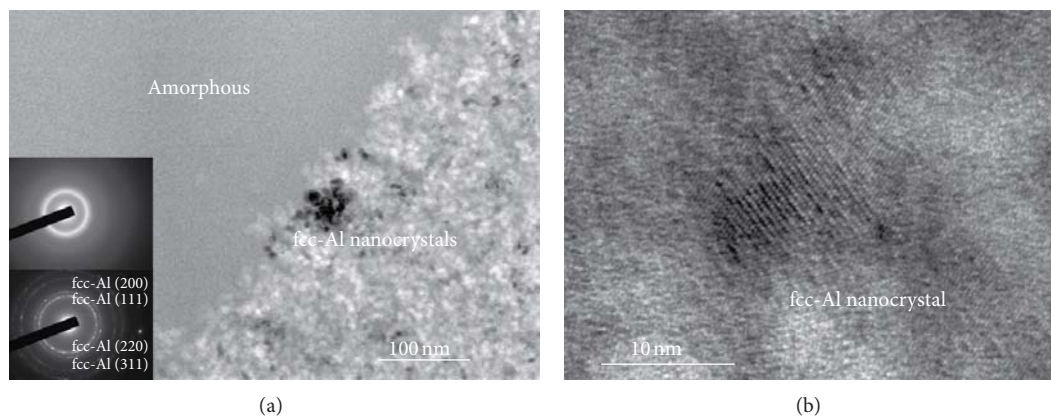


FIGURE 5: TEM BF image of an SPS-processed sample sintered at 248.5°C under 200 MPa. The inset in (a) is the corresponding SEAD patterns for the amorphous matrix and fcc-Al nanocrystals. (b) is an HRTEM image of the fcc-Al nanocrystals shown in (a).

4. Summary

$\text{Al}_{86}\text{Ni}_6\text{Y}_{4.5}\text{Co}_2\text{La}_{1.5}$ BMG disks (diameter: 10 mm; thickness: 4 mm) were fabricated from metallic glass powder of the same composition by SPS. The influence of applied pressure on the densification of $\text{Al}_{86}\text{Ni}_6\text{Y}_{4.5}\text{Co}_2\text{La}_{1.5}$ metallic glass

powder was investigated at different sintering temperatures at a fixed heating rate of 40°C/min. Applying a high pressure (600 MPa) assisted in the removal of the surface oxide layers that enveloped the starting metallic glass powder. This led to full densification of the metallic glass powder flow free of particle-particle interface oxides and nano-crystallization.

The mechanism was attributed to potential viscous flow during SPS between the powder particles. In contrast, both residual oxides and nanocrystalline Al phases were detected at particle-particle interfaces in the $\text{Al}_{86}\text{Ni}_6\text{Y}_{4.5}\text{Co}_2\text{La}_{1.5}$ BMGs fabricated under a low pressure (200 MPa) with respect to the same heating and isothermal sintering parameters. The applied pressure showed a predominant influence on the removal of the surface oxide layers on the starting metallic glass powder during SPS, which is crucial to the consolidation of the metallic glass powder.

Acknowledgments

This work was supported by the Australian Research Council (ARC). The authors would like to thank Professor Jian-qiang Wang of the Institute of Metal Research, Chinese Academy of Sciences, for the provision of the powder. M. Yan acknowledges supports from the Queensland Smart Future Fellowship Programme (Early Career) and a UQ Early Career Researcher Grant. The authors also acknowledge the assistance from the Centre for Microscopy and Microanalysis (CMM) of The University of Queensland and the Australian Microscopy & Microanalysis Research Facility (AMMRF).

References

- [1] W. H. Wang, C. Dong, and C. H. Shek, "Bulk metallic glasses," *Materials Science and Engineering R*, vol. 44, no. 2-3, pp. 45–89, 2004.
- [2] A. Inoue, "Amorphous, nanoquasicrystalline and nanocrystalline alloys in Al-based systems," *Progress in Materials Science*, vol. 43, no. 5, pp. 365–520, 1998.
- [3] B. J. Yang, J. H. Yao, Y. S. Chao, J. Q. Wang, and E. Ma, "Developing aluminum-based bulk metallic glasses," *Philosophical Magazine*, vol. 90, no. 23, pp. 3215–3231, 2010.
- [4] M. Yan, S. Kohara, J. Q. Wang, K. Nogita, G. B. Schaffer, and M. Qian, "The influence of topological structure on bulk glass formation in Al-based metallic glasses," *Scripta Materialia*, vol. 65, no. 9, pp. 755–758, 2011.
- [5] M. Yan, J. Q. Wang, C. Kong, G. B. Schaffer, and M. Qian, "Micrometer-sized quasicrystals in the $\text{Al}_{85}\text{Ni}_5\text{Y}_6\text{Co}_2\text{Fe}_2$ metallic glass: a TEM study and a brief discussion on the formability of quasicrystals in bulk and marginal glass-forming alloys," *Journal of Materials Research*, vol. 27, no. 16, pp. 2131–2139, 2012.
- [6] B. J. Yang, J. H. Yao, J. Zhang, H. W. Yang, J. Q. Wang, and E. Ma, "Al-rich bulk metallic glasses with plasticity and ultrahigh specific strength," *Scripta Materialia*, vol. 61, no. 4, pp. 423–426, 2009.
- [7] A. Inoue, K. Ohtera, A. P. Tsai, and T. Masumoto, "Aluminum-based amorphous-alloys with tensile-strength above 980 Mpa, (100 Kg/Mm²)," *Japanese Journal of Applied Physics Part 2*, vol. 27, no. 4, pp. L479–L482, 1988.
- [8] X. P. Li, M. Yan, B. J. Yang, J. Q. Wang, G. B. Schaffer, and M. Qian, "Crystallization behaviour and thermal stability of two aluminium-based metallic glass powder materials," *Materials Science and Engineering A*, vol. 530, pp. 432–439, 2011.
- [9] C. K. Kim, H. S. Lee, S. Y. Shin, J. C. Lee, D. H. Kim, and S. Lee, "Microstructure and mechanical properties of Cu-based bulk amorphous alloy billets fabricated by spark plasma sintering," *Materials Science and Engineering A*, vol. 406, no. 1-2, pp. 293–299, 2005.
- [10] T. S. Kim, J. Y. Ryu, J. K. Lee, and J. C. Bae, "Synthesis of Cu-base/Ni-base amorphous powder composites," *Materials Science and Engineering A*, vol. 448–451, pp. 804–808, 2007.
- [11] X. Li, A. Makino, H. Kato, A. Inoue, and T. Kubota, " $\text{Fe}_{76}\text{Si}_{9.6}\text{B}_{8.4}\text{P}_6$ glassy powder soft-magnetic cores with low core loss prepared by spark-plasma sintering," *Materials Science and Engineering B*, vol. 176, no. 15, pp. 1247–1250, 2011.
- [12] D. J. Wang, Y. J. Huang, J. Shen, Y. Q. Wu, H. Huang, and J. Zou, "Temperature influence on sintering with concurrent crystallization behavior in Ti-based metallic glassy powders," *Materials Science and Engineering A*, vol. 527, no. 10–11, pp. 2662–2668, 2010.
- [13] P. P. Choi, J. S. Kim, O. T. H. Nguyen, D. H. Kwon, Y. S. Kwon, and J. C. Kim, "Al-La-Ni-Fe bulk metallic glasses produced by mechanical alloying and spark-plasma sintering," *Materials Science and Engineering A*, vol. 448–451, pp. 1119–1122, 2007.
- [14] T. T. Sasaki, K. Hono, J. Vierke, M. Wollgarten, and J. Banhart, "Bulk nanocrystalline $\text{Al}_{85}\text{Ni}_{10}\text{La}_5$ alloy fabricated by spark plasma sintering of atomized amorphous powders," *Materials Science and Engineering A*, vol. 490, no. 1-2, pp. 343–350, 2008.
- [15] X. P. Li, M. Yan, H. Imai et al., "Fabrication of 10 mm diameter fully dense $\text{Al}_{86}\text{Ni}_6\text{Y}_{4.5}\text{Co}_2\text{La}_{1.5}$ bulk metallic glass with high fracture strength," *Materials Science and Engineering A*, vol. 568, pp. 155–159, 2013.
- [16] M. Yan, P. Yu, K. B. Kim, J. K. Lee, G. B. Schaffer, and M. Qian, "The surface structure of gas-atomized metallic glass powders," *Scripta Materialia*, vol. 62, no. 5, pp. 266–269, 2010.
- [17] X. P. Li, M. Yan, J. Q. Wang et al., "Non-isothermal crystallization kinetics and mechanical properties of $\text{Al}_{86}\text{Ni}_6\text{Y}_{4.5}\text{Co}_2\text{La}_{1.5}$ metallic glass powder," *Journal of Alloys and Compounds*, vol. 530, pp. 127–131, 2012.
- [18] Z. A. Munir, U. Anselmi-Tamburini, and M. Ohyanagi, "The effect of electric field and pressure on the synthesis and consolidation of materials: a review of the spark plasma sintering method," *Journal of Materials Science*, vol. 41, no. 3, pp. 763–777, 2006.
- [19] G. Ji, F. Bernard, S. Launois, and T. Grosdidier, "Processing conditions, microstructure and mechanical properties of hetero-nanostructured ODS FeAl alloys produced by spark plasma sintering," *Materials Science and Engineering A*, vol. 559, pp. 566–573, 2013.
- [20] T. Grosdidier, G. Ji, and S. Launois, "Processing dense hetero-nanostructured metallic materials by spark plasma sintering," *Scripta Materialia*, vol. 57, no. 6, pp. 525–528, 2007.
- [21] G. Ji, T. Grosdidier, N. Bozzolo, and S. Launois, "The mechanisms of microstructure formation in a nanostructured oxide dispersion strengthened FeAl alloy obtained by spark plasma sintering," *Intermetallics*, vol. 15, no. 2, pp. 108–118, 2007.

Research Article

Surface Nanocrystallization of 3Cr13 Stainless Steel Induced by High-Current Pulsed Electron Beam Irradiation

Zhiyong Han,¹ Le Ji,² Jie Cai,² Hui Zou,¹ Zhiping Wang,¹ and Qingfeng Guan²

¹ College of Science, Civil Aviation University of China, Tianjin 300300, China

² School of Materials Science and Engineering, Jiangsu University, Zhenjiang 212013, China

Correspondence should be addressed to Qingfeng Guan; guanqf@ujs.edu.cn

Received 7 December 2012; Accepted 1 February 2013

Academic Editor: Kemin Zhang

Copyright © 2013 Zhiyong Han et al. This is an open access article distributed under the Creative Commons Attribution License, which permits unrestricted use, distribution, and reproduction in any medium, provided the original work is properly cited.

The nanocrystalline surface was produced on 3Cr13 martensite stainless steel surface using high-current pulsed electron beam (HCPEB) technique. The structures of the nanocrystallized surface were characterized by X-ray diffraction and electron microscopy. Two nanostructures consisting of fine austenite grains (50–150 nm) and very fine carbides precipitates are formed in melted surface layer after multiple bombardments via dissolution of carbides and crater eruption. It is demonstrated that the dissolution of the carbides and the formation of the supersaturated Fe (C) solid solution play a determining role on the microstructure evolution. Additionally, the formation of fine austenite structure is closely related to the thermal stresses induced by the HCPEB irradiation. The effects of both high carbon content and high value of stresses increase the stability of the austenite, which leads to the complete suppression of martensitic transformation.

1. Introduction

Nanomaterials with considerable fine grain sizes and significantly large volume fraction of grain boundaries have exhibited superior mechanical, physical, and chemical properties compared to conventional coarse-grained materials [1]. Surface nanocrystallization of a coarse-grained material provides a new approach to improve the properties of the materials [2]. In practice, surface nanostructures of metal materials can be obtained via severe plastic deformation using surface mechanical attrition treatment (SMAT) [3], high-energy shot peening (HESP) [4], ultrasonic shot peening [5], wire-brushing [6], and so forth.

Recently, the application of energetic beams such as ion, electron, laser, and plasma has been of increasing interest to modify the surface of the metallic materials [7–11]. Among these techniques, the high-current pulsed electron beam (HCPEB) is relatively new [12, 13]. The energy concentration per pulse is high and could be varied within a relatively large range. Hence, any type of exposure to the heat of the near-surface layers of materials could be achieved: heating, melting, and high-rate evaporation. A subsequent fast cooling is followed by high-rate crystallization of the melt

and generation of the thermoelastic dynamic and quasistatic mechanical stresses in the region under irradiation, which inevitably cause high-rate deformation. The combination of the above-mentioned factors due to the HCPEB treatment can promote structural phase transformations and result in the formation of very fine grains within the irradiated surface layers, which would remarkably influence the physical-mechanical properties of the irradiated surface.

In this work, the surface nanocrystallization of 3Cr13 steel resulted from the HCPEB irradiation is reported. The surface nanocrystallization has potential applications in industries due to its high efficiency, simplicity, and reliability of the HCPEB technique.

2. Experimental

The HCPEB equipment, used in this work, is a Nadezhda-2 type, which can produce an electron beam with low electron energy in the range of 10–40 kV, high peak current with the range of 10^2 – 10^3 A/cm², short pulsed duration of 0.5–1.5 μ s, and cross-section area 30 cm². The electron beam is generated by an explosive emission cathode, and the accelerating

TABLE 1: The compositions of 3Cr13 stainless steel.

Samples	Chemical composition (wt.%)						
	C	Cr	Mn	S	P	Ni	Si
3Cr13	0.28	13.26	0.58	0.015	0.018	0.50	0.82

voltage, magnetic fields strength, and the anode-collector distance can be adjusted to control the beam energy density. More details about the HCPEB system are described in [7].

A typical 3Cr13 martensite stainless steel was used for study in this work. Its chemical composition was listed in Table 1. Before the electron beam treatment, the samples were machined to dimensions of 14 mm × 10 mm × 5 mm and austenitized at 1050°C for 30 min. Oil quenching terminated this heat treatment. The steel was subsequently tempered at 620°C for 2 h. The sample surface was prepared before the HCPEB treatment by mechanical polishing to ensure a similar initial surface state. The energy of the electron beam was kept constant at 24.3 keV, and different pulse numbers were used (5 and 10 times). For all treatments, the pulsing time was about 1.5 μ s, and 10 s were set between each pulse.

Surface and cross-section microstructures were characterized using a field emission gun scanning electron microscope (SEM, JEOL JSM-7001F). X-ray diffraction (XRD) was carried out with the CuK_α in a Rigaku D/Max-2500/pc X-ray diffractometer. Microstructures were further examined with a transmission electron microscope (TEM) of type JEM-2100. The foils used for TEM observations were obtained by preparing one-sided mechanically prethinned, dimpled, and, in the last step, electrolytic thinning of the thin plates until the electron transparency occurred.

3. Results

The XRD patterns of the samples before and after the HCPEB irradiations are shown in Figure 1. The evident broadening of the Bragg reflection profiles may be attributed to fine grain size and high value of residual stress. Figure 1 also reveals that the peaks of the martensite phase are shifted to lower angles, signifying the increase of the lattice parameter. It might come from the presence of tensile residual stresses in the surface [12]. Additionally, the peaks of carbide (Cr_7C_3) vanish completely, and the peaks of γ austenite emerge after the irradiations with 5 and 10 pulses. It is indicated that the dissolved Cr_7C_3 carbide increased the content of carbon in the martensite, which could also result in the increase of the lattice parameter. Note that the peak intensity of the γ -Fe phase increases with the number of pulses, indicating that the volume fraction and/or grain sizes of the γ -phase increases with increasing the number of pulses.

The almost complete dissolving of the carbides is in good agreement with the SEM morphology observations shown in Figure 2. Figure 2(a) reveals the morphology of the treated surface where many craters are present. According to previous studies, such a typical morphology is the result of the local sublayer melting and eruption through the solid outer surface [10, 14]. Figures 2(b) and 2(c) show the typical cross-sectional micrograph of the etched samples after 5 and

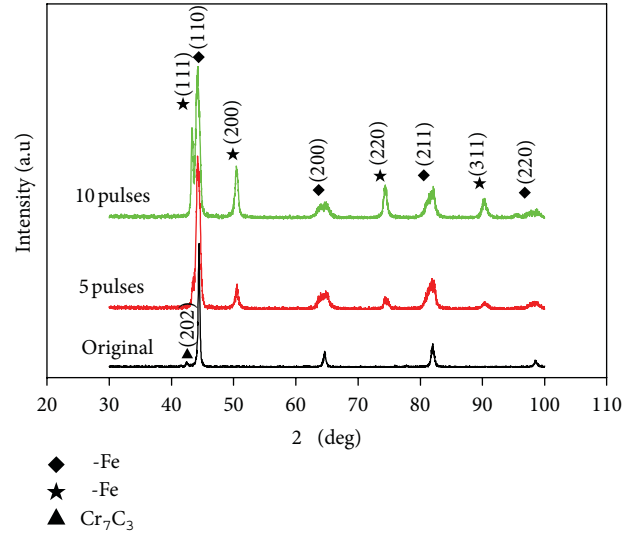


FIGURE 1: XRD patterns of the untreated and treated samples.

10 pulses of the HCPEB irradiation, respectively. The top surface layer, corresponding to the melted layer that is known to be weakly etchable [9, 15] as shown in Figures 2(b) and 2(c), appears with a gray contrast, which completely differs from the other part of samples. The depth of the melted layer measured from Figures 2(b) and 2(c) is about 4–6 μ m.

Figure 3(a) exhibits the SEM images of the irradiated surface where the craters are seldom presented. One can see that two typical characteristics of features were formed on the irradiated surface, namely island feature (indicated by letter A) and martensite-like feature (indicated by letter B). High magnification SEM images of both regions, as shown in Figures 3(b) and 3(c), reveal that very fine grains with sizes of 80 nm are approximately homogeneously dispersed on the irradiated surface, clearly indicating that the melted surface layer is mainly composed of refined grains or subgrains.

TEM micrograph shown in Figure 4(a) shows the typical microstructure of the untreated sample, consisting of Cr_7C_3 carbides and martensite. After 5 pulses, as shown in Figure 4(b), the original carbides phase disappears, and the grains with sizes from 50 to 150 nm are formed. After 10 pulses, similar microstructure was observed in Figure 4(c) compared to its 5 pulses counterpart. The primary differences lie in that a little larger grain sizes (about 80–200 nm) were obtained for 10 pulses sample. It is worth noting that the interiors of the fine grain appear to be clean without any detectable defects. The corresponding selected area electron diffraction (SAED) pattern (Figure 4(d)) shows a random crystallographic orientation, indicating the formation of equiaxed fine γ austenite grain structure in the melted layer. A careful look at the micrograph in Figures 4(b) and 4(c) also reveals very fine precipitates with sizes below 20 nm. They are often present at the grain boundaries (Figure 4(b)) and triple junctions (Figure 4(c)). Their presence at grain boundary and/or triple junctions suggests that they precipitated from the solid state in nature.

The formation of fine precipitates can be attributed to the rapid quenching process from the supersaturated Fe (C) solid

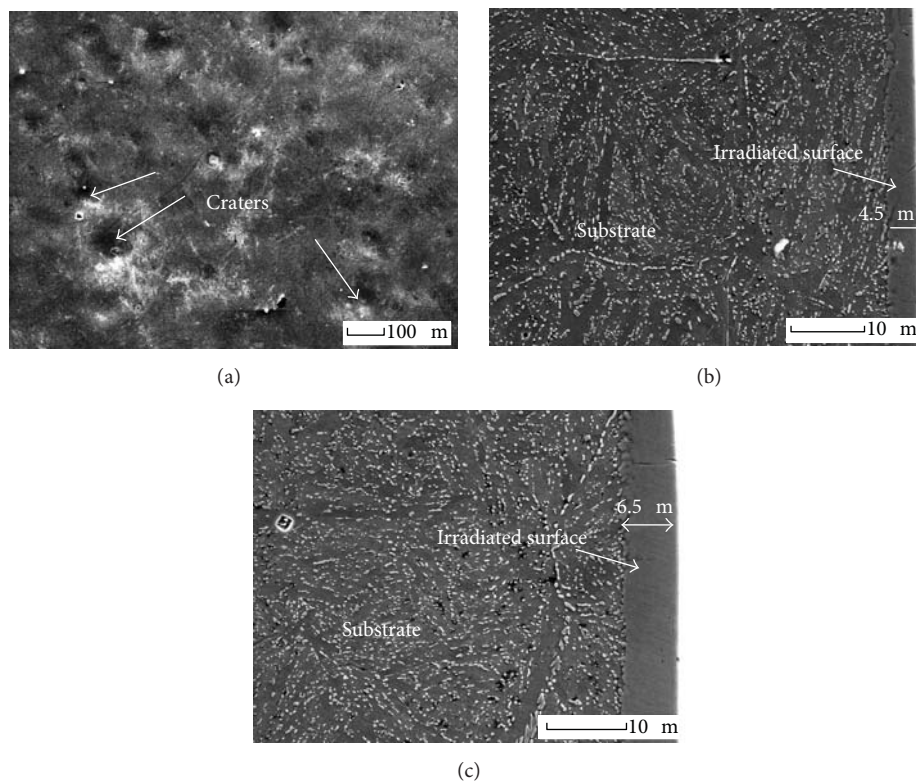


FIGURE 2: SEM micrographs showing the surface morphology (a), cross-sectional aspect of the samples irradiated for 5 pulses (b), and 10 pulses (c).

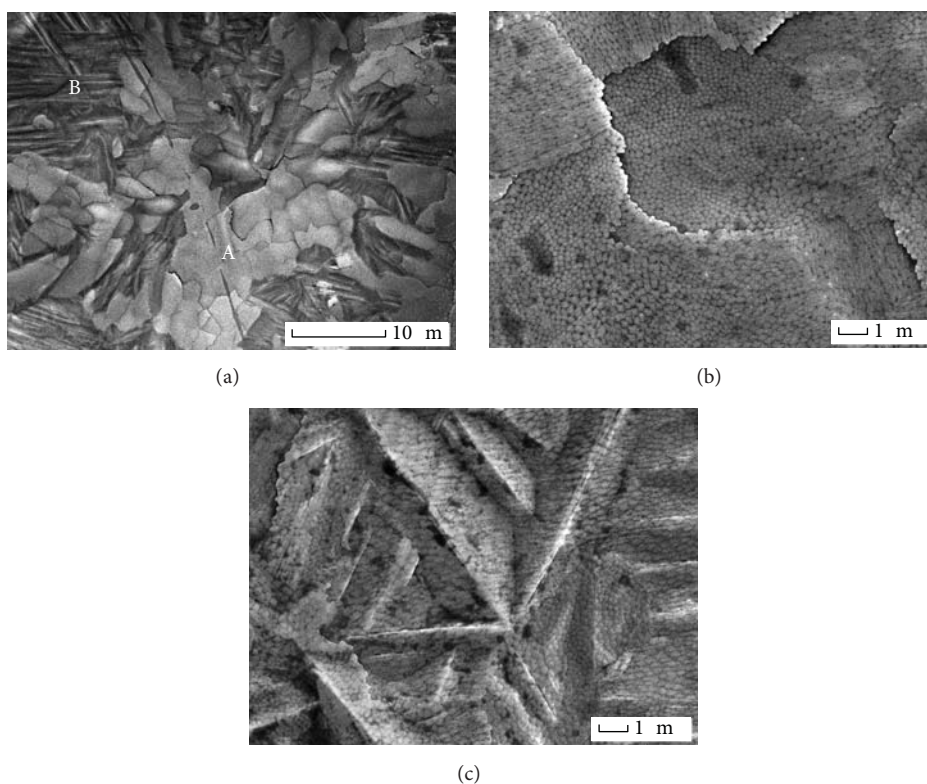


FIGURE 3: Typical SEM images of island region (marked A) and martensite-like region (marked B) (a), high-magnification SEM images of the region A (b), and the region B (c), showing the surface aspects.

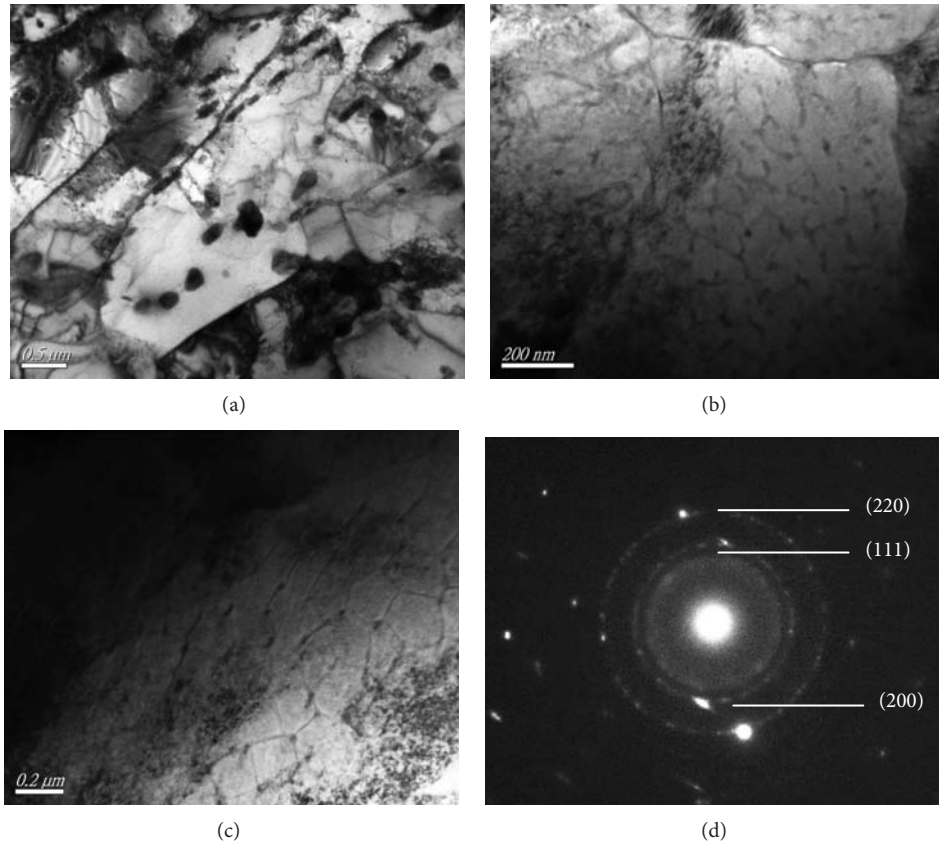


FIGURE 4: TEM images showing the aspects of the melted surface layer of the 3Cr13 steel, (a) untreated, (b) treated with 5 pulses, (c) treated with 10 pulses, and (d) the corresponding electron diffraction pattern of (c).

solution after the dissolution of the carbides. The transient cooling process inhibits the precipitation and growth of carbides and finally leads to the formation of very fine carbide precipitates.

The surface structure is more pronouncedly characterized by the nanostructure austenite. Stahl et al. observed the formation of a thin layer (about $0.3\ \mu\text{m}$) of a nanoaustenite structure after irradiating a prequenched bearing steel using a pulsed laser [16]. Similar results were also observed in D2 steel [9, 15] HSS S6-5-2 steel [17], and M50 steel [18] irradiated by the multiple pulses of the HCPEB irradiation. Our observation is a little different from the studies of Zou et al. [9, 15, 18]. In their studies, similar austenite grains were observed after the HCPEB remelting of the D2 steel, and so forth. However, they concluded that the austenite has a high orientation tendency. Comparatively, in our study, a random crystallographic orientation and equiaxed fine austenite grain structure were obtained.

An interesting phenomenon found in the present work is the stabilization of the austenite in the melted layer of the irradiated samples despite the very high cooling rate undergone by the surface of the sample. In the present case, the austenite directly grows from the melt during the rapid solidification process, and the high amounts of Cr and C in this phase due to the dissolution of the initial carbide particles are an important factor for suppressing the martensitic transformation [9]. In addition, the very

fine size of the austenite grains is another factor for the stabilization of the austenite phase because it will significantly enhance its strength and make the accommodation of a martensitic variant more difficult [15]. Finally, in our opinion, the thermal stress induced by the surface irradiation may be an important factor which should affect the formation of fine austenite. Based on Bardenshtein et al.'s research [19], austenite is favored by the thermal stresses. When an electron beam irradiates the target, due to the drastic temperature change, a steep temperature gradient is generated along the incident direction of the beam. However, due to the lateral confinement along the surface, the thermal expansion in the directions vertical to the beam is strongly resisted, causing the surface thermal stress. This external force increased the internal stress to an extraordinarily high level [20]. The microstructure of the sublayer beneath the melted layer was also investigated, and the results are shown in Figure 5. It illuminates the substructure in some of the preformed martensite plates, indicating the formation of deformation twins within martensite plates. In Figure 5(b), very high density of dislocations was produced in the interior of preformed martensite plates. Apparently, high density of dislocations was introduced by the intense deformation under the action of high value of applied stresses. It is reasonably believed that the formation of the twins in the preformed martensite plates was mainly resulted from the high applied stresses and the strain rate due to the rapid heating and

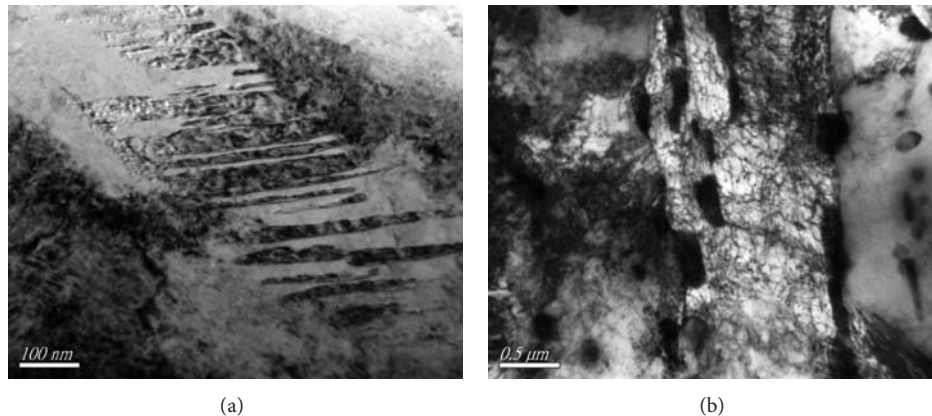


FIGURE 5: TEM images of deformation twins (a) and dislocation configurations (b), showing the deformation microstructures in the preformed martensite beneath melted surface layer.

cooling caused by HCPEB irradiation [20]. Therefore, the formation of fine austenite structure in this work is closely related to the thermal stresses induced by HCPEB irradiation.

It is well known that surface nanostructures exhibit superior mechanical properties compared to conventional coarse-grained materials. Moreover, high value of residual stresses accumulated in the subsurface layer below the top nanostructure surface are favored to the improvement of the surface performance. In conclusion, HCPEB irradiations provide an effective method for fabricating surface nanostructure.

4. Conclusions

The initial samples of 3Cr13 steel were irradiated by high-current pulsed electron beam. The surface structures were investigated in detail using X-ray diffraction, SEM, and TEM. According to experimental results, we conclude as follows.

After HCPEB posttreatments, irradiated surface melted, and a supersaturated Fe (C) solid solution phase was formed after multiple bombardments. Rapid solidification caused the formation of two nanostructures consisting of fine austenite grains (50–150 nm) and very fine carbides precipitates in the melted surface layer via dissolution of carbides and crater eruption. Rapid heating and cooling induced heavy plastic deformation beneath the melted layer, which lead to the formation of deformation twins and high density of dislocations within martensite plates. The dissolution of the carbides and the formation of the supersaturated Fe (C) solid solution play a determining role on the microstructure evolution. Furthermore, the formation of the fine austenite structure is closely related to the thermal stresses induced by the HCPEB irradiation. The effects of both high carbon content and high value of stresses increase the stability of the austenite, which leads to the complete suppressing of martensitic transformation.

Acknowledgments

This work was supported by the National Natural Science Foundation of China (U1233111 and 50671042), to which the authors are very grateful.

References

- [1] R. W. Cahn, "Nanostructured materials," *Nature*, vol. 348, no. 6300, pp. 389–390, 1990.
- [2] Z. B. Wang, N. R. Tao, W. P. Tong, J. Lu, and K. Lu, "Diffusion of chromium in nanocrystalline iron produced by means of surface mechanical attrition treatment," *Acta Materialia*, vol. 51, no. 14, pp. 4319–4329, 2003.
- [3] Z. B. Wang, N. R. Tao, S. Li et al., "Effect of surface nanocrystallization on friction and wear properties in low carbon steel," *Materials Science and Engineering A*, vol. 352, no. 1-2, pp. 144–149, 2003.
- [4] C. H. Chen, R. M. Ren, X. J. Zhao, and Y. J. Zhang, "Surface nanostructures in commercial pure Ti induced by high energy shot peening," *Transactions of Nonferrous Metals Society of China*, vol. 14, no. 2, pp. 215–218, 2004.
- [5] X. Wu, N. Tao, Y. Hong, B. Xu, J. Lu, and K. Lu, "Microstructure and evolution of mechanically-induced ultrafine grain in surface layer of AL-alloy subjected to USSP," *Acta Materialia*, vol. 50, no. 8, pp. 2075–2084, 2002.
- [6] M. Sato, N. Tsuji, Y. Minamino, and Y. Koizumi, "Formation of nanocrystalline surface layers in various metallic materials by near surface severe plastic deformation," *Science and Technology of Advanced Materials*, vol. 5, no. 1-2, pp. 145–152, 2004.
- [7] A. D. Pogrebnjak, V. S. Ladysev, N. A. Pogrebnjak et al., "Comparison of radiation damage and mechanical and tribological properties of α -Fe exposed to intense pulsed electron and ion beams," *Vacuum*, vol. 58, no. 1, pp. 45–52, 2000.
- [8] L. E. Xiaoyun, Y. Sha, Z. Weijiang, H. Baoxi, W. Yugang, and X. Jianming, "Computer simulation of thermal-mechanical effects of high intensity pulsed ion beams on a metal surface," *Surface and Coatings Technology*, vol. 128-129, no. 1, pp. 381–386, 2000.
- [9] J. X. Zou, T. Grosdidier, K. M. Zhang, and C. Dong, "Mechanisms of nanostructure and metastable phase formations in the surface melted layers of a HCPEB-treated D2 steel," *Acta Materialia*, vol. 54, no. 20, pp. 5409–5419, 2006.
- [10] K. M. Zhang, J. X. Zou, T. Grosdidier, and C. Dong, "Crater-formation-induced metastable structure in an AISI D2 steel treated with a pulsed electron beam," *Vacuum*, vol. 86, no. 9, pp. 1273–1277, 2012.
- [11] J. X. Zou, K. M. Zhang, S. Z. Hao, C. Dong, and T. Grosdidier, "Mechanisms of hardening, wear and corrosion improvement of 316 L stainless steel by low energy high current pulsed

- electron beam surface treatment," *Thin Solid Films*, vol. 519, no. 4, pp. 1404–1415, 2010.
- [12] K. M. Zhang, J. X. Zou, B. Bolle, and T. Grosdidier, "Evolution of residual stress states in surface layers of an AISI D2 steel treated by low energy high current pulsed electron beam," *Vacuum*, vol. 87, pp. 60–68, 2013.
- [13] K. M. Zhang, J. X. Zou, T. Grosdidier, and C. Dong, "Microstructure and property modifications of an AISI H13 (4Cr5MoSiV) steel induced by pulsed electron beam treatment," *Journal of Vacuum Science and Technology A*, vol. 28, no. 6, pp. 1349–1355, 2010.
- [14] Y. Qin, X. G. Wang, C. Dong et al., "Temperature field and formation of crater on the surface induced by high current pulsed electron beam bombardment," *Acta Physica Sinica*, vol. 52, no. 12, pp. 3043–3048, 2003.
- [15] J. X. Zou, T. Grosdidier, K. M. Zhang, B. Gao, S. Z. Hao, and C. Dong, "Microstructures and phase formations in the surface layer of an AISI D2 steel treated with pulsed electron beam," *Journal of Alloys and Compounds*, vol. 434–435, pp. 707–709, 2007.
- [16] G. Stähli and C. Sturzenegger, "On the formation of austenitic boundary layers by short laser-pulse reaction with steel," *Scripta Metallurgica*, vol. 12, no. 7, pp. 617–622, 1978.
- [17] V. P. Rotshtein, D. I. Proskurovsky, G. E. Ozur, Y. U. F. Ivanov, and A. B. Markov, "Surface modification and alloying of metallic materials with low-energy high-current electron beams," *Surface and Coatings Technology*, vol. 180–181, pp. 377–381, 2004.
- [18] G. Z. Tang, F. J. Xu, G. H. Fan, X. X. Ma, and L. Q. Wang, "Mechanisms of microstructure formations in M50 steel melted layer by high current pulsed electron beam," *Nuclear Instruments and Methods in Physics Research B*, vol. 288, pp. 1–5, 2012.
- [19] A. Bardenshtein, L. Bushnev, E. Dudarev, A. Markov, and V. Rotshtein, "Thermal stresses and twinning in thin copper samples irradiated with a high-current electron beam," in *Proceedings of the 1st International Congress on Radiation Physics, High Current Electronics and Modification of Materials*, vol. 3, pp. 43–52, Tomsk, Russia, 2000.
- [20] Q. F. Guan, Q. Y. Zhang, C. Dong, and G. T. Zou, "Deformation twinning in single-crystal aluminum induced by high-current pulsed electron beam," *Journal of Materials Science*, vol. 40, no. 18, pp. 5049–5052, 2005.

Review Article

Nanostructure Formations and Improvement in Corrosion Resistance of Steels by Means of Pulsed Electron Beam Surface Treatment

K. M. Zhang,¹ J. X. Zou,^{2,3,4} and T. Grosdidier^{3,4,5}

¹ School of Materials Engineering, Shanghai University of Engineering Science, Shanghai 201620, China

² Shanghai Engineering Research Center of Mg Materials and Applications, National Engineering Research Center of Light Alloy Net Forming, Shanghai Jiao Tong University, Shanghai 200240, China

³ State Key Laboratory of Metal Matrix Composite, School of Materials Science and Engineering, Shanghai Jiao Tong University, Shanghai 200240, China

⁴ Laboratoire d'Etude des Microstructures et de Mécanique des Matériaux (LEM3), Université de Lorraine, Ile du Saulcy, UMR 7239, 57045 Metz, France

⁵ Laboratory of Excellence on Design of Alloy Metals for Low-Mass Structures (DAMAS), University of Lorraine, 57045 Metz, France

Correspondence should be addressed to K. M. Zhang; zhangkm@sues.edu.cn

Received 12 December 2012; Accepted 25 January 2013

Academic Editor: Gang Ji

Copyright © 2013 K. M. Zhang et al. This is an open access article distributed under the Creative Commons Attribution License, which permits unrestricted use, distribution, and reproduction in any medium, provided the original work is properly cited.

The corrosion of steels has long been the topic for materials scientists. It is established that surface treatment is an efficient way to improve the corrosion resistance of steels without changing the bulk properties and with low costs. In the present paper, different kinds of surface treatment techniques for steels are briefly reviewed. In particular, the surface modification involving nanostructure formations of steels by using a low energy high pulsed electron beam (LEHCPEB) treatment is lightened in the case of an AISI 316L stainless steel and D2 steel. The overall results demonstrate the high potential of the LEHCPEB technique for improving the corrosion performance of steels.

1. Introduction

Steels are the most widely used metallic materials both in industrials and in our daily life. This is due to their superior properties, such as high strength, good ductility, high hardness, and low costs. However, steels often suffer from staining, rusting, and corroding in different environments [1–3], which may cause serious problems or even failure of the components made of steels. Usually, general corrosion occurs in carbon steels or low-alloyed steels since there is no dense protective films formed on these steels [4]. Therefore, the steels are continuously corroded. The so-called stainless steel usually contains Cr of more than 11 wt% [5]. As a result of the high Cr content, a dense protective Cr oxide layer can be formed on the surface in corrosive environments, which will prevent the further corrosion of the bulk material. Nevertheless, stainless steel can be affected by pitting in the presence of halide

ions, particularly the chloride ion [6–8]. Therefore, corrosion resistance is of first concern for different kinds of steels to be used in industrial. The addition of alloying elements, such as Cr, into steels is a way to improve the corrosion resistance of steels. However, alloying of the bulk material will also change the mechanical properties of the steels. Furthermore, alloying is also very costly.

To compromise the corrosion, mechanical properties, and the cost, the ideal solution would be to use surface modification techniques to generate a protective layer at the near-surface region or on the surface of the steels. In the past decades, different surface modification techniques have been applied to improve the corrosion resistance of steels. It is found that carburizing, boriding, and nitriding can be used to create a hardened layer on the steel surface, containing mainly carbides, borides, or nitrides, respectively. These hardened layers may also have better corrosion resistance

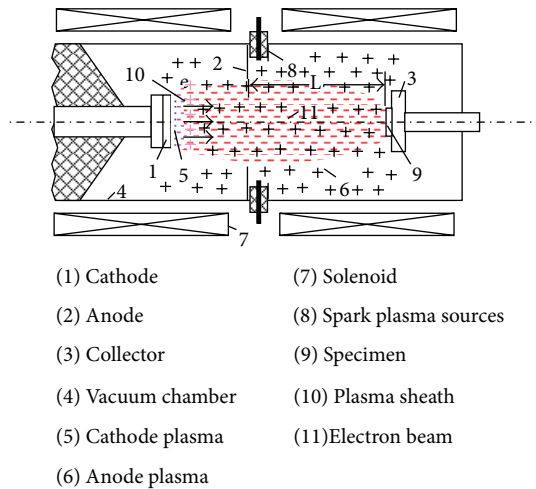


FIGURE 1: Schematic diagram of the LEHCPEB source based on vacuum spark plasma.

than their substrates [9–12]. By using laser surface remelting and cladding, the corrosion resistance of laser-treated steels can be also greatly improved. This was mainly attributed to a homogenization of the elements in the remelted surface layer or the addition of protective alloying elements/compounds [13, 14]. Other methods, mainly film deposition techniques such as physical vapour deposition (PVD), chemical vapour deposition (CVD), sol-gel methods, electroless plating, and so on [15–17], have also been introduced to modify the steel surfaces. For instances, TiN, CrN, NbN, and TiCN films or multilayer films can be deposited onto steel surfaces by using various film deposition techniques [18–21]. Although these films always have better corrosion resistance, the surface properties strongly depend on the quality of the films such as pinholes and impurities, which are not easy to control. Furthermore, the films often suffer from poor adhesion with the substrates. Ion implantation is also testified to be able to improve the corrosion resistance of steels through introducing alloying elements into the very top surface layers [22–24]. However, the ion-implanted layers, usually less than $1\text{ }\mu\text{m}$ in thickness, are too thin to sustain long-time corrosion.

Low Energy High Current Pulsed Electron Beam (LEHCPEB) technique is a recently developed technique for surface modification of metallic materials [25, 26]. The pulsed electron irradiation induces (i) very rapid heating, melting, solidification, and cooling of the surface together with (ii) the formation of thermal stress waves. As a result, improved surface properties of the material, often unattainable with conventional surface treatment techniques, can be obtained fairly easily. This is particularly true for tribological properties [27–29]. Previous investigations have suggested that the LEHCPEB technique could be also used to improve the corrosion resistance of precipitates containing alloys [30–32]. The pulsed electron irradiation generated by this surface treatment technique induces rapid melting of the surface followed by extremely fast solidification. This process leads to the dissolution of second-phase particles and, after sufficient number of pulses, to the formation of a

$2\text{--}3\text{ }\mu\text{m}$ thick homogeneous melted surface [33]. In the case of the steels, the subsequent ultra-fast solidification leads to a structure containing nanostructured domains [34]. It will be shown in the following sections that those effects induced by the LEHCPEB treatments can significantly improve the corrosion resistance of steels.

2. The LEHCPEB System

The pulsed electron beam treatment was carried out with a Nadezhda-2 type LEHCPEB source [25, 35]. It produces an electron beam of low energy ($10\text{--}40\text{ keV}$), high-peak current ($10^2\text{--}10^3\text{ A/cm}^2$), short pulse duration (approx. $1\text{ }\mu\text{s}$), and high efficiency (repeating pulse interval being 10 s). Figure 1 shows a detailed sketch of the electron beam gun, a major part of the electron beam system which produces electron beams. The explosive emission cathode is made of porous graphite for its low ionization potential. The anode is made of stainless steel and has a hole in its center through which the beam passes. Graphite cathode spark plasma sources are placed evenly in a circle behind the anode. The electron beam is transported through the anode plasma to the collector. To prevent the beam from pinching and dispersing, an external magnetic field created by a sectioned solenoid is used. The accelerating voltage, magnetic field intensity, and anode-collector distance control the beam energy density. More details about the LEHCPEB system can be found in [35, 36].

3. Surface Modifications of Steels by the LEHCPEB Treatment

Two examples of steels treated by the LEHCPEB are shown here, namely, AISI 316L stainless steel and AISI D2 steel. The details about the starting materials and their LEHCPEB treatments can be found in [32–34]. In both cases, the modifications in microstructure and corrosion resistance induced by the treatment will be reviewed and discussed in detail.

3.1. Improving Corrosion Resistance of 316L Stainless Steel by LEHCPEB. Figure 2(a) shows a SEM image of the microstructure of the AISI 316L stainless steel in the as-received condition after etching in chloronitrous acid and observation under secondary electron imaging (SEI) condition. The microstructure is primarily a single austenitic phase structure. Many of the grains are twinned, and their size is about $40\text{--}60\text{ }\mu\text{m}$. Figure 2(b) is a backscattered electron image (BEI) of the untreated sample. The composition is fairly homogenous on the whole surface, but many tiny inclusions are visible. These inclusions are the intentionally introduced MnS particles [37] improving machinability. Electron probe microanalysis was also carried out on the treated samples to reveal the possible composition changes in the LEHCPEB-treated samples. Figure 3 shows the results from the samples treated for 5 and 20 pulses with a beam energy of 3 J/cm^2 . Figure 3(a) is a secondary electron image of the sample treated for 5 pulses, and Figure 3(b) is the corresponding backscattered electron image. In Figure 3(a), a large amount

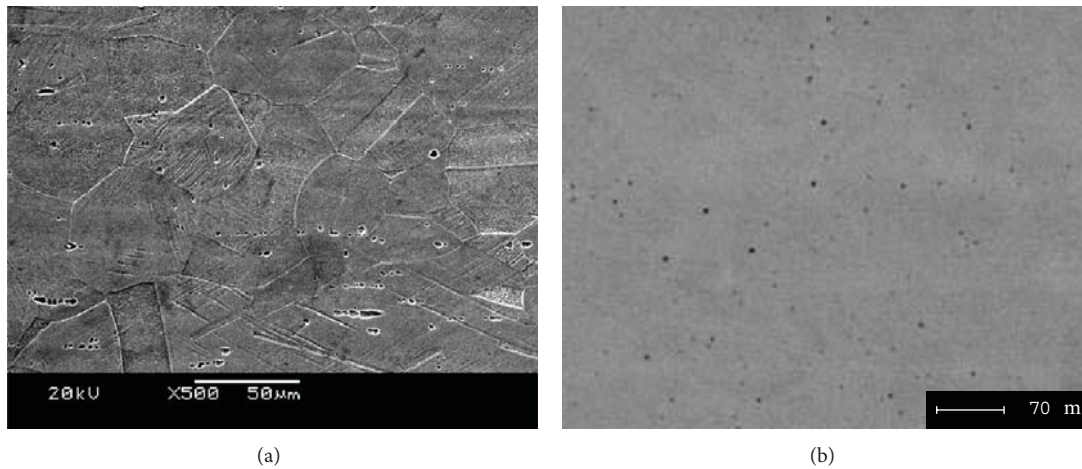


FIGURE 2: SEM images obtained under SEI (a) and BEI (b) imaging conditions for the initial sample.

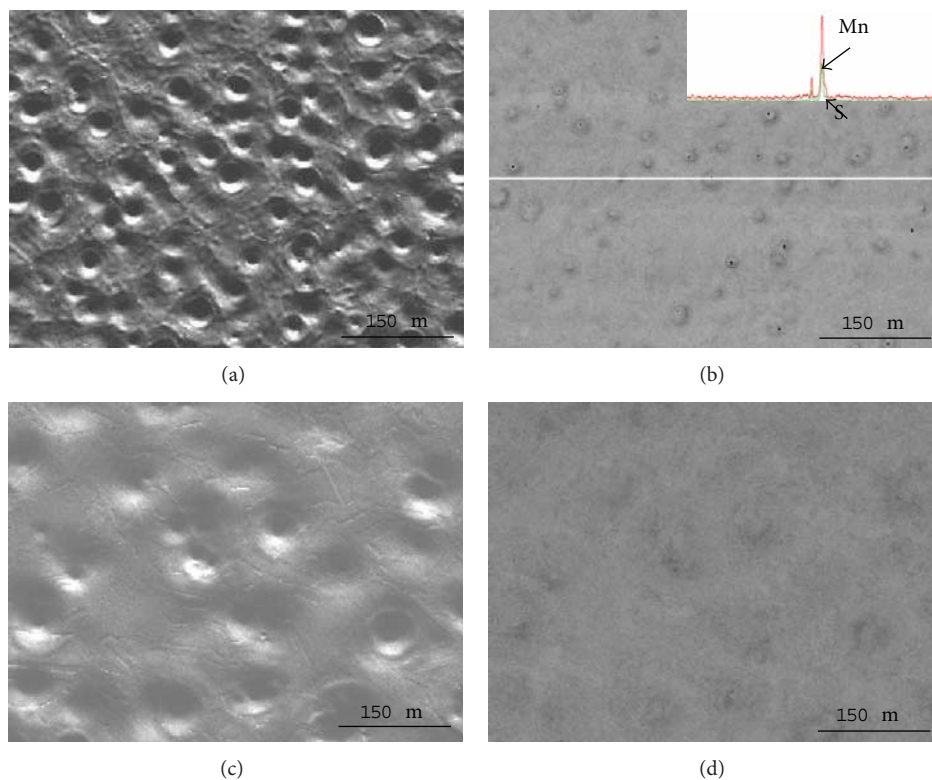


FIGURE 3: Images of the samples treated for 5 ((a) and (b)) and 20 ((c) and (d)) pulses observed under SEI ((a) and (c)) and BEI ((b) and (d)) conditions.

of craters can be observed, which are commonly present on metal surfaces treated with pulsed energetic beams [38, 39]. They are distributed fairly homogeneously on the whole surface. In Figure 3(b), some dark spots still exist on the surface, but their quantity is reduced compared to the initial state. Comparing Figures 3(a) and 3(b), it is clear that the dark spots are always located at the center of the craters. The elemental line scan shown in Figure 3(b) reveals that the dark spots correspond to S- and Mn-rich particles or MnS inclusions. The previously mentioned result indicates

that the MnS particles initiate the craters. Figures 3(c) and 3(d) display the same analysis for the 20-pulse sample. In Figure 3(c), only a few craters are present after 20 pulses. The crater density is much lower than the one reported for the 5-pulse treatment. Figure 3(d) shows that the dark spots have almost completely disappeared. In brief, the second phase particles are the nucleation sites for craters during the LEHCPEB treatment.

A typical example of SNMS analysis in 20-pulse sample is given in Figure 4 where the evolutions in the Fe, Cr, Ni,

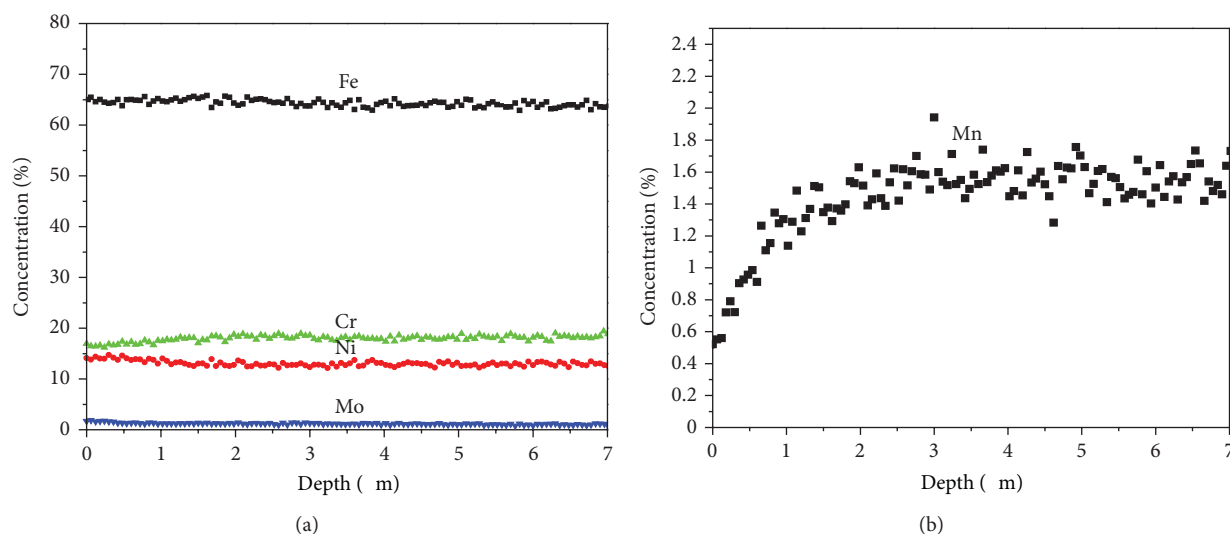


FIGURE 4: A typical example of surface composition profiles of the 316L stainless steel sample treated by LEHCPEB for 20 pulses measured by SNMS.

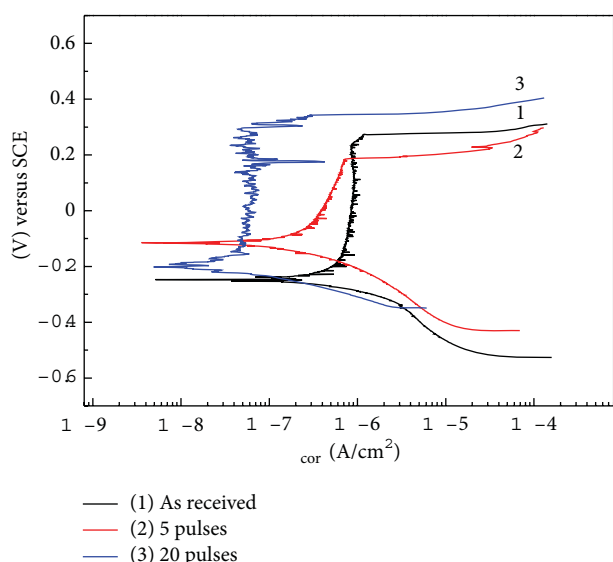


FIGURE 5: Potentiodynamic polarization curves of the treated and untreated AISI 316L stainless steel in the TSB fluid.

Mo, and Mn concentrations are plotted as a function of the distance from the surface. After 20 pulses, as illustrated in Figure 4(a), the Fe, Ni, Cr, and Mo concentrations remained nearly constant. On the other hand, the Mn concentration decreases significantly toward the surface from 1.6 at. % in the bulk of the steel down to about 0.6 at. % at the top surface, as shown in Figure 4(b). Considering that a part of Mn exists in MnS particles, the decrease in Mn concentration in the surface layer confirmed the occurrence of the selective purification effect during the LEHCPEB treatment.

Figure 5 shows the results of the potentiodynamic polarization curves of the untreated and treated samples. All the samples have a passive behavior in the Tyrode's simulated body fluid (TSBF) solution. The corrosion current density

of the LEHCPEB-treated samples decreased when increasing the pulse numbers. The corrosion current density of the sample after 20 pulses was an order of magnitude lower than that of the untreated sample. The corrosion potential (E_{corr}) of all the treated samples is also increased to some extent. The breakdown potential of the passive film, E_{brk} , increases from 233 mV (SCE) for the untreated sample to 342 mV for the 20-pulsed sample. These polarization curves reveal a significant improvement in the corrosion resistance of the 316L stainless steel after the LEHCPEB treatment. However, the results also show that the 5-pulse sample has a lower broken potential with a narrower passive region compared to that of the untreated sample.

Figure 6 shows the Bode plots of EIS spectra for all the 316L stainless steel samples in the TSB fluid. In the high-frequency region, the impedance reflects the electrolyte resistance between the sample and the reference electrode. At the low-frequency limit, the impedance is attributed to the polarization resistance of the sample in the electrolyte [40]. It is clear that the impedance modulus and the phase angle of the initial sample are always lower than those of the treated samples. From Figure 6(a), it can be seen that $|Z|$ has a nearly linear relation with $\log(f)$. Figure 6(b) indicates that the phase angle ϕ has values close to -80° at low-frequency values ($f < 1$ Hz) after the LEHCPEB treatments. These characteristics indicate that the oxide layer formed on modified samples has predominantly a capacitive behavior [41]. The near capacitive behavior is observed over a wider frequency range for the modified samples. This means that the passive film on the LEHCPEB-modified sample surface can maintain its characteristic response over a longer time. Moreover, the 20-pulse sample displayed higher polarization resistance compared with that of 5-pulse one. This can be observed in both the higher near capacitive values of the phase shift response at low frequencies and in the impedance values at low frequency. From all of the previously mentioned results, we can safely conclude that the corrosion resistance

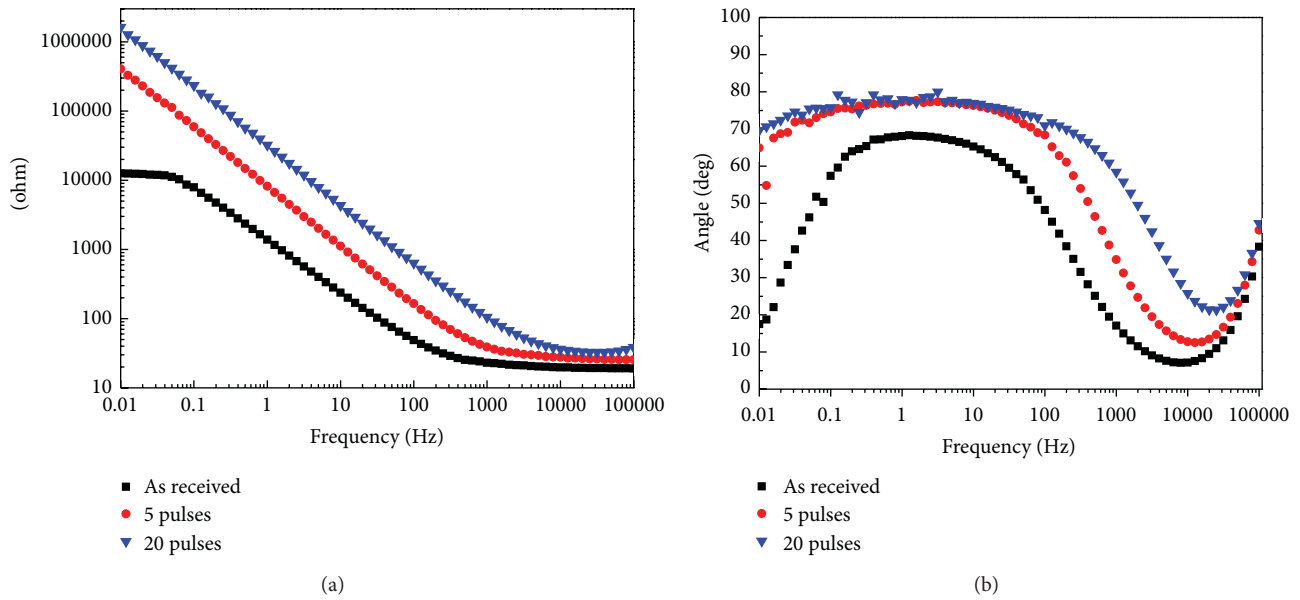


FIGURE 6: Bode plots of 316L samples in the TSB fluid: (a) impedance modulus $|Z|$ versus frequency f , (b) phase angle ϕ versus frequency.

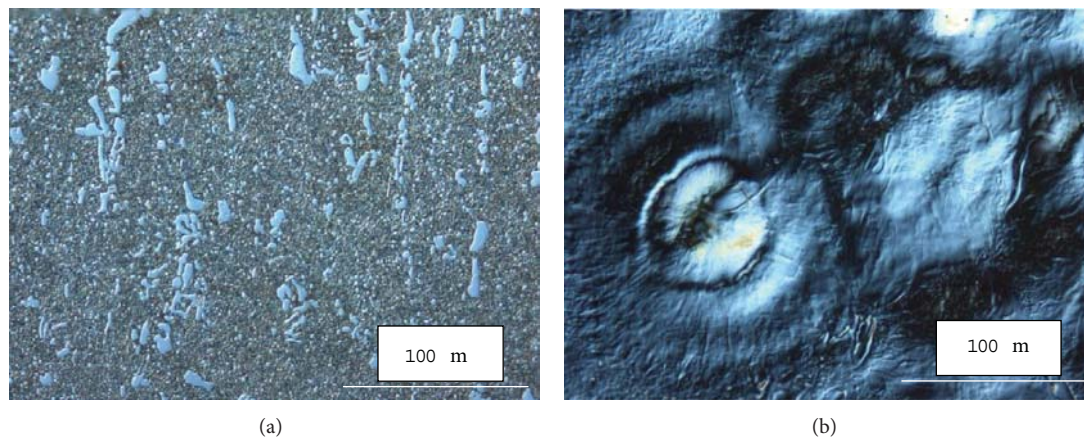


FIGURE 7: Optical morphologies of the D2 samples: as initial (a), treated sample D2-1 (b).

of samples was significantly improved after the LEHCPEB treatment. The best corrosion resistance in this study was found to be the sample treated with 20 pulses.

The crater formation and related surface purification effect are believed to be the main reasons for the improved corrosion resistance. At the early stage of the treatment, typically 5 pulses in our case, eruption usually occurs on the top surface, since there are a large amount of inclusions/second-phase particles. With the increased number of pulses, the particle density on the top surface decreases due to the eruption events as well as their dissolution within the melt. This reduction of particle density leads to a lower amount of available nucleation sites for new eruption events and, consequently, the crater formation on the top surface is more difficult. Since the solidification rate is very fast, “solute trapping” occurs under cooling after the dissolution of the particles and results in the homogenization of the chemistry in the resolidified melted layer. This removes the Cr-depleted zone generally

present at the material surface [8] and enhances the corrosion resistance. The best corrosion properties are obtained after a sufficient number of LEHCPEB pulses—typically 20 pulses here—that can provide with the combination of (i) the formation of a chemically homogeneous film and (ii) the absence of surface craters.

By using the LEHCPEB treatment, rapid surface alloying of the 316L stainless steel with Ti has been successfully achieved. The results showed that the corrosion resistance of the steel can be further improved by introducing Ti into the top surface layer of the stainless steel [42].

3.2. Improving Corrosion Resistance of D2 Steel by LEHCPEB. The pulsed electron beam treatment parameters for the D2 steel samples are shown in Table 1. Here, the number of pulses is set as 20 for all the samples, while the accelerating voltage is changed. Figures 7(a) and 7(b) give the typical optical images

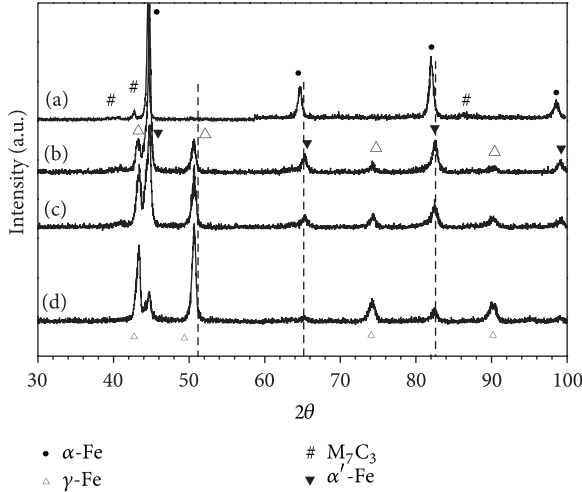


FIGURE 8: XRD patterns of the untreated and treated D2 steel samples, as received (a), D2-1 (b), D2-2 (c), and D2-3 (d).

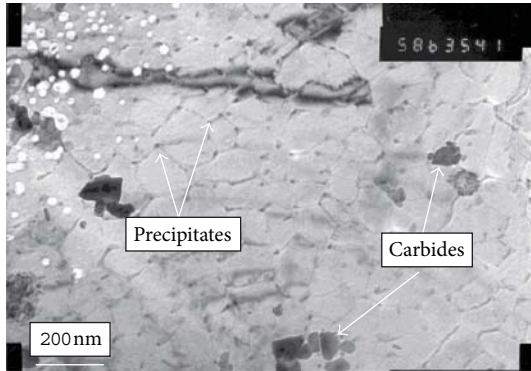


FIGURE 9: Typical bright field TEM micrograph taken in the melted layer of the 25-pulse D2 steel sample.

of the untreated and treated D2 steel (D2-1) samples. It can be clearly seen that large carbides are present in the untreated sample (Figure 7(a)). After the treatment, craters are formed on the surface (Figure 7(b)), which are the results of eruptions occurring at the carbides. Indeed, the carbides have lower melting point and heat conductivity than the α ferrite matrix. Therefore, during the treatment process, the carbides melt before the rest of the material. Just below the surface, the melting expansion induces an eruption event, as described in more detail elsewhere [34, 43].

Figure 8 shows the XRD traces of the samples before and after the LEHCPEB treatments. The starting material contained two phases: ferrite (α -Fe) and carbide having the Cr_7C_3 structure. The volume fraction of the carbide is fairly important, and the carbide peaks are clearly visible in the XRD trace of the starting material. The intensity of the X-ray diffraction peaks also indicates that the major phase in the initial material was α -ferrite. After the LEHCPEB bombardment, the XRD traces are observed to change somehow dramatically. Concerning the Cr_7C_3 phase, it is clear that the carbide peaks tend to disappear after the LEHCPEB

TABLE 1: LEHCPEB treatment parameters of the D2 steel samples.

Specimens	Energy (kV)	Distance (mm)	Pulses (times)
D2-1	18.00	140	20
D2-2	21.50	140	20
D2-3	27.80	140	20

TABLE 2: Corrosion data of the untreated and treated D2 steel samples in 3.5% NaCl solution.

Samples	E_{corr} (mV)	i_{corr} ($\mu\text{A}/\text{cm}^2$)	R_p ($\text{k}\Omega/\text{cm}^2$)
As initial	-720.38	0.29	74.37
D2-1	-451.45	0.23	93.06
D2-2	-470.77	0.21	101.27
D2-3	-478.14	0.20	105.69

treatments. Concerning the α phase, it is interesting to note that some of the peaks in the treated samples have close neighbours. A splitting of the (200) peak is usually found in newly formed martensite having sufficient amount of C to reveal its quadraticity. Finally, some new peaks are present in the XRD traces. They were verified to be from the γ -Fe phase. The peak intensity of the γ -Fe phase increases with the accelerating voltage, indicating that the volume fraction of the γ phase detected by XRD increases [44, 45].

The corrosion resistance of the D2 steels samples was measured in the 3.5% NaCl water solution. The corrosion data calculated from potentiodynamic polarization tests are summarized in Table 2. It can be found that the corrosion potential (E_{corr}) becomes nobler after the LEHCPEB treatment, while the corrosion current (i_{corr}) decreases. As a result, the calculated polarization resistance (R_p) increases after the LEHCPEB treatment. The best corrosion resistance is found in the D2 steel sample treated with the highest accelerating voltage (D2-3).

The corrosion resistance of D2 steel is closely related to the formation of austenite in the surface layer. From the phase diagram, it can be established that the primary phase in solidification for the D2 steel should be γ . However, the local composition depends on the ability of electron beam to homogenize the surface layer. When the accelerating voltage is low, that is, low beam energy density, the melting duration of the surface layer is very short. As a result, the large carbides cannot be completely dissolved in the melt. During cooling, martensitic transformation will occur in the C lean austenite. When high-accelerating voltage is applied, the melt duration at the top surface layer is sufficient long for carbides to be completely dissolved. The austenite layer formed in the melted layer will be stabilized by C and retained at room temperature. Figure 9 shows a typical TEM bright field image of the austenite layer formed in a D2 steel sample treated by 25 pulses [34]. It is clearly seen that the austenite phase has a cell-like structure with a cell size of about 100~200 nm. Besides, some nanoscale carbides and precipitates are also visible at the boundary or the triple junctions of the cells. Such kind

of nanocell/grain structure was also observed in other steels, Mg, Al alloys treated by pulsed electron beams [46–50]. The presence of these metastable homogeneous layers with special nanostructures formed by the LEHCPEB treatment at the top surface accounts for the improved corrosion resistance of the treated samples. The advantages of the LEHCPEB treatment over other conventional surface treatment techniques lie in (i) the formation of homogeneous surface layers having nanostructures after a sufficient number of pulses [30–36]; (ii) the strong metallurgical binder between treated layers and the substrate [25, 32–34]; and (iii) the thick modified layer after the LEHCPEB treatment [25, 26, 36, 38]. Therefore, the LEHCPEB technique is a promising approach in improving the surface properties of metallic materials, especially their corrosion resistance.

4. Summary

The modifications in microstructures and corrosion after low energy high current pulsed electron beam (LEHCPEB) surface treatment have been shown in the case of steels. The results obtained here for the AISI 316L stainless steel and AISI D2 steel clearly confirm the high potential of the LEHCPEB technique for improving the corrosion resistance; in particular if the number of pulses and/or the beam energy is sufficiently high. The crater eruption-induced purification effect and the formations of homogenized layer and nanostructures are believed to be the main reasons accounting for the improved corrosion resistance of steels after the LEHCPEB treatment.

Acknowledgments

Professor K. M. Zhang would like to acknowledge the support of Top Discipline Plan for Mechanical Engineering of Shanghai Municipal Education Commission (YLJX12-2). This work is supported by the Special Foundation of the Shanghai Science and Technology Committee for Nanomaterials Research (no. 1052nm05000) and National Natural Science Foundation (nos. 51101096, 51271121). Professor T. Grosdidier would also like to acknowledge the “Sea-Sky” professorship position provided by the Dalian University of Technology. Finally, Professor T. Grosdidier and J. X. Zou would like to acknowledge the framework of the Labex DAMAS within which this work was carried out.

References

- [1] A. S. Cushman and H. A. Gardner, *The Corrosion and Preservation of Iron and Steel*, McGraw-Hill, New York, NY, USA, 1910.
- [2] M. G. Fontana and N. D. Greene, *Corrosion Engineering*, McGraw-Hill, New York, NY, USA, 1967.
- [3] K. R. Trethewey and J. Chamberlain, *Corrosion for Students of Science and Engineering*, Longman Scientific and Technical, Burnt Mill, UK, 1988.
- [4] P. R. Roberge, *Corrosion Basics: An Introduction*, NACE Press, 2nd edition, 2006.
- [5] K. H. Lo, C. H. Shek, and J. K. L. Lai, “Recent developments in stainless steels,” *Materials Science and Engineering R: Reports*, vol. 65, no. 4–6, pp. 39–104, 2009.
- [6] G. Wranglen, “Pitting and sulphide inclusions in steel,” *Corrosion Science*, vol. 14, no. 5, pp. 331–349, 1974.
- [7] G. S. Eklund, “Initiation of pitting at sulfide inclusions in stainless steel,” *Journal of the Electrochemical Society*, vol. 121, no. 4, pp. 467–473, 1974.
- [8] M. P. Ryan, D. E. Williams, R. J. Chater, B. M. Hutton, and D. S. McPhail, “Why stainless steel corrodes,” *Nature*, vol. 415, no. 6873, pp. 770–774, 2002.
- [9] C. Bindal and A. H. Ucisik, “Characterization of boriding of 0.3%C, 0.02% P plain carbon steel,” *Vacuum*, vol. 82, no. 1, pp. 90–94, 2007.
- [10] A. Pertek and M. Kulka, “Two-step treatment carburizing followed by boriding on medium-carbon steel,” *Surface and Coatings Technology*, vol. 173, no. 2–3, pp. 309–314, 2003.
- [11] B. Selçuk, R. Ipek, M. B. Karamiş, and V. Kuzucu, “An investigation on surface properties of treated low carbon and alloyed steels (bonding and carburizing),” *Journal of Materials Processing Technology*, vol. 103, no. 2, pp. 310–317, 2000.
- [12] A. A. Novakova, I. G. Sizov, D. S. Golubok, T. Y. Kiseleva, and P. O. Revokatov, “Electron-beam boriding of low-carbon steel,” *Journal of Alloys and Compounds*, vol. 383, no. 1–2, pp. 108–112, 2004.
- [13] T. M. Yue, J. K. Yu, and H. C. Man, “The effect of excimer laser surface treatment on pitting corrosion resistance of 316LS stainless steel,” *Surface and Coatings Technology*, vol. 137, no. 1, pp. 65–71, 2001.
- [14] I. Manna, J. Dutta Majumdar, B. Ramesh Chandra, S. Nayak, and N. B. Dahotre, “Laser surface cladding of Fe-B-C, Fe-B-Si and Fe-BC-Si-Al-C on plain carbon steel,” *Surface and Coatings Technology*, vol. 201, no. 1–2, pp. 434–440, 2006.
- [15] C. J. Wang and C. C. Li, “Corrosion behaviors of AISI 1025 steels with electroless nickel/aluminized coatings in NaCl-induced hot corrosion,” *Surface and Coatings Technology*, vol. 177–178, pp. 37–43, 2004.
- [16] J. S. Chen, J. G. Duh, and F. B. Wu, “Microhardness and corrosion behavior in CrN / electroless Ni / mild steel complex coating,” *Surface and Coatings Technology*, vol. 150, no. 2–3, pp. 239–245, 2002.
- [17] B. F. Chen, W. L. Pan, G. P. Yu, J. Hwang, and J. H. Huang, “On the corrosion behavior of TiN-coated AISI D2 steel,” *Surface and Coatings Technology*, vol. 111, no. 1, pp. 16–21, 1999.
- [18] E. Lunarska, N. Ageeva, and J. Michalski, “Corrosion resistance of plasma-assisted chemical vapour deposition (PACVD) TiN-coated steel in a range of aggressive environments,” *Surface and Coatings Technology*, vol. 85, no. 3, pp. 125–130, 1996.
- [19] J. Creus, H. Idrissi, H. Mazille, F. Sanchette, and P. Jacquot, “Improvement of the corrosion resistance of CrN coated steel by an interlayer,” *Surface and Coatings Technology*, vol. 107, no. 2–3, pp. 183–190, 1998.
- [20] L. A. S. Ries, D. S. Azambuja, and I. J. R. Baumvol, “Corrosion resistance of steel coated with Ti/TiN multilayers,” *Surface and Coatings Technology*, vol. 89, no. 1–2, pp. 114–120, 1997.
- [21] C. Liu, Q. Bi, and A. Matthews, “EIS comparison on corrosion performance of PVD TiN and CrN coated mild steel in 0.5 N NaCl aqueous solution,” *Corrosion Science*, vol. 43, no. 10, pp. 1953–1961, 2001.
- [22] E. Cano, L. Martínez, J. Simancas, F. J. Pérez-Trujillo, C. Gómez, and J. M. Bastidas, “Influence of N, Ar and Si ion implantation

- on the passive layer and corrosion behaviour of AISI 304 and 430 stainless steels," *Surface and Coatings Technology*, vol. 200, no. 16-17, pp. 5123-5131, 2006.
- [23] N. Mottu, M. Vayer, J. Dudognon, and R. Erre, "Structure and composition effects on pitting corrosion resistance of austenitic stainless steel after molybdenum ion implantation," *Surface and Coatings Technology*, vol. 200, no. 7, pp. 2131-2136, 2005.
- [24] F. J. Pérez, E. Otero, M. P. Hierro et al., "High temperature corrosion protection of austenitic AISI 304 stainless steel by Si, Mo and Ce ion implantation," *Surface and Coatings Technology*, vol. 108-109, no. 1-3, pp. 127-131, 1998.
- [25] D. I. Proskurovsky, V. P. Rotshtein, G. E. Ozur et al., "Pulsed electron-beam technology for surface modification of metallic materials," *Journal of Vacuum Science and Technology A*, vol. 16, no. 4, pp. 2480-2488, 1998.
- [26] D. I. Proskurovsky, V. P. Rotshtein, G. E. Ozur, Y. F. Ivanov, and A. B. Markov, "Physical foundations for surface treatment of materials with low energy, high current electron beams," *Surface and Coatings Technology*, vol. 125, no. 1-3, pp. 49-56, 2000.
- [27] A. D. Pogrebnjak, V. S. Ladysev, N. A. Pogrebnjak et al., "Comparison of radiation damage and mechanical and tribological properties of α -Fe exposed to intense pulsed electron and ion beams," *Vacuum*, vol. 58, no. 1, pp. 45-52, 2000.
- [28] A. N. Valyaev, V. S. Ladysev, A. D. Pogrebnjak, A. A. Valyaev, and S. V. Plotnikov, "Comparative analysis of radiation damages, mechanical and tribological properties of α -Fe exposed to intense-pulsed electron and ion beams," *Nuclear Instruments and Methods in Physics Research B*, vol. 161, pp. 1132-1136, 2000.
- [29] B. Gao, S. Hao, J. Zou et al., "High current pulsed electron beam treatment of AZ31 Mg alloy," *Journal of Vacuum Science and Technology A*, vol. 23, no. 6, pp. 1548-1553, 2005.
- [30] J. X. Zou, K. M. Zhang, C. Dong, Y. Qin, S. Hao, and T. Grosdidier, "Selective surface purification via crater eruption under pulsed electron beam irradiation," *Applied Physics Letters*, vol. 89, no. 4, Article ID 041913, 3 pages, 2006.
- [31] K. M. Zhang, D. Z. Yang, J. X. Zou, T. Grosdidier, and C. Dong, "Improved in vitro corrosion resistance of a NiTi alloy by high current pulsed electron beam treatment," *Surface and Coatings Technology*, vol. 201, no. 6, pp. 3096-3102, 2006.
- [32] K. Zhang, J. Zou, T. Grosdidier, C. Dong, and D. Yang, "Improved pitting corrosion resistance of AISI 316L stainless steel treated by high current pulsed electron beam," *Surface and Coatings Technology*, vol. 201, no. 3-4, pp. 1393-1400, 2006.
- [33] J. X. Zou, T. Grosdidier, B. Bolle, K. M. Zhang, and C. Dong, "Texture and microstructure at the surface of an AISI D2 steel treated by high current pulsed electron beam," *Metallurgical and Materials Transactions A*, vol. 38, no. 9, pp. 2061-2071, 2007.
- [34] J. Zou, T. Grosdidier, K. Zhang, and C. Dong, "Mechanisms of nanostructure and metastable phase formations in the surface melted layers of a HCPEB-treated D2 steel," *Acta Materialia*, vol. 54, no. 20, pp. 5409-5419, 2006.
- [35] C. Dong, A. Wu, S. Hao et al., "Surface treatment by high current pulsed electron beam," *Surface and Coatings Technology*, vol. 163-164, pp. 620-624, 2003.
- [36] S. Z. Hao, B. Gao, A. M. Wu et al., "Surface modification of steels and magnesium alloy by high current pulsed electron beam," *Nuclear Instruments and Methods in Physics Research B*, vol. 240, no. 3, pp. 646-651, 2005.
- [37] R. C. Newman, "Beyond the kitchen sink," *Nature*, vol. 415, no. 6873, pp. 743-744, 2002.
- [38] S. Hao, P. Wu, J. Zou, T. Grosdidier, and C. Dong, "Microstructure evolution occurring in the modified surface of 316L stainless steel under high current pulsed electron beam treatment," *Applied Surface Science*, vol. 253, no. 12, pp. 5349-5354, 2007.
- [39] K. M. Zhang, J. X. Zou, T. Grosdidier et al., "Mechanisms of structural evolutions associated with the high current pulsed electron beam treatment of a NiTi shape memory alloy," *Journal of Vacuum Science and Technology A*, vol. 25, no. 1, pp. 28-36, 2007.
- [40] C. H. Hsu and F. Mansfeld, "Concerning the conversion of the constant phase element parameter Y_0 into a capacitance," *Corrosion*, vol. 57, no. 9, pp. 747-748, 2001.
- [41] G. E. Cavigliasso, M. J. Esplandiu, and V. A. Macagno, "Influence of the forming electrolyte on the electrical properties of tantalum and niobium oxide films: an EIS comparative study," *Journal of Applied Electrochemistry*, vol. 28, no. 11, pp. 1213-1219, 1998.
- [42] K. M. Zhang, J. X. Zou, T. Grosdidier, C. Dong, and S. Weber, "Ti surface alloying of an AISI 316L stainless steel by low energy high current pulsed electron beam treatment," *Journal of Vacuum Science and Technology A*, vol. 26, no. 6, pp. 1407-1414, 2008.
- [43] J. X. Zou, T. Grosdidier, B. Bolle, K. M. Zhang, and C. Dong, "Texture and microstructure at the surface of an AISI D2 steel treated by high current pulsed electron beam," *Metallurgical and Materials Transactions A*, vol. 38, no. 9, pp. 2061-2071, 2007.
- [44] Q. F. Guan, H. Zou, G. T. Zou et al., "Surface nanostructure and amorphous state of a low carbon steel induced by high-current pulsed electron beam," *Surface and Coatings Technology*, vol. 196, no. 1-3, pp. 145-149, 2005.
- [45] G. Z. Tang, F. J. Xu, G. H. Fan, X. X. Ma, and L. Q. Wang, "Mechanisms of microstructure formations in M50 steel melted layer by high current pulsed electron beam," *Nuclear Instruments and Methods in Physics Research B*, vol. 288, pp. 1-5, 2012.
- [46] K. M. Zhang, J. X. Zou, T. Grosdidier, and C. Dong, "Crater formation induced metastable structure in an AISI D2 steel treated with a pulsed electron beam," *Vacuum*, vol. 86, pp. 1273-1277, 2012.
- [47] J. X. Zou, K. M. Zhang, S. Z. Hao, C. Dong, and T. Grosdidier, "Mechanisms of hardening, wear and corrosion improvement of 316 L stainless steel by low energy high current pulsed electron beam surface treatment," *Thin Solid Films*, vol. 519, no. 4, pp. 1404-1415, 2010.
- [48] Y. Hao, B. Gao, G. F. Tu, H. Cao, S. Z. Hao, and C. Dong, "Surface modification of Al-12. 6Si alloy by high current pulsed electron beam," *Applied Surface Science*, vol. 258, no. 6, pp. 2052-2056, 2012.
- [49] Y. Hao, B. Gao, G. F. Tu, S. W. Li, S. Z. Hao, and C. Dong, "Surface modification of Al-20Si alloy by high current pulsed electron beam," *Applied Surface Science*, vol. 257, no. 9, pp. 3913-3919, 2011.
- [50] K. M. Zhang and J. X. Zou, "Formation of ultrafine twinned austenite on a cold rolled 316L stainless steel induced by pulsed electron beam treatment under heating mode," *Thin Solid Films*, vol. 526, pp. 28-33, 2012.

Research Article

Antibacterial TiO₂ Coating Incorporating Silver Nanoparticles by Microarc Oxidation and Ion Implantation

Peng Zhang,¹ Zhiguo Zhang,² and Wei Li²

¹ School of Materials Science and Engineering, South China University of Technology, Guangzhou 510640, China

² Department of Materials Science and Engineering, Jinan University, Guangzhou 510632, China

Correspondence should be addressed to Wei Li; liweijn@yahoo.com.cn

Received 6 November 2012; Accepted 6 December 2012

Academic Editor: Jianxin Zou

Copyright © 2013 Peng Zhang et al. This is an open access article distributed under the Creative Commons Attribution License, which permits unrestricted use, distribution, and reproduction in any medium, provided the original work is properly cited.

Infection associated with titanium implants remains the most common serious complication in hard tissue replacement surgery. Since such postoperative infections are usually difficult to cure, it is critical to find optimal strategies for preventing infections. In this study, TiO₂ coating incorporating silver (Ag) nanoparticles were fabricated on pure titanium by microarc oxidation and ion implantation. The antibacterial activity was evaluated by exposing the specimens to *Staphylococcus aureus* and comparing the reaction of the pathogens to Ti-MAO-Ag with Ti-MAO controls. Ti-MAO-Ag clearly inhibited bacterial colonization more than the control specimen. The coating's antibacterial ability was enhanced by increasing the dose of silver ion implantation, and Ti-MAO-Ag20.0 had the best antibacterial ability. In addition, cytocompatibility was assessed by culturing cell colonies on the specimens. The cells grew well on both specimens. These findings indicate that surface modification by means of this process combining MAO and silver ion implantation is useful in providing antibacterial activity and exhibits cytocompatibility with titanium implants.

1. Introduction

Titanium- (Ti-) based implants are widely used in the surgical domain as hard tissue replacements due to their relatively low elastic modulus, good fatigue strength, formability, corrosion resistance, and high biocompatibility [1]. However, the maintenance of bioinertness and the prevention of toxic metal ion release are becoming key challenges to the safety of implants in the human body. For this reason, numerous strategies have been developed to produce favorable surfaces on the implants which not only help to retain the excellent bulk properties of titanium during a long life cycle but also favor the prevention or delay of toxic metal ion release [2–6].

Nowadays, stricter antibacterial requirements of implants have been urgently demanded for clinical use. Bacterial infection associated with implants has become a growing threat to human health, as it may cause various complications such as swelling, tenderness, erythema, extensive soft tissue trauma, warmth, and diminished range of joint motion, leaving patients suffering from prolonged morbidity, extended rehabilitation, and repeated debridement and surgery [7–11].

Moreover, such infections are usually difficult to treat, which motivates people to develop various methods to prevent infections rather than treat them. However, in spite of the great efforts made to mitigate bacterial contamination such as thorough disinfection and strict aseptic surgical operation schemes, bacterial invasion and complications still occur in the nearby tissues after implant surgery [12, 13]. On the other hand, several biomaterial surface modification approaches have been attempted to improve the antibacterial ability of the implant and have demonstrated great progresses in reducing the incidence of implant-associated infections [12].

The infections associated with implants are characterized by bacterial colonization and biofilm formation on the implanted device as well as infection of the adjacent tissues. It is generally accepted that the most effective way to prevent biofilm buildup on implants is to prohibit the initial bacterial adhesion, as the biofilms are quite difficult to remove after formation. Therefore, postoperative infection rates may be greatly reduced through improving the antimicrobial properties of the implant surface by means of surface modifications. Antibacterial surfaces were originally produced by direct

impregnation with antibiotics, with the purpose of preventing the initial adhesion of bacteria onto the implant surface [7–10, 14–17]. However, although these antibiotic-loaded surfaces demonstrated superior curative effects, potential toxicity and increased bacterial drug resistance due to the slow-release doses have become new increased risks in surgery [8]. In addition to antibiotic-releasing coatings, research interest has also focused on developing covalently bonded drugs to realize long-lasting antibacterial ability. However, the susceptibility of bacteria to drugs in the vicinity of implants presents a problem, and drug resistance of bacteria isolated from implants has been reported [8, 18].

Recently, silver-containing coatings have attracted increasing attention due to the nontoxicity of the active Ag^+ to human cells and its antimicrobial activity [8, 19, 20]. Ag^+ is a strong bactericide with satisfactory stability and presents significant broad spectrum antimicrobial effects on both gram-positive and gram-negative bacteria [20]. The antibacterial effect can last for a long time and can be less prone to producing antibacterial resistance [20, 21]. Moreover, silver-containing coatings could inhibit bacterial attachment onto the implants [21]. *In vitro* studies demonstrate excellent biocompatibility of silver-containing coatings without genotoxicity or cytotoxicity [22]. *In vivo* studies, on the other hand, indicate that silver-containing coatings have no local or systemic side-effects [20–22].

The required Ag dose in the implants is typically low, which makes it possible to introduce Ag into biocompatible coatings. In fact, various well-established techniques such as plasma ion implantation have been proposed to produce silver-containing coatings [23]. By incorporating a sufficient amount of Ag to enhance the antibacterial ability of porous coatings, a surface that retains biocompatibility and relatively long-term antibacterial ability can be produced. In this study, the silver was introduced by an ion implantation method into TiO_2 coatings produced by microarc oxidation (MAO). MAO on the surface of titanium implants can provide a porous biofunctional TiO_2 coating with good adhesion to the substrate and high apatite-forming ability [6, 24–29]. The incorporation of Ag was expected to improve the antibacterial ability of the TiO_2 coatings. The microstructure, the antimicrobial properties, and the biocompatibility of the TiO_2 coatings in which Ag was implanted were investigated in detail.

2. Materials and Methods

2.1. Coating Specimen Preparation. Commercially available pure titanium alloys (TA2) were used as specimens. The titanium specimens were cut into plates with dimensions of $15 \times 10 \times 2$ mm. The surfaces of the plates were abraded with emery papers of 200, 400, 600, 800, and 1200 grit in turn and washed in an ultrasonic bath for 20 min with acetone, ethanol, and deionized water, respectively. The titanium plates were then dried in an oven at room temperature.

MAO was carried out on the Ti plates with an AC-type high power supply (PN-III). The plates served as the anode electrode and a stainless steel plate was used

as the counter electrode. The electrolyte was 0.2 M calcium acetate monohydrate ($(\text{CH}_3\text{COO})_2\text{Ca} \cdot \text{H}_2\text{O}$, CA) and 0.02 M β -glycerophosphoric acid disodium salt pentahydrate ($\text{C}_3\text{H}_7\text{Na}_2\text{O}_6\text{P} \cdot 5\text{H}_2\text{O}$, β -GP). After treatment at 350 V for 5 minutes, porous TiO_2 coatings formed on the plate surface. The thickness of the oxide coating ranged from 12 μm to 20 μm and the average diameter of the pore size was 5 to 10 μm .

2.2. Silver Ion Implantation. Silver ion implantation was performed using an ion implantation machine equipped with a metal vapor vacuum arc (MEVVA) ion source. The initial gas pressure in the ion implantation chamber was under 2×10^{-3} Pa. Silver was implanted into the TiO_2 coatings with an acceleration energy of 65 keV. The silver implantation doses were 1.0, 5.0, 10.0, and 20.0×10^{17} ions/ cm^2 , respectively. The corresponding samples were denoted as Ti-MAO-Ag1.0, Ti-MAO-Ag5.0, Ti-MAO-Ag10.0, and Ti-MAO-Ag20.0, respectively.

2.3. In Vitro Antimicrobial Properties. The antibacterial activities of the silver-containing coatings were characterized based on the American Society for Testing and Materials (ASTM) G21-1996 (“Standard Practice for Determining Resistance of Synthetic Polymeric Materials to Fungi”). Gram-positive *Staphylococcus aureus* (ATCC 6538) was used to evaluate the antibacterial ability of the silver-containing coatings since staphylococci mainly account for infections of both temporarily and permanently implanted orthopedic devices. All the specimens and petri dishes were sterilized by autoclave at 121°C for 1 h. Afterwards, bacteria solution with a concentration of 5.6×10^6 CFU/mL was dripped onto the sample surface. The specimens were covered by plastic film in a sterile dish and incubated at 37°C for 24 h. Each specimen and its covered film were washed with 5 mL of stroke-physiological saline solution. The wash eluate was collected and diluted to 1:50 with saline solution. Then 100 μL of the diluted solution was incubated on a standard culture plate containing LB broth (10 g/L tryptone, 5 g/L yeast extract, 10 g/L NaCl). After further incubation at 37°C for 24 h, the active bacteria were counted and the antibacterial rate was calculated using the following formula:

$$R = \frac{(B - A)}{B} \times 100\%, \quad (1)$$

where R is the antibacterial rate (%), B is the average number of viable bacteria on the corresponding MAO titanium specimen without Ag ion implantation which is consistent with the control group, and A is the average number of viable bacteria on the Ag-ion-implanted MAO specimen. The measurement was repeated three times for *S. aureus* culture.

2.4. Cell Culture. The 3T3 cell line (Chinese hamster fibroblasts) was used for cytotoxicity tests. The culture medium consisted of alpha-minimum essential medium (α -MEM) supplemented with 10% fetal calf serum (FBS), 100 U mL^{-1} of penicillin, and $100 \mu\text{g mL}^{-1}$ of streptomycin sulfate. Experiments were conducted in an incubator at 37°C with

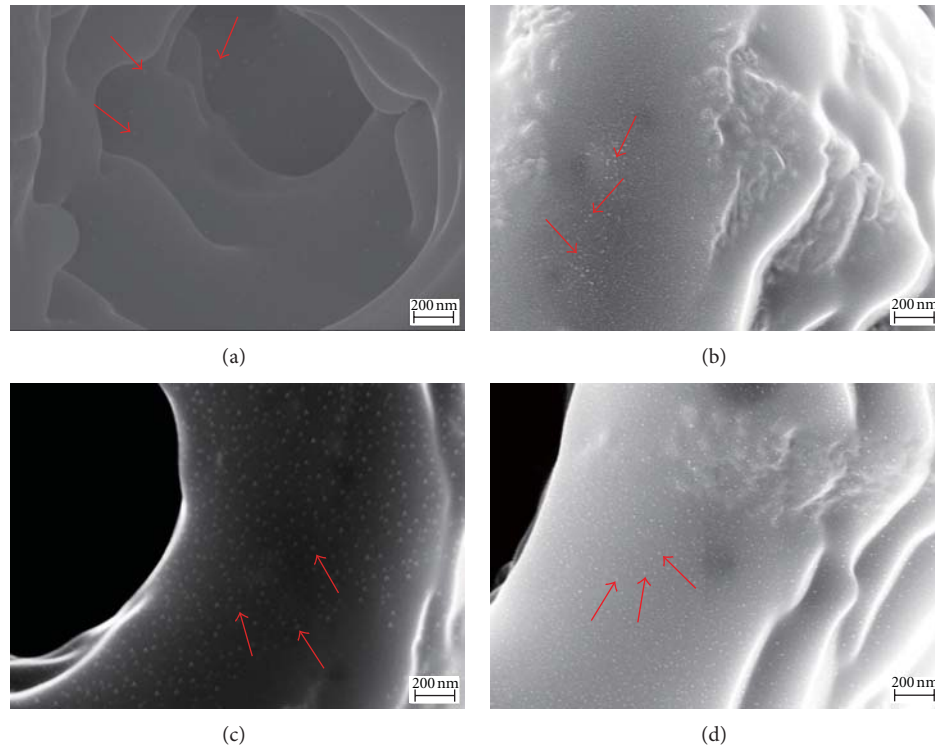


FIGURE 1: Surface morphologies for different specimens with various implanted Ag doses on MAO coating surfaces: (a) Ti-MAO-Ag1.0, (b) Ti-MAO-Ag5.0, (c) Ti-MAO-Ag10.0, and (d) Ti-MAO-Ag20.0.

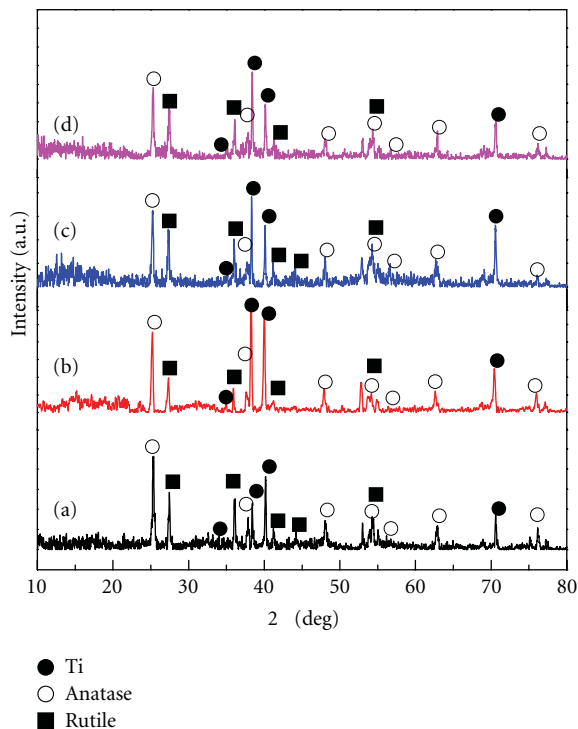


FIGURE 2: XRD patterns of samples with different implanted Ag doses: (a) Ti-MAO-Ag1.0, (b) Ti-MAO-Ag5.0, (c) Ti-MAO-Ag10.0, and (d) Ti-MAO-Ag20.0.

a humidified atmosphere of 95% air and 5% CO_2 for 24 h. The specimens were sterilized by heating at 180°C for 1 h. The cells were fixed with 5 mL of 10% formalin for 30 min, stained with 8 mL of 0.15% methylene blue for an additional 30 min, washed thoroughly with different concentration alcohol strictly, and dried [30].

2.5. Microstructure and Surface Analyses. The surface morphologies of the coatings were examined by scanning electron microscopy (SEM, Zeiss SUPRA 40, Germany). The crystalline structure was characterized by X-ray diffraction (XRD, D/Max 2400 V, Rigaku, Tokyo, Japan) using Cu K_α radiation in the 2θ range of $10\text{--}80^\circ$ with an accelerating voltage of 36 kV and a current of 100 mA. The chemical composition of the surface layer was analyzed by energy dispersive spectrometry (EDS).

3. Results and Discussion

The SEM top-morphology images of the coatings incorporating different doses of silver are shown in Figure 1. The typical porous surfaces on MAO-treated pure titanium can be clearly seen, indicating that the implantation of Ag had little effect on the surface morphology of the TiO_2 coating formed. The implanted Ag presented in the form of nanoparticles distributed homogeneously on the surface and even inside the open pores. Inspection of the porous coating surfaces

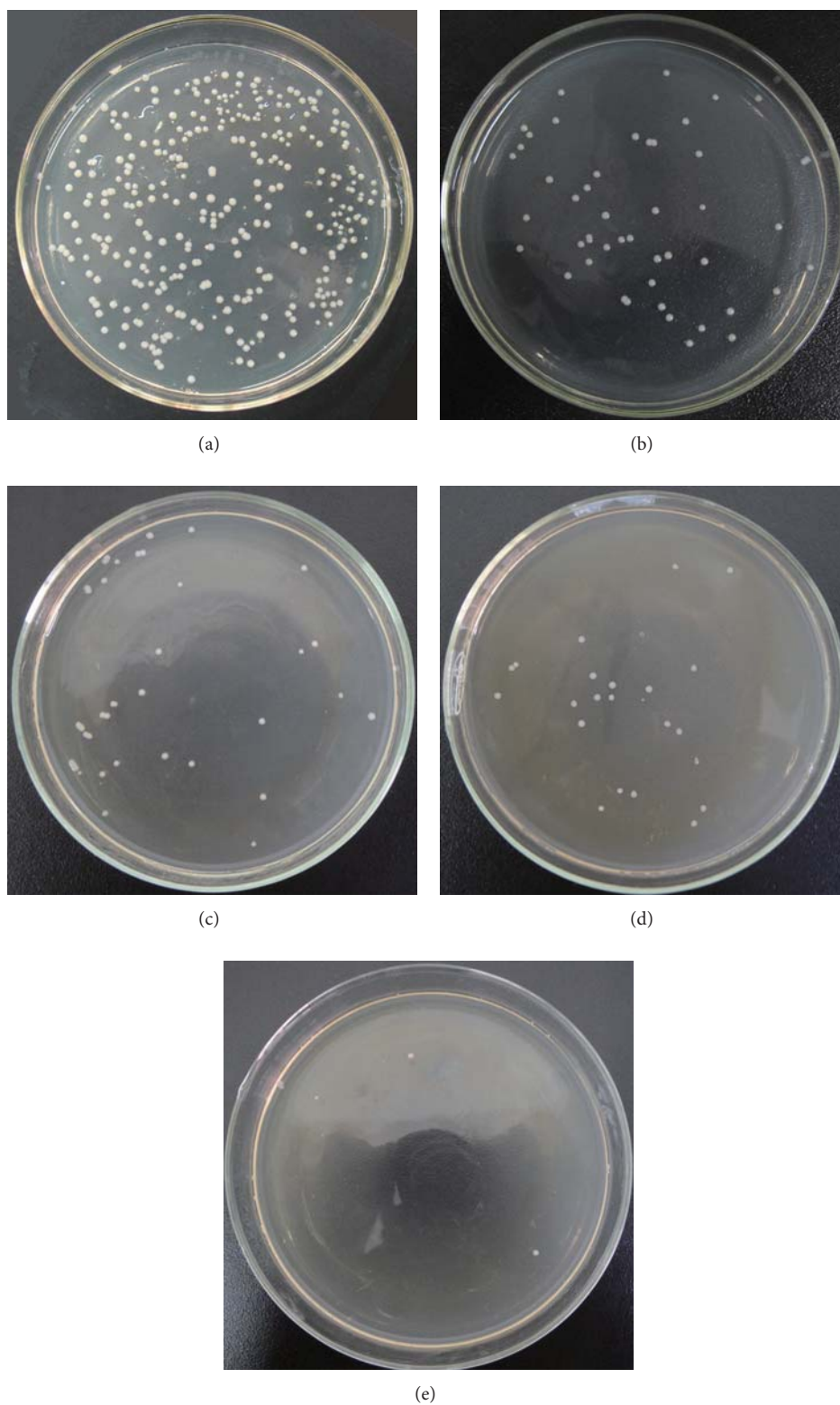


FIGURE 3: Photos of culture plates after antibacterial tests against *Staphylococcus aureus*: (a) control specimen Ti-MAO, (b) Ti-MAO-Ag1.0, (c) Ti-MAO-Ag5.0, (d) Ti-MAO-Ag10.0, and (e) Ti-MAO-Ag20.0.

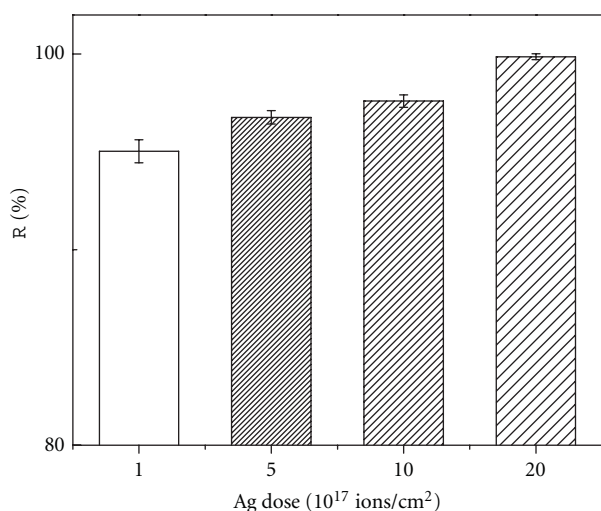


FIGURE 4: Antibacterial rate (R) evolution with the incorporated Ag doses.

with different implanted doses shows that the amount of Ag nanoparticles on the porous coating surfaces increased with increases in the dose implanted.

Figure 2 exhibits the XRD patterns of the specimens with different doses of implanted silver. Only the peaks related to the anatase and rutile phases and the phase from the Ti substrate can be indexed for all the specimens. The peaks of Ag or Ag alloys do not appear, confirming that the Ag was present as nanoparticles. The results are contrary to those reported by other research groups [19, 31], who found that the weak Ag diffraction peaks could be identified although the Ag particles were in the nanocrystalline form. The difference could be attributed to the amounts of silver incorporated and the methods of incorporation. The ion implantation technique demonstrated the unique advantage of providing a superfine nanoparticle in contrast to the other methods of incorporation.

EDS composition analysis indicated that the incorporated Ag content on the sample surface increases with increasing the ion implantation doses of Ag, as shown in Table 1, which is consistent with the SEM observations.

The antibacterial ability of MAO coatings in which Ag was implanted was investigated by growing *S. aureus* colonies on LB plates. The MAO coatings incorporating Ag present strong inhibition of *S. aureus* colony formation compared to the MAO coating without incorporated Ag, where significant amounts of colonies were found (see Figure 3(a)). In contrast, nearly no viable bacteria could be seen on Ti-MAO-Ag20.0 (Figure 3(e)). Moreover, the number of bacteria that could be seen decreased as the dose of Ag incorporated increased, suggesting that the antibacterial ability increased with the content of incorporated Ag. The detailed calculation of the antibacterial rate shown in Figure 4 demonstrates that the antibacterial rate increases with increases in the dose of Ag incorporated from 95.8% to nearly 100%. The results are in good accordance with a previous report [19], where TiO₂ nanotubes incorporating Ag demonstrated superior

antibacterial ability by killing all the planktonic bacteria in the suspension during the first few days.

However, the mechanism of inhibitory action of silver ions on microorganisms remains controversial. It is proposed that DNA loses its replication ability and cellular proteins become inactivated by the reaction with Ag [32, 33]. Other research results showed that Ag⁺ bound to functional groups of proteins, resulting in protein denaturation [32]. Concerning the mechanism of how the silver nanoparticles act as biocidal material against *S. aureus*, some reports have suggested that electrostatic attraction between negatively charged bacterial cells and positively charged nanoparticles is crucial for the activity of nanoparticles as bactericidal materials [34]. However, there are also contradictory reports revealing that, despite the negative charge on the silver nanoparticle surfaces, silver nanoparticles present good antibacterial activity by interacting directly with “building elements” of the bacterial membrane structure, resulting in structural change in the bacterial membrane, degradation, and finally cell death [32]. This mechanism has been verified in a series of studies [32, 35–37], which would explain the good antibacterial ability observed in this study.

The cytotoxicity of the specimens was evaluated by observing the morphology of the 3T3 cell colony formation. The formation of normal fibroblasts with a spindle-like shape was observed on the surfaces of all samples (Figure 5). The morphologies of the fibroblasts show little difference when comparing the samples with and without Ag implantation, indicating that the Ag-containing coatings demonstrated similar biocompatibility to the titanium treated directly by MAO. The latter has been reported to demonstrate superior biocompatibility and no cytotoxicity [38, 39].

Toxicity from silver has been observed in the form of argyria only when there are large open wounds and large amounts of silver ions have been used for dressing. Reports of silver allergy are scarce in the literature. On the contrary, most studies propose that silver nanoparticles are non-toxic. However, with respect of their small size and variable properties, it is suggested that they are hazardous to the environment of the human body [21, 40]. Hussain et al. [41] studied the toxicity of silver nanoparticles of different sizes in a rat liver cell line. They reported that abnormal size, cellular shrinkage, and irregular shape of the cells increased as the concentration of silver nanoparticles increased, suggesting that the cytotoxicity of silver nanoparticles to mitochondrial activity increased. In this study, the cells spread well and displayed a normal shape in the coatings incorporating silver, indicating that these implanted doses of Ag⁺ in the coatings are nontoxic to the colony cells.

4. Conclusion

Ag was incorporated in MAO TiO₂ coatings on pure titanium by an ion implantation method. The ion implantation technique demonstrated the unique advantage of providing a superfine silver nanoparticle. With increases in the implanted doses, the Ag content in the coatings increased. The in vitro antimicrobial tests indicated that the

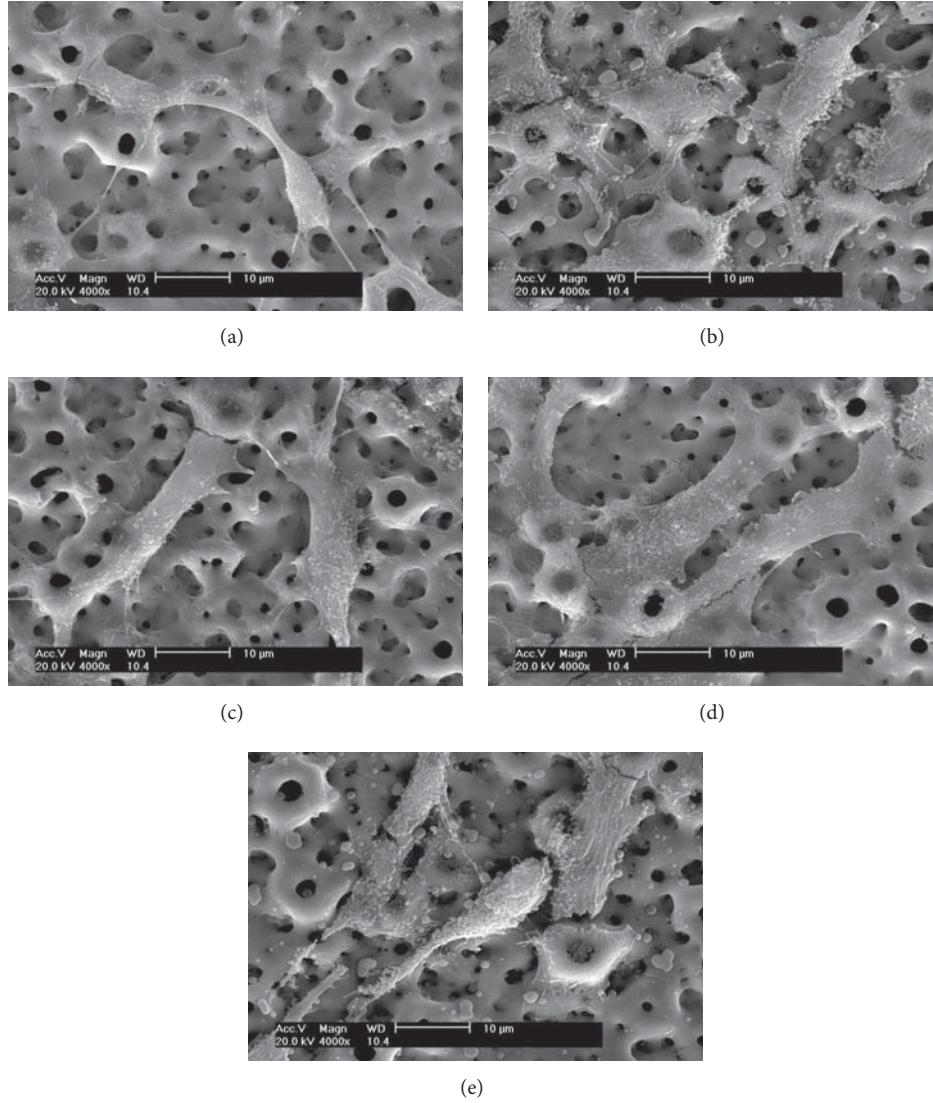


FIGURE 5: The surface morphology of the cells cultured on the surface of the Ag incorporated coatings by SEM: (a) the referred MAO-treated titanium, (b) Ti-MAO-Ag1.0, (c) Ti-MAO-Ag5.0, (d) Ti-MAO-Ag10.0, and (e) Ti-MAO-Ag20.0.

TABLE 1: Compositions on the Ag⁺ implanted surfaces from EDS analysis.

No.	Specimen	Dose (10^{17} ions/cm ²)	Element (wt. %)				
			Ti	O	Ca	P	Ag
1	Ti-MAO-Ag1.0	1.0	43.8	42.7	9.5	3.5	0.5
2	Ti-MAO-Ag5.0	5.0	55.5	34.5	6.8	2.5	0.8
3	Ti-MAO-Ag10.0	10	49.6	42.7	4.5	2.0	1.2
4	Ti-MAO-Ag20.0	20	51.0	34.3	9.5	3.9	1.3

Ag-containing coatings possessed good antibacterial ability, which may have resulted from the interaction between the nanocrystalline silver and the bacterial membrane. The superior biocompatibility and noncytotoxicity of the silver-containing porous structural coatings were confirmed by the

cell culture tests. The combination of antibacterial ability and biocompatibility as well as noncytotoxicity indicates that the ion implantation method could provide a promising strategy for the fabrication of a long-term antibacterial surface and thus an attractive biomaterial.

Acknowledgments

This research is supported by the Science and Technology Planning Project of Guangdong Province, China (no. 2010B010800024).

References

- [1] B. S. Necula, I. Apachitei, F. D. Tichelaar, L. E. Fratila-Apachitei, and J. Duszczek, "An electron microscopical study on the growth of TiO_2 -Ag antibacterial coatings on Ti6Al7Nb biomedical alloy," *Acta Biomaterialia*, vol. 7, no. 6, pp. 2751–2757, 2011.
- [2] Y. Han, S. H. Hong, and K. Xu, "Structure and in vitro bioactivity of titania-based films by micro-arc oxidation," *Surface and Coatings Technology*, vol. 168, no. 2–3, pp. 249–258, 2003.
- [3] P. Huang, K. W. Xu, and Y. Han, "Preparation and apatite layer formation of plasma electrolytic oxidation film on titanium for biomedical application," *Materials Letters*, vol. 59, no. 2–3, pp. 185–189, 2005.
- [4] P. Huang, F. Wang, K. Xu et al., "Mechanical properties of titania prepared by plasma electrolytic oxidation at different voltages," *Surface and Coatings Technology*, vol. 201, no. 9–11, pp. 5168–5171, 2007.
- [5] J. Sun, Y. Han, and K. Cui, "Microstructure and apatite-forming ability of the MAO-treated porous titanium," *Surface and Coatings Technology*, vol. 202, no. 17, pp. 4248–4256, 2008.
- [6] A. L. Yerokhin, X. Nie, A. Leyland, A. Matthews, and S. J. Dowey, "Plasma electrolysis for surface engineering," *Surface and Coatings Technology*, vol. 122, no. 2–3, pp. 73–93, 1999.
- [7] A. D. Pye, D. E. A. Lockhart, M. P. Dawson, C. A. Murray, and A. J. Smith, "A review of dental implants and infection," *Journal of Hospital Infection*, vol. 72, no. 2, pp. 104–110, 2009.
- [8] L. Zhao, P. K. Chu, Y. Zhang, and Z. Wu, "Antibacterial coatings on titanium implants," *Journal of Biomedical Materials Research B*, vol. 91, no. 1, pp. 470–480, 2009.
- [9] I. Banerjee, R. C. Pangule, and R. S. Kane, "Antifouling coatings: recent developments in the design of surfaces that prevent fouling by proteins, bacteria, and marine organisms," *Advanced Materials*, vol. 23, no. 6, pp. 690–718, 2011.
- [10] E. De Giglio, S. Cometa, M. A. Ricci et al., "Ciprofloxacin-modified electrosynthesized hydrogel coatings to prevent titanium-implant-associated infections," *Acta Biomaterialia*, vol. 7, no. 2, pp. 882–891, 2011.
- [11] M. Kazemzadeh-Narbat, J. Kindrachuk, K. Duan, H. Jenssen, R. E. W. Hancock, and R. Wang, "Antimicrobial peptides on calcium phosphate-coated titanium for the prevention of implant-associated infections," *Biomaterials*, vol. 31, no. 36, pp. 9519–9526, 2010.
- [12] P. A. Norowski and J. D. Bumgardner, "Biomaterial and antibiotic strategies for peri-implantitis," *Journal of Biomedical Materials Research B*, vol. 88, pp. 530–543, 2009.
- [13] B. Yang, L. Gan, Y. Qu, and C. Yue, "Anti-inflammatory properties of bioactive titanium metals," *Journal of Biomedical Materials Research A*, vol. 94, no. 3, pp. 700–705, 2010.
- [14] D. Isackson, L. D. McGill, and K. N. Bachus, "Percutaneous implants with porous titanium dermal barriers: an in vivo evaluation of infection risk," *Medical Engineering and Physics*, vol. 33, no. 4, pp. 418–426, 2011.
- [15] C. Cyteval and A. Bourdon, "Imaging orthopedic implant infections," *Diagnostic and Interventional Imaging*, vol. 93, no. 6, pp. 547–557, 2012.
- [16] N. J. Hickok and I. M. Shapiro, "Immobilized antibiotics to prevent orthopaedic implant infections," *Advanced Drug Delivery Reviews*, vol. 64, no. 12, pp. 1165–1176, 2012.
- [17] S. Jeyapalina, J. P. Beck, K. N. Bachus et al., "Efficacy of a porous-structured titanium subdermal barrier for preventing infection in percutaneous osseointegrated prostheses," *Journal of Orthopaedic Research*, vol. 30, no. 8, pp. 1304–1311, 2012.
- [18] M. Yoshinari, Y. Oda, T. Kato, and K. Okuda, "Influence of surface modifications to titanium on antibacterial activity in vitro," *Biomaterials*, vol. 22, no. 14, pp. 2043–2048, 2001.
- [19] L. Zhao, H. Wang, K. Huo et al., "Antibacterial nano-structured titania coating incorporated with silver nanoparticles," *Biomaterials*, vol. 32, no. 24, pp. 5706–5716, 2011.
- [20] A. Melaiye and W. J. Youngs, "Silver and its application as an antimicrobial agent," *Expert Opinion on Therapeutic Patents*, vol. 15, no. 2, pp. 125–130, 2005.
- [21] M. Rai, A. Yadav, and A. Gade, "Silver nanoparticles as a new generation of antimicrobials," *Biotechnology Advances*, vol. 27, no. 1, pp. 76–83, 2009.
- [22] M. Bosetti, A. Massè, E. Tobin, and M. Cannas, "Silver coated materials for external fixation devices: in vitro biocompatibility and genotoxicity," *Biomaterials*, vol. 23, no. 3, pp. 887–892, 2002.
- [23] A. Ewald, D. Hösel, S. Patel et al., "Silver-doped calcium phosphate cements with antimicrobial activity," *Acta Biomaterialia*, vol. 7, no. 11, pp. 4064–4070, 2011.
- [24] P. K. Chu, J. Y. Chen, L. P. Wang, and N. Huang, "Plasma-surface modification of biomaterials," *Materials Science and Engineering R*, vol. 36, no. 5–6, pp. 143–206, 2002.
- [25] X. Liu, R. W. Y. Poon, S. C. H. Kwok, P. K. Chu, and C. Ding, "Plasma surface modification of titanium for hard tissue replacements," *Surface and Coatings Technology*, vol. 186, no. 1–2, pp. 227–233, 2004.
- [26] E. Matykina, M. Montuori, J. Gough et al., "Spark anodising of titanium for biomedical applications," *Transactions of the Institute of Metal Finishing*, vol. 84, no. 3, pp. 125–133, 2006.
- [27] F. C. Walsh, C. T. J. Low, R. J. K. Wood et al., "Plasma electrolytic oxidation (PEO) for production of anodised coatings on lightweight metal (Al, Mg, Ti) alloys," *Transactions of the Institute of Metal Finishing*, vol. 87, no. 3, pp. 122–135, 2009.
- [28] A. G. Rakoch and I. V. Bardin, "Microarc oxidation of light alloys," *Metallurgist*, vol. 54, no. 5–6, pp. 378–383, 2010.
- [29] W. G. Graham and K. R. Stalder, "Plasmas in liquids and some of their applications in nanoscience," *Journal of Physics D*, vol. 44, no. 17, Article ID 174037, 2011.
- [30] T. Shirai, T. Shimizu, K. Ohtani, Y. Zen, M. Takaya, and H. Tsuchiya, "Antibacterial iodine-supported titanium implants," *Acta Biomaterialia*, vol. 7, no. 4, pp. 1928–1933, 2011.
- [31] O. Akhavan, "Lasting antibacterial activities of Ag-TiO₂/Ag-a-TiO₂ nanocomposite thin film photocatalysts under solar light irradiation," *Journal of Colloid and Interface Science*, vol. 336, no. 1, pp. 117–124, 2009.
- [32] I. Sondi and B. Salopek-Sondi, "Silver nanoparticles as antimicrobial agent: a case study on *E. coli* as a model for Gram-negative bacteria," *Journal of Colloid and Interface Science*, vol. 275, no. 1, pp. 177–182, 2004.
- [33] Q. L. Feng, J. Wu, G. Q. Chen et al., "A mechanistic study of the antibacterial effect of silver ions on *Escherichia coli* and *Staphylococcus aureus*," *Journal of Biomedical Materials Research*, vol. 52, no. 4, pp. 662–668, 2000.
- [34] P. K. Stoimenov, R. L. Klinger, G. L. Marchin, and K. J. Klabunde, "Metal oxide nanoparticles as bactericidal agents," *Langmuir*, vol. 18, no. 17, pp. 6679–6686, 2002.

- [35] W. K. Jung, H. C. Koo, K. W. Kim, S. Shin, S. H. Kim, and Y. H. Park, "Antibacterial activity and mechanism of action of the silver ion in *Staphylococcus aureus* and *Escherichia coli*," *Applied and Environmental Microbiology*, vol. 74, no. 7, pp. 2171–2178, 2008.
- [36] S. H. Kim, H. S. Lee, D. S. Ryu, S. J. Choi, and D. S. Lee, "Antibacterial activity of silver-nanoparticles against *Staphylococcus aureus* and *Escherichia coli*," *Korean Journal of Microbiology and Biotechnology*, vol. 39, no. 1, pp. 77–85, 2011.
- [37] Q. L. Feng, J. Wu, G. Q. Chen et al., "A mechanistic study of the antibacterial effect of silver ions on *Escherichia coli* and *Staphylococcus aureus*," *Journal of Biomedical Materials Research*, vol. 52, no. 4, pp. 662–668, 2000.
- [38] D. Q. Wei, Y. Zhou, and C. H. Yang, "Characteristic, cell response and apatite-induction ability of microarc oxidized TiO₂-based coating containing P on Ti6Al4V before and after chemical-treatment and dehydration," *Ceramics International*, vol. 35, no. 7, pp. 2545–2554, 2009.
- [39] Y. W. Lim, S. Y. Kwon, D. H. Sun, H. E. Kim, and Y. S. Kim, "Enhanced cell integration to titanium alloy by surface treatment with microarc oxidation: a pilot study," *Clinical Orthopaedics and Related Research*, vol. 467, no. 9, pp. 2251–2258, 2009.
- [40] L. Braydich-Stolle, S. Hussain, J. J. Schlager, and M. C. Hofmann, "In vitro cytotoxicity of nanoparticles in mammalian germline stem cells," *Toxicological Sciences*, vol. 88, no. 2, pp. 412–419, 2005.
- [41] S. M. Hussain, K. L. Hess, J. M. Gearhart, K. T. Geiss, and J. J. Schlager, "In vitro toxicity of nanoparticles in BRL 3A rat liver cells," *Toxicology in Vitro*, vol. 19, no. 7, pp. 975–983, 2005.

Research Article

Thermodynamic Property Study of Nanostructured Mg-H, Mg-Ni-H, and Mg-Cu-H Systems by High Pressure DSC Method

Huaiyu Shao,¹ Gongbiao Xin,² Xingguo Li,² and Etsuo Akiba¹

¹ International Institute for Carbon-Neutral Energy Research (WPI- I2CNER), Kyushu University, Fukuoka 819-0395, Japan

² Beijing National Laboratory for Molecular Sciences (BNLMS), and The State Key Laboratory of Rare Earth Materials Chemistry and Applications, College of Chemistry and Molecular Engineering, Peking University, Beijing 100871, China

Correspondence should be addressed to Huaiyu Shao; h.shao@i2cner.kyushu-u.ac.jp and Xingguo Li; xgli@pku.edu.cn

Received 13 December 2012; Accepted 17 January 2013

Academic Editor: Jianxin Zou

Copyright © 2013 Huaiyu Shao et al. This is an open access article distributed under the Creative Commons Attribution License, which permits unrestricted use, distribution, and reproduction in any medium, provided the original work is properly cited.

Mg, Ni, and Cu nanoparticles were synthesized by hydrogen plasma metal reaction method. Preparation of Mg_2Ni and Mg_2Cu alloys from these Mg, Ni, and Cu nanoparticles has been successfully achieved in convenient conditions. High pressure differential scanning calorimetry (DSC) technique in hydrogen atmosphere was applied to study the synthesis and thermodynamic properties of the hydrogen absorption/desorption processes of nanostructured Mg-H, Mg-Ni-H, and Mg-Cu-H systems. Van't Hoff equation of Mg-Ni-H system as well as formation enthalpy and entropy of Mg_2NiH_4 was obtained by high pressure DSC method. The results agree with the ones by pressure-composition isotherm (PCT) methods in our previous work and the ones in literature.

1. Introduction

Mg and Mg-based alloys are widely studied as hydrogen storage materials for the advantages such as low price, light weight, high hydrogen capacity, and high abundance of Mg in the earth's crust [1–4]. The hydrides of Mg and the common Mg-based alloys show considerable hydrogen storage content—7.6 mass% for MgH_2 and 3.6, 4.5, and 5.4 mass% for Mg_2NiH_4 , Mg_2CoH_5 , and Mg_2FeH_6 , respectively. Recently some new hydrogen storage materials have been explored [4, 5], but Mg-based materials are still ones of the most promising hydrogen storage candidates to many researchers, especially for heat storage or stationary energy storage [3, 6], in which cases, working temperature can be above 500 K.

One serious barrier of Mg-based alloys for hydrogen storage study is synthesis of these alloys by conventional melting method because of the large difference in melting point and vaporization pressure between Mg and Ni, Co, Fe, and so forth. Ball milling/mechanical alloying method has been developed to synthesize Mg-based alloys and it is considered as one effective way to prepare nonequilibrium

alloy samples with plenty of defects and samples with grain size in nanometer scale [7]. Recently it has almost become the main preparation method by many groups to study Mg-based alloys [8–20]. However, this method faces the disadvantage of possible pollution by steel balls or air during the milling process. Another difficulty in the study of Mg-based materials is poor kinetics of these materials. For example, Mg_2Ni in micrometer scale produced by conventional melting method needs absorption/desorption temperature higher than 500 K even after several hydrogen absorption and desorption cycles under hydrogen pressure atmosphere. Common Mg metal samples in micrometer scale need much stricter conditions to absorb and desorb hydrogen. Our group and some other researchers successfully prepared nanostructured Mg-based alloy and hydride samples in convenient conditions from metal nanoparticles which were synthesized by plasma metal reaction [21–26]. These nanostructured samples show excellent hydrogen storage kinetics and properties. They can absorb and desorb hydrogen in convenient conditions without any activation process [23, 27, 28]. This work is to demonstrate that we can study the preparation process, thermodynamic properties, and reaction mechanism of

these nanostructured Mg-based materials by high pressure differential scanning calorimetry (DSC) technique under hydrogen atmosphere.

2. Experimental Details

The Mg, Ni, and Cu nanoparticles were synthesized from bulk metals by hydrogen plasma metal reaction method. Bulk Mg, Ni, and Cu metals (purity > 99.7%) were melted and vaporized by hydrogen-plasma-metal reaction in the chamber and the gaseous metals were taken to the collecting room by the circulating gas and were deposited on the filter wall, where we obtained the Mg, Ni, and Cu metal nanoparticles. To prepare Mg-Ni and Mg-Cu system alloys and hydrides, Mg and Ni (Cu) nanoparticles were weighted at a 2:1 molar ratio and mixed in acetone by an ultrasonic homogenizer. Then the mixture was dried and pressed into small pieces, from which, Mg-Ni (Mg-Cu) hydrides were synthesized in 4 MPa hydrogen atmosphere at 623 K (673 K) for 2 h (9 h) and alloys were obtained after the evacuation of the hydrides at the same temperature.

The composition and structure analysis of the samples were carried out by X-ray diffraction at an automatic Rigaku X-ray diffractometer with monochromatic Cu K α radiation at a scanning rate of 4°/min.

The synthesis and thermodynamic properties of Mg-H, Mg-Ni-H, and Mg-Cu-H systems were studied from DSC measurements using a NETZSCH DSC 204 HP apparatus starting from metal nanoparticles. Mg, 2Mg+Ni and 2Mg+Cu nanoparticle mixture samples with about 10 mg in weight were put into the chamber of the DSC apparatus. After closure of the system, evacuation and supply of 0.5 MPa hydrogen cycles were conducted to fresh the system. For the synthesis of Mg-Ni-H and Mg-Cu-H system, a flowing and constant hydrogen atmosphere of 4 MPa pressure was provided to the DSC chamber system. A special device is equipped in this DSC machine to keep the flowing atmosphere constant. The temperature was increased from room temperature to 823 K at a heating rate of 20 K/min. The heating and cooling processes were repeated two more cycles after the first synthesis cycle. After the production of Mg₂NiH₄, the sample was taken through several heating and cooling cycles between 453 K and 823 K at 5, 10, and 20 K/min in various flowing and constant hydrogen pressure value (1 MPa, 2 MPa, and 4 MPa).

3. Results and Discussion

Figures 1 and 2 show the XRD curves of the metal nanoparticle samples by hydrogen plasma metal reaction method and Mg-Ni-H, Mg-Cu-H system samples prepared from these metal nanoparticles. Figure 1(a) shows the metal nanoparticle sample prepared from bulk Mg contains pure Mg phase. Mg nanoparticle sample shows hexagonal structure and the space group is P6₃/mmc. The size is in the range of a few hundred nm. There is a small reflection peak at 42.9°, which is due to the small amount of MgO impurity (less than 1 mass%). All of the other peaks are indexed to Mg phase. This thin layer MgO actually is very helpful to prevent the Mg particles

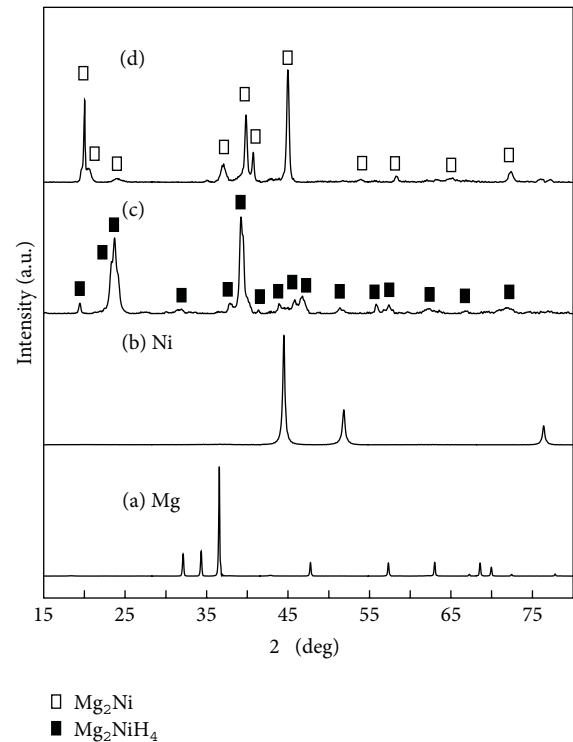


FIGURE 1: XRD patterns of (a) Mg nanoparticles, (b) Ni nanoparticles, (c) Mg₂NiH₄ sample prepared from Mg and Ni nanoparticles at 623 K in 4 MPa hydrogen for 2 hours, and (d) Mg₂Ni sample prepared after evacuation of Mg₂NiH₄.

from further oxidation. The reflection peaks in Figure 1(b) are all ascribed to Ni nanoparticles. Ni sample shows face-centered cubic structure of Fm3m space group. The broadening of Ni peaks indicates the nanostructure of Ni samples. The particle size is about 30–50 nm. Figure 1(c) presents the Mg₂NiH₄ sample prepared from 2Mg+Ni nanoparticle mixture by sintering in 4 MPa hydrogen at 623 K for 2 h. The XRD curve is well indexed to monoclinic Mg₂NiH₄ low-temperature phase (space group: C2/m). After evacuation of the Mg₂NiH₄ sample, Mg₂Ni alloy (hexagonal structure, space group: P6₂22) was obtained (Figure 1(d)). Hydrogen and nanostructure of the metal samples play important roles in the preparation of Mg₂NiH₄ and Mg₂Ni samples in convenient conditions.

Figure 2(b) indicates XRD curve of the obtained Cu nanoparticles. Only Cu phase is observed, which is face-centered cubic structure with the space group of Fm3m. The Cu peaks are also broad because of the nanostructure of the Cu phase. From 2Mg+Cu nanoparticle mixture, firstly Mg-Cu-H hydride sample was obtained by sintering the mixture sample in 4 MPa hydrogen atmosphere at 673 K for 9 h and the XRD curve of the obtained hydrides sample is shown in Figure 2(c). The sample mainly consists of MgH₂ (tetragonal structure, space group: P4₂/mmn) and MgCu₂ (face-centered cubic structure, space group: Fd3m) phases. For Mg-Cu-H system, there is no ternary hydride found in literature up to now. After the evacuation, Mg₂Cu main phase sample

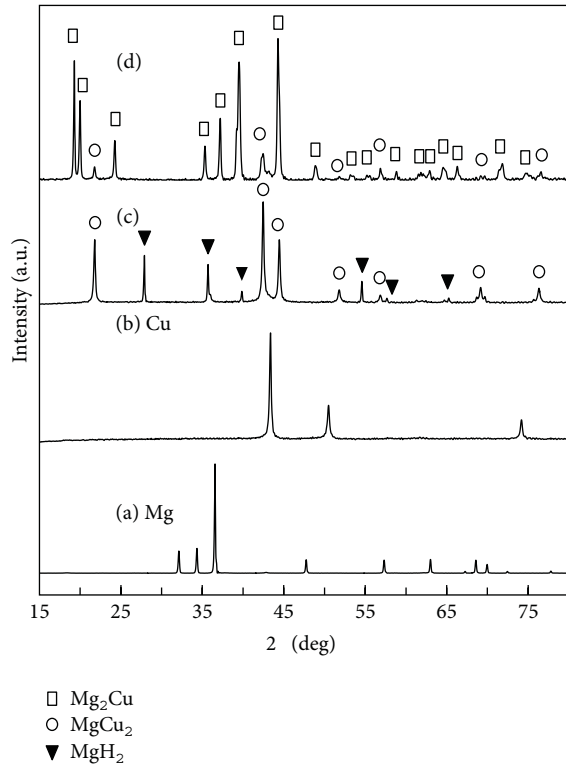


FIGURE 2: XRD patterns of (a) Mg nanoparticles, (b) Cu nanoparticles, (c) Mg-Cu-H hydride sample prepared from Mg and Cu nanoparticles at 673 K in 4 MPa hydrogen for 9 hours, and (d) Mg_2Cu sample prepared after evacuation of Mg-Cu-H hydride system.

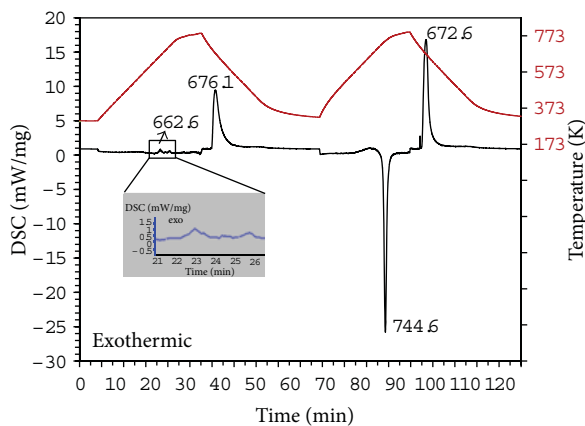


FIGURE 3: DSC curve of Mg-H system started from Mg nanoparticle sample in 4 MPa hydrogen pressure.

(orthorhombic, space group: $Fddd$) was obtained. A small amount of MgCu_2 impurity is detected.

Figure 3 shows the DSC curve of the Mg nanoparticles in an initial hydrogen pressure of 4 MPa, at a scan rate of 20 K/min. The upper dash line indicates the temperature trend and the solid line shows the DSC curve. The first peak is a small exothermic peak at 662.6 K, which is due to the

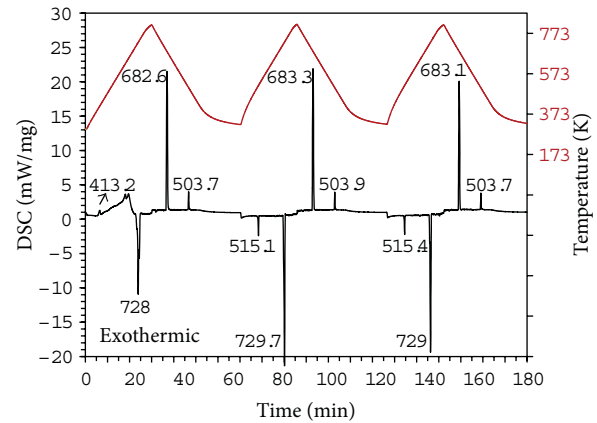
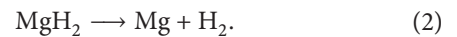
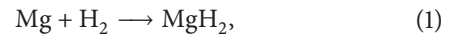


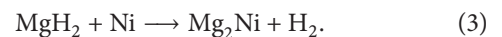
FIGURE 4: DSC curve of Mg-Ni-H system started from 2Mg+Ni nanoparticle mixture in 4 MPa hydrogen pressure.

hydrogen absorption of small amount of Mg nanoparticles. Most of the Mg begins to react with hydrogen to form MgH_2 in the first cooling cycle and shows an exothermic peak at 676.1 K. Firstly, only partial Mg sample reacts with hydrogen to form the hydride because at the beginning of the hydrogen absorption, it is difficult for hydrogen to penetrate the MgO layer on the surface of Mg nanoparticles and then enter the interior of Mg particles in very short time with heating rate of 20 K/min due to kinetic limitation. After the Mg particle surface are cracked by the entry of hydrogen, much more fresh surface occurs and makes it easier for hydrogen to enter the Mg particle interior and react with the left Mg to form MgH_2 . The reaction equations are expressed as follows:



In the second heating cycle, the hydrogenated MgH_2 desorbs hydrogen to form Mg phase and shows an endothermic peak with a peak temperature of 744.6 K (2). The formed Mg absorbs hydrogen again during the second cooling process and shows a peak temperature of 672.6 K (1).

Figure 4 presents the DSC result of starting sample-2Mg+Ni nanoparticle mixture in 4 MPa hydrogen, at a scan rate of 20 K/min. The first exothermic peak at 413.2 K is attributed to the hydrogen absorption of part of the Mg nanoparticles (1) with Ni as catalyst. The hydrogen absorption peak of Mg nanoparticles is about 250 K lowered (compared to Figure 3) when there are Ni nanoparticles as catalyst, which indicates the excellent catalytic effect of Ni nanoparticles to the hydrogen absorption of Mg phase. At about 430~450 K, there are several exothermic peaks, which are also due to hydrogen absorption of the rest Mg nanoparticles. The formed MgH_2 reacts with Ni to form Mg_2Ni and shows an endothermic peak in the first heating period at 728.0 K. The reaction is expressed as follows:



The Mg_2Ni phase absorbs hydrogen and shows an exothermic peak at 682.6 K in the first cooling cycle, which is ascribed to

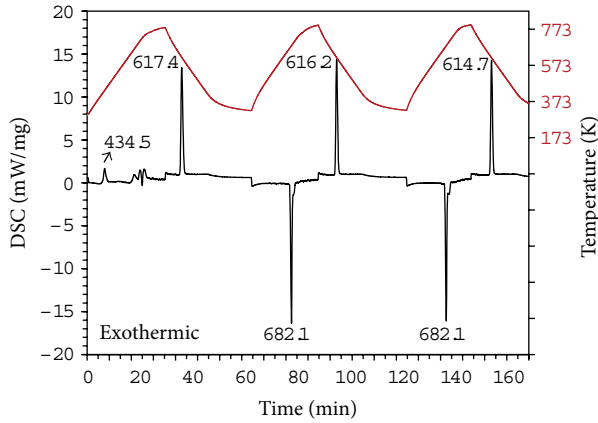
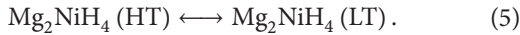


FIGURE 5: DSC curve of Mg-Cu-H system started from 2Mg+Cu nanoparticle mixture in 4 MPa hydrogen pressure.

(4). The exothermic peaks at 683.3 K in the second cooling cycle and 683.1 K in the third cycle have the same attribution:



A small exothermic peak at 503.7 K in the first cooling cycle is due to the transformation of high temperature (HT) Mg_2NiH_4 phase to low temperature one (LT) (5). The exothermic peak at 503.9 K in the second cooling cycle and the one at 503.7 K in the third cooling cycle are due to the same transformation reaction. The exothermic peak at 515.1 K in the second heating cycle and the one at 515.4 K at the third heating cycle are due to the transformation of low temperature Mg_2NiH_4 phase to high temperature one as follows:



The high and sharp peak at 729.7 K at the second heating cycle and the one at 729.0 K at the third cycle are due to desorption of Mg_2NiH_4 phase to form Mg_2Ni and hydrogen as follows:

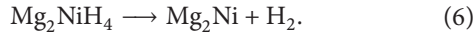


Figure 5 indicates the DSC curve of 2Mg+Cu nanoparticle mixture in 4 MPa hydrogen atmosphere. The heating and cooling rate is 20 K/min. The first exothermic peak occurs at 434.5 K, which is corresponding to the hydrogen absorption of Mg nanoparticles with Cu nanoparticles as the catalyst. This is similar to Mg-Ni-H system in Figure 4. With Cu catalyst, the hydrogenation peak temperature is lowered about 230 K. After the first exothermic peak, there are several exothermic and endothermic peaks in the temperature range of 660 K to 740 K in the first heating period. The attribution of these peaks remains unclear currently. After these peaks, the next peak at 617.4 K in the first cooling cycle could be easily defined as hydrogen absorption peak of Mg_2Cu phase according to DSC results of Mg-H system in Figure 3 and pressure-composition isotherm (PCT) results reported by us before [28]. The reactions of (1), (7), and (8) are thought to

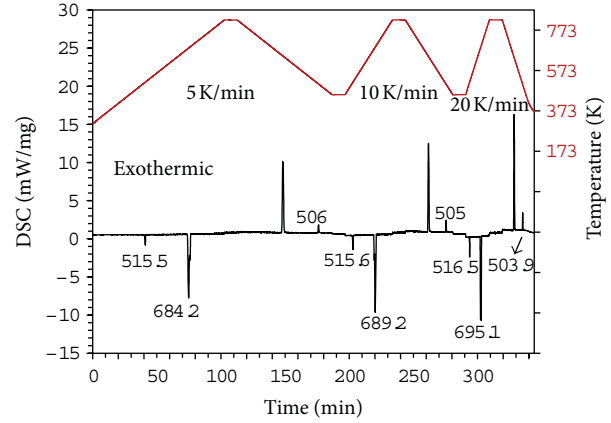
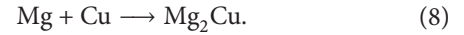
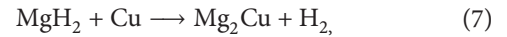


FIGURE 6: DSC curve of Mg-Ni-H system in 2 MPa hydrogen, at different scan rates started from Mg_2NiH_4 sample.

contribute to these peaks between 600 K and 740 K in the first heating process as follows:



The sharp exothermic peaks at 617.4 K, 616.2 K, and 614.7 K in the cooling period are due to the hydrogen absorption of Mg_2Cu expressed as (9), which could be easily confirmed by the XRD results after the DSC measurement. The large sharp endothermic peaks at 682.1 K in the second and third cycles are attributed to desorption of MgH_2 and MgCu_2 mixture to form Mg_2Cu and hydrogen (10). The same reaction mechanism during cycling of Mg-Cu-H system was reported by other groups [1, 29]:

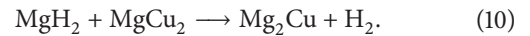
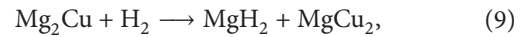


Figure 6 presents the DSC curve started from low temperature Mg_2NiH_4 phase in 2 MPa hydrogen, which is obtained from 2Mg+Ni nanoparticle mixture by DSC methods in 4 MPa hydrogen for one heating and cooling cycle. The upper dash line shows the temperature program. The middle solid line indicates the pressure change with time. During each heating and cooling cycle with different scan rates (5, 10, and 20 K/min), there are two large peaks and two small ones. These peaks have the same attribution with the ones in the second and third cycles of the DSC curve in Figure 4. They are also ascribed to (5), (6), (4), and (5) in the appearance order. From the figure, we may see that the desorption reaction of Mg_2NiH_4 to form Mg_2Ni (6) in 2 MPa hydrogen shows the peak temperatures of 684.2 K at 5 K/min, 689.2 K at 10 K/min, and 695.1 K at 20 K/min. From the pressure recording data, we obtain the real-time pressure values, which are 2.106 MPa for 684.2 K at 5 K/min, 2.106 MPa for 689.2 K at 10 K/min, and 2.107 MPa for 695.1 K at 20 K/min. These pressure, temperature and scan rate data in 2 MPa hydrogen are described in Table 1 and the values in 4 MPa and 1 MPa are

TABLE 1: Desorption temperature and pressure values from DSC measurements of Mg-Ni-H system.

Scan rate (K/min)	Desorption temperature (K)	Desorption pressure (0.1 MPa)
5	720.6	41.05
	684.2	21.06
	645.4	10.99
10	725.8	41.01
	689.2	21.06
	652.3	11.05
20	731.0	41.07
	695.1	21.07
	659.2	11.05

also included. These peaks are approximately corresponding to middle point of the desorption process. Usually we take the hydrogen equilibrium pressure of the middle point of the desorption curve during PCT measurement, and the real-time temperature of the middle point to make van't Hoff plot to obtain desorption enthalpy and entropy according to the van't Hoff equation:

$$\ln\left(\frac{P}{P^0}\right) = \frac{\Delta H}{RT} - \frac{\Delta S}{R}. \quad (11)$$

Using the data shown in Table 1, we could obtain the van't Hoff equations at different scan rates, which are given in Table 2. The van't Hoff equations vary with the scan rates because the peak temperatures for hydrogen desorption reaction from DSC technique differ at different scan rates. The higher the scan rate, the higher the temperature difference between peak temperature and real equilibrium temperature. If we want to obtain the van't Hoff equation at complete equilibrium state, we should take the DSC measurement at zero scan rate, which is impossible. However, in our case, the kinetics of the absorption and desorption reaction of nanostructured Mg-Ni-H system is superior. This means we can approach almost equilibrium state of the sorption reactions at low scan rates. After we measured the system at 5 K/min rate, we made the plot. We obtain a van't Hoff equation of $\ln(P/0.1 \text{ MPa}) = -8123/T + 14.961$ and the formation enthalpy and entropy values of -67.5 kJ/mol H_2 and $-124.4 \text{ J/(K}\cdot\text{mol H}_2)$. These results agree well with the ones from the van't Hoff equation ($\ln(P/0.1 \text{ MPa}) = -7978/T + 15.06$) and formation enthalpy and entropy values (-66.3 kJ/mol H_2 and $-125.3 \text{ J/(K}\cdot\text{mol H}_2)$, resp.) obtained by PCT technique in our previous work [23]. PCT technique is a traditional way used to make van't Hoff plot by obtaining the equilibrium pressure values of samples at various temperatures and obtain formation enthalpy and entropy values, but one whole PCT including hydrogen absorption and desorption process usually is quite time-consuming. It usually takes several days or much more depending on the hydrogen storage kinetics of the samples, measurement parameters, and equilibrium conditions. Also it has not been much noticed that the obtained equilibrium pressure values vary much with different equilibrium conditions during PCT

measurements, which could contribute to some difference in the calculated van't Hoff equation and formation enthalpy and entropy results using these plateau pressure data. By DSC technique, we could make a whole van't Hoff plot in a much more time-saving way. By comparing the results from DSC method and former PCT technique, it shows DSC method is an excellent way to obtain van't Hoff equations as well as formation enthalpy and entropy values of nanostructured hydrogen storage systems, which are with good kinetics. After we reported our method [30], Rongeat et al. reported their results about thermodynamic properties of hydrides determined by high pressure DSC method in a much different way [31]. We take the middle point of the DSC reaction peak and assume that the thermodynamics values obtained by our method are not equilibrium state while with kinetics factor, so we can compare with other people's results from desorption PCT measurements. Rongeat et al. tried to give a range of thermodynamics values of the equilibrium state between absorption measurements and desorption ones. Table 3 shows the temperature values of transformation reaction between high temperature Mg_2NiH_4 phase and low temperature one, in different hydrogen pressure values and at different scan rates. From this table, we can see that the transformation temperature from LT phase to HT phase and the one from HT phase to LT phase do not change much with the different hydrogen pressure.

4. Conclusions

The main conclusions of this work are as follows:

- (1) Nanostructured Mg-Ni-H, Mg-Cu-H hydride systems and Mg_2Ni , Mg_2Cu alloys can be obtained from Mg, Ni, and Cu nanoparticles by high hydrogen pressure DSC method.
- (2) The preparation process and hydrogen absorption and desorption properties of nanostructured Mg-H, Mg-Ni-H, and Mg-Cu-H systems were studied by DSC method. With Ni or Cu as catalyst, Mg nanoparticles absorb hydrogen at temperatures about 230–250 K lowered. Nanostructured Mg-H, Mg-Ni-H, and Mg-Cu-H systems show excellent hydrogen storage properties.
- (3) From the temperature and hydrogen pressure values obtained in DSC measurements of nanostructured Mg-Ni-H system, van't Hoff equation was obtained as $\ln(P/0.1 \text{ MPa}) = -8123/T + 14.961$ at 5 K/min scan rate. The formation enthalpy and entropy are -67.5 kJ/mol H_2 and $-124.4 \text{ J/(K}\cdot\text{mol H}_2)$. These results agree with those by PCT method.

Acknowledgments

The authors acknowledge support from the International Institute for Carbon-Neutral Energy Research (WPI-I2CNER), established by the World Premier International Research Center Initiative (WPI), MEXT, Japan. This work was also supported in part by JSPS KAKENHI (23860034)

TABLE 2: Van't Hoff equations of Mg_2NiH_4 at different DSC scan rates.

Scan rate (K/min)	Van't Hoff equation	Formation enthalpy ($-\text{kJ/mol H}_2$)	Formation entropy $-\text{J}/(\text{K} \cdot \text{mol H}_2)$
5	$\ln(P/0.1 \text{ MPa}) = -8123/T + 14.961$	67.5	124.4
10	$\ln(P/0.1 \text{ MPa}) = -8431/T + 15.313$	70.1	127.3
20	$\ln(P/0.1 \text{ MPa}) = -8793/T + 15.728$	73.1	130.8

TABLE 3: Transformation temperatures between high temperature Mg_2NiH_4 phase and low temperature one in different hydrogen pressure values and scan rate conditions.

LT phase to HT phase			HT phase to LT phase		
Pressure (MPa)	Scan rate (K/min)	Temperature (K)	Pressure (MPa)	Scan rate (K/min)	Temperature (K)
4	20	516.6	4	20	504.7
	10	515.3		10	506.2
	5	515.0		5	507.2
2	20	516.5	2	20	503.9
	10	515.6		10	505.0
	5	515.5		5	506.0
1	20	516.5	1	20	504.1
	10	515.7		10	504.8
	5	515.6		5	505.4

in Japan and MOST of China (no. 2010CB631301 and 2011AA03A408).

References

- [1] J. J. Reilly and R. H. Wiswall, "The reaction of hydrogen with alloys of magnesium and copper," *Inorganic Chemistry*, vol. 6, no. 12, pp. 2220–2223, 1967.
- [2] J. J. Reilly and R. H. Wiswall, "The reaction of hydrogen with alloys of magnesium and nickel and the formation of Mg_2NiH_4 ," *Inorganic Chemistry*, vol. 7, no. 11, pp. 2254–2256, 1968.
- [3] H. Shao, G. Xin, J. Zheng, X. Li, and E. Akiba, "Nanotechnology in Mg-based materials for hydrogen storage," *Nano Energy*, vol. 1, pp. 590–601, 2012.
- [4] B. Sakintuna, F. Lamari-Darkrim, and M. Hirscher, "Metal hydride materials for solid hydrogen storage: a review," *International Journal of Hydrogen Energy*, vol. 32, no. 9, pp. 1121–1140, 2007.
- [5] J. Yang, A. Sudik, C. Wolverton, and D. J. Siegel, "High capacity hydrogen storage materials: attributes for automotive applications and techniques for materials discovery," *Chemical Society Reviews*, vol. 39, no. 2, pp. 656–675, 2010.
- [6] B. Bogdanović, T. H. Hartwig, and B. Spliethoff, "The development, testing and optimization of energy storage materials based on the MgH_2/Mg system," *International Journal of Hydrogen Energy*, vol. 18, no. 7, pp. 575–589, 1993.
- [7] F. H. Froes, C. Suryanarayana, K. Russell, and C. G. Li, "Synthesis of intermetallics by mechanical alloying," *Materials Science and Engineering A*, vol. 192–193, no. 2, pp. 612–623, 1995.
- [8] Y. Q. Lei, Y. M. Wu, Q. M. Yang, J. Wu, and Q. D. Wang, "Electrochemical-behavior of some mechanically alloyed Mg-Ni-based amorphous hydrogen storage alloys," *Zeitschrift Fur Physikalische Chemie*, vol. 183, pp. 379–384, 1994.
- [9] M. Y. Song, "Effects of mechanical alloying on the hydrogen storage characteristics of Mg-Xwt-Percent Ni (X=0, 5, 10, 25 and 55) mixtures," *International Journal of Hydrogen Energy*, vol. 20, no. 3, pp. 221–227, 1995.
- [10] G. Liang, S. Boily, J. Huot, A. Van Neste, and R. Schulz, "Hydrogen absorption properties of a mechanically milled Mg-50 wt%LaNi₅ composite," *Journal of Alloys and Compounds*, vol. 268, no. 1–2, pp. 302–307, 1998.
- [11] S. Orimo and H. Fujii, "Hydriding properties of the Mg_2Ni -H system synthesized by reactive mechanical grinding," *Journal of Alloys and Compounds*, vol. 232, no. 1–2, pp. L16–L19, 1996.
- [12] E. Akiba, "Hydrogen-absorbing alloys," *Current Opinion in Solid State and Materials Science*, vol. 4, no. 3, pp. 267–272, 1999.
- [13] H. Imamura, I. Kitazawa, Y. Tanabe, and Y. Sakata, "Hydrogen storage in carbon/Mg nanocomposites synthesized by ball milling," *International Journal of Hydrogen Energy*, vol. 32, no. 13, pp. 2408–2411, 2007.
- [14] K. Asano, H. Enoki, and E. Akiba, "Effect of Li addition on synthesis of Mg-Ti BCC Alloys by means of ball milling," *Materials Transactions*, vol. 48, no. 2, pp. 121–126, 2007.
- [15] H. Shao, K. Asano, H. Enoki, and E. Akiba, "Correlation study between hydrogen absorption property and lattice structure of Mg-based BCC alloys," *International Journal of Hydrogen Energy*, vol. 34, no. 5, pp. 2312–2318, 2009.
- [16] H. Shao, K. Asano, H. Enoki, and E. Akiba, "Fabrication, hydrogen storage properties and mechanistic study of nanostructured $\text{Mg}_{50}\text{Co}_{50}$ body-centered cubic alloy," *Scripta Materialia*, vol. 60, no. 9, pp. 818–821, 2009.
- [17] H. Shao, K. Asano, H. Enoki, and E. Akiba, "Preparation and hydrogen storage properties of nanostructured Mg-Ni BCC alloys," *Journal of Alloys and Compounds*, vol. 477, no. 1–2, pp. 301–306, 2009.
- [18] H. Shao, K. Asano, H. Enoki, and E. Akiba, "Fabrication and hydrogen storage property study of nanostructured Mg-Ni-B ternary alloys," *Journal of Alloys and Compounds*, vol. 479, no. 1–2, pp. 409–413, 2009.

- [19] K. Yamamoto, S. Tanioka, Y. Tsushio et al., "Influence of elemental diffusion on low temperature formation of MgH_2 in $\text{TiMn}_{1.3}\text{Ti}_{0.2}\text{Mg}$ (T equals 3d-transition elements)," *Journal of Alloys and Compounds*, vol. 243, no. 1-2, pp. 144–150, 1996.
- [20] J. Lu, J. C. Young, Z. F. Zhigang, Y. S. Hong, and E. Rönnebro, "Hydrogen storage properties of nanosized MgH_2 -0.1 TiH_2 prepared by ultrahigh-energy-high-pressure milling," *Journal of the American Chemical Society*, vol. 131, no. 43, pp. 15843–15852, 2009.
- [21] H. Shao, T. Liu, X. Li, and L. Zhang, "Preparation of Mg_2Ni intermetallic compound from nanoparticles," *Scripta Materialia*, vol. 49, no. 6, pp. 595–599, 2003.
- [22] H. Shao, T. Liu, and X. Li, "Preparation of the Mg_2Ni compound from ultrafine particles and its hydrogen storage properties," *Nanotechnology*, vol. 14, no. 3, pp. L1–L3, 2003.
- [23] H. Shao, H. Xu, Y. Wang, and X. Li, "Preparation and hydrogen storage properties of Mg_2Ni intermetallic nanoparticles," *Nanotechnology*, vol. 15, no. 3, pp. 269–274, 2004.
- [24] H. Shao, T. Liu, Y. Wang, H. Xu, and X. Li, "Preparation of Mg-based hydrogen storage materials from metal nanoparticles," *Journal of Alloys and Compounds*, vol. 465, no. 1-2, pp. 527–533, 2008.
- [25] J. Zou, X. Zeng, Y. Ying et al., "Study on the hydrogen storage properties of core-shell structured Mg-RE (RE = Nd, Gd, Er) nano-composites synthesized through arc plasma method," *International Journal of Hydrogen Energy*, vol. 38, pp. 2337–2346, 2013.
- [26] J. X. Zou, X. Q. Zeng, Y. J. Ying, P. Stephane, and W. J. Ding, "Preparation and hydrogen sorption properties of a nano-structured Mg based Mg-La-O composite," *International Journal of Hydrogen Energy*, vol. 37, pp. 13067–13073, 2012.
- [27] H. Shao, H. Xu, Y. Wang, and X. Li, "Synthesis and hydrogen storage behavior of Mg-Co-H system at nanometer scale," *Journal of Solid State Chemistry*, vol. 177, no. 10, pp. 3626–3632, 2004.
- [28] H. Shao, Y. Wang, H. Xu, and X. Li, "Preparation and hydrogen storage properties of nanostructured Mg_2Cu alloy," *Journal of Solid State Chemistry*, vol. 178, no. 7, pp. 2211–2217, 2005.
- [29] F. K. Hsu, C. W. Hsu, J. K. Chang, C. K. Lin, S. L. Lee, and C. E. Jiang, "Structure and hydrogen storage properties of $\text{Mg}_2\text{Cu} 1-x\text{Ni}_x$ ($x=0-1$) alloys," *International Journal of Hydrogen Energy*, vol. 35, no. 24, pp. 13247–13254, 2010.
- [30] H. Shao, *Preparation and hydrogen storage properties of Mg-based nanostructures materials [Ph.D. thesis]*, Beijing Unvieristy, 2005.
- [31] C. Rongeat, I. Llamas-Jansa, S. Doppiu et al., "Determination of the heat of hydride formation/decomposition by High-Pressure Differential Scanning Calorimetry (HP-DSC)," *Journal of Physical Chemistry B*, vol. 111, no. 46, pp. 13301–13306, 2007.

Research Article

Low Temperature Synthesis of Hexagonal Shaped α -Al₂O₃ Using a Solvothermal Method

A-Young Kim,¹ Hyun Soo Kim,¹ No-Kuk Park,² Tae Jin Lee,² Won Gun Lee,³
Heun Duk Kim,³ Jun Woo Park,³ and Misook Kang¹

¹Department of Chemistry, College of Science, Yeungnam University, 214-1 Daedong, Gyeongsan, Gyeongbuk 712-749, Republic of Korea

²School of Chemical Engineering, Yeungnam University, 214-1 Daedong, Gyeongsan, Gyeongbuk 712-749, Republic of Korea

³TPS Inc., 193 Galsan-dong, Dalseo-gu, Daegu 704-900, Republic of Korea

Correspondence should be addressed to Misook Kang, mskang@ynu.ac.kr

Received 15 November 2012; Revised 6 December 2012; Accepted 12 December 2012

Academic Editor: Jianxin Zou

Copyright © 2012 A-Young Kim et al. This is an open access article distributed under the Creative Commons Attribution License, which permits unrestricted use, distribution, and reproduction in any medium, provided the original work is properly cited.

This study demonstrates the low temperature synthesis of α -Al₂O₃ by solvothermal method using gibbsite alumina precursor in 1, 4-butanediol solvent according to various pH conditions. In acidic solution, an orthorhombic boehmite (AlOOH) structure was obtained after solvothermal reaction. A significant result in this study was that the solvothermally synthesized alumina in pH = 9 at 300 °C for 36 h represented a rhombohedral α -Al₂O₃ structure hexagonal shaped with about 1.5~2.0 μ m of particle size. Otherwise, the α -Al₂O₃ structure was rather changed to the mixture of a boehmite and α -Al₂O₃ structures above pH = 11. In the case of α -Al₂O₃ synthesized at pH = 9, the specific surface area was 26.18 m²/g, and the particles that were stable in acidic solution resulted in 61.80 mV of zeta potential.

1. Introduction

The α -Al₂O₃ powder has considerable potential for a wide range of applications including high strength materials, sapphire crystal growth, electronics, semiconductors, and catalysts [1–4]. In particular, the current high demand for sapphire substrates for the LED market has greatly added to the crystal growth business on top of existing applications. The volume of sapphire wafer production is currently measured in hundreds of millions of units annually. Here α -Al₂O₃ crystals have attracted attention as a source of sapphire. Due to its versatility, increasing interest has focused on the synthesis of α -Al₂O₃. Conventional synthesis processes of α -Al₂O₃ involve vapor phase reaction, precipitation, sol-gel, hydrothermal, and combustion methods. Vapor phase reaction for preparation fine α -Al₂O₃ powder from a gas phase precursor demands high temperature above 1200 °C [5]. The precipitation method suffers from its complexity and time consuming as like long washing times and aging time [6]. The direct formation of α -Al₂O₃ via the hydrothermal method needs high temperature and pressure [7].

The combustion method has been used to yield α -Al₂O₃ powders, whereas the powder obtained from the process is usually hard aggregated but contains nano-sized primary particles [8]. Sol-gel a commonly from a precursor solution used technique, involves the formation of an amorphous gel; however, this method needs some thermal treatment steps at various temperatures [9, 10]. In general, α -Al₂O₃ derived from the decomposition of gelatinous boehmite, gibbsite, and related hydroxide alumina undergoes a number of transitional phases. Amorphous alumina dehydrates at 500 °C to form γ -alumina which then transforms to δ -alumina and θ -alumina before becoming α -Al₂O₃ in the range of 1,200~1,400 °C, depending on the procedure [11]. Recently several studies on the preparation of α -Al₂O₃ have tried to lower the formation temperature by using additives [12, 13]. It has been suggested that the metal-organic-derived alumina could lower the transformation temperature of α -Al₂O₃. In our previous researches [14, 15], we have also reported two papers; both were about mild temperature synthesis of α -Al₂O₃ using a chelating reagent as like ethylenediamine and a pre-microwave treatment,

resulted that α - Al_2O_3 structure was successfully obtained below $1,000^\circ\text{C}$. However, the crystallization temperature is still high. Therefore, new methods are needed to overcome the problem. In particular, the solvothermal method is an alternative to calcinations for promoting crystallization under mild temperatures. This process has been applied recently to the synthesis of small ceramic particles and films containing a range of metal oxides. Solvothermal treatments can be used to control the grain size, particle morphology, crystalline phases, and surface chemistry by regulating the sol composition, reaction temperatures, pressure, solvent nature, additives, and aging time. The particles prepared using the solvothermal method are expected to have a larger surface area, smaller particle size, and greater stability than those obtained by other methods, such as the sol-gel method. There are few reports of α - Al_2O_3 , which are prepared using the solvothermal method. Bell and Adair [16] have synthesized α -alumina in 1,4-butanediol solvent by reaction of gibbsite powder at 300°C for 36 h under a stirring rate of 460 rpm and autogenously pressures. They have also controlled the morphology through the use of special adsorbents in non-aqueous solution synthesis involves consideration of solvent degradation. Such studies are continuing, but without evident success as yet.

In this study, we have also tried to synthesize a special α - Al_2O_3 powder as a raw material for sapphire crystal growth in application to the LED industry. The α - Al_2O_3 structure in this study is controlled according to the effects of the pHs in the preparation step using a solvothermal method. The as-synthesized Al_2O_3 powders are characterized by X-ray diffraction (XRD) analysis, transmission electron microscopy (TEM), field emission scanning electron microscopy (FESEM), specific surface areas (Brunauer-Emmett-Teller, BET), X-ray photoelectron spectroscopy (XPS), and zeta potentials using electrophoresis light scattering (ELS) measurements.

2. Experimental

A solvothermal method was introduced in this study [16]. Gibbsite ($\text{Al}(\text{OH})_3$, sigmaaldrich.com/sigma-aldrich/home.html) was used as an aluminum precursor. First, the Gibbsite of 10.0 g was well dispersed in small amount of methanol with sonification for 1 h and then the colloidal solution was well mixed with excess 1,4-butanediol solvent for 2 h. The colloidal solution was thermally treated at 70°C for 24 h to remove methanol. Then acetic acid or ammonia water was slowly dropped into the solution to control pH = 4, 7, 9, and 11. The final solution was stirred homogeneously for 5 h, and then the solution was moved to a liner in autoclave, and finally the autoclave was heated in N_2 atmosphere at a rate of $10^\circ\text{C}/\text{min}$ to 300°C and then maintained isothermally at this temperature for 36 h and 70 atm. After solvothermal treatment, the obtained white powders were washed and dried. The synthesized Al_2O_3 were named to pH 4, 7, 9, and 11 according to pH of the final solution in the preparation step.

The as-synthesized Al_2O_3 powders were identified using powder XRD (model MPD, PANalytical, Yeungnam University Instrumental Analysis Center, Korea) with nickel-filtered $\text{CuK}\alpha$ radiation (30 kV, 30 mA) at 2-theta angles of 10 – 90° . The scan speed was $10^\circ/\text{min}$, and the time constant was 1 s. The sizes and shapes of the materials were measured by field emission SEM/energy-dispersive X-ray spectroscopy (FESEM/EDS; S-4100, Hitachi, Yeungnam University Instrumental Analysis Center, Korea). XPS measurements of the binding energy of Al_{2p} and O_{1s} orbitals in alumina powders were recorded with a model AXIS-NOVA (Kratos Inc., Korea Basic Science Institute Jeonju Center, Korea) system, equipped with a nonmonochromatic $\text{AlK}\alpha$ (1486.6 eV) X-ray source. The specific surface area was calculated according to the BET theory that gives the isotherm equation for multilayer adsorption by generalization of Langmuir's treatment of the unimolecular layer. The BET surface areas were measured using a Belsorp II instrument. The materials were degassed under vacuum at 120°C for 1 h before the BET surface measurements. Then the samples were thermally treated at 300°C for 30 min. The BET surface areas of the materials were measured through nitrogen gas adsorption using a continuous flow method with a mixture of nitrogen and helium as the carrier gas. The zeta potentials of the materials were determined by electrophoretic mobility using an electrophoresis measurement apparatus (ELS 8000, Otsuka Electronics, Japan) with a plate sample cell. ELS determinations were performed in the reference beam mode at a laser light source wavelength of 670 nm, modular frequency of 250 Hz, and scattering angle of 15° . The standard error of the zeta potentials, converted from the experimentally determined electrophoretic mobility, was typically $< 1.5\%$ and the percent error $< 5\%$. To measure the zeta potentials, 0.1 wt% of each sample was dispersed in deionized water and the pH of the solution was adjusted to 7. Relative sintered particle size distributions of the various pH solutions were also measured by using this equipment. Thermal gravimetric analysis measurements were collected using a TGA N-1000 (Scinco, Korea) thermal gravimetric analysis (TGA) equipped with a platinum crucible. Samples were heated from room temperature ($\sim 50^\circ\text{C}$) to 900°C with a heating rate of 5°C min^{-1} while the chamber was continuously purged with O_2 gases at a rate of 25 mL/min.

3. Results and Discussion

Figure 1 shows the XRD patterns of the four types as-synthesized Al_2O_3 powders according to various pH conditions after solvothermal treatment at 300°C for 36 h. The synthesized Al_2O_3 powder at pH = 4 exhibited peaks at 2 theta angles of 14.51, 28.22, 38.44, 49.18, 49.47, 55.19, 63.93, and 72.03° corresponding to the (d_{020}), (d_{120}), (d_{031}), (d_{200}), (d_{200}), (d_{220}), (d_{231}), and (d_{251}) spaces, respectively, and they were ascribed to the orthorhombic boehmite (AlOOH) structure [17]. However, the structures changed to the boehmite/ α - Al_2O_3 mixture at pH = 7. A significant result showed at pH = 9 that the XRD peaks assigned to α - Al_2O_3 were clearer and sharper without high thermal

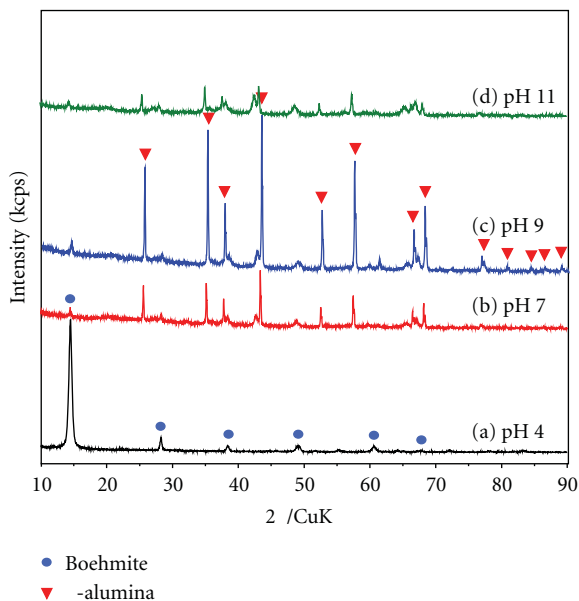


FIGURE 1: The XRD patterns of the Al_2O_3 powders as-solvothermally synthesized according to pHs.

treatment above $1,000^\circ\text{C}$. The synthesized $\alpha\text{-Al}_2\text{O}_3$ particle exhibited peaks at 2 theta angles of 25.57, 35.14, 37.76, 43.33, 46.16, 52.53, 57.47, 61.27, 66.49, 68.18, and 76.84, corresponding to the (d012), (d104), (d110), (d113), (d202), (d024), (d116), (d018), (d214), (d300) and (d1,0,10) spaces, respectively [18]. It was ascribed to the rhombohedral structure. Consequently, $\alpha\text{-Al}_2\text{O}_3$ was easily acquired with the solvothermal process, and it lowered the existing temperature by $500\sim 900^\circ\text{C}$, compared to the sol-gel process. These results revealed the pH effect on the crystallinity because of hydrolysis and poly-condensation in solvothermal treatment. This indicates that the rate of hydrolysis is governed by the hydronium ion in acidic solutions, so that the amount of water is small due to rapid formation of H_3O^+ . On the other hand, the reaction is controlled by the hydroxyl ions (OH^-) when powders are derived at $\text{pH} = 9$. The initial growth leads to a linear chain, but the high concentration of OH^- ions leads to crystallization because the probability of intermolecular reaction is higher than the intra-molecular reaction. The most probable metal-oxygen polymeric network, formed at high pH. The full width at half maximum (FWHM) height of the peak at $2\theta = 35.14^\circ$ (104) was measured, and the Scherrer equation [19], $t = 0.9\lambda/\beta \cos \theta$, where λ the wavelength of the incident X-rays, β , the FWHM in radians and θ the diffraction angle, was used to determine the crystalline domain size. The calculated crystalline domain size based on a special peak of 35.14° (d104) is 39.66 nm for the $\alpha\text{-Al}_2\text{O}_3$ powders synthesized at $\text{pH} = 9$.

TEM and SEM images of the solvothermally synthesized Al_2O_3 particles prepared at various pHs are shown in Figure 2. This figure revealed that the shapes varied according to the pH. At lower pH, the Al_2O_3 powder was close

to an orthorhombic rectangular shape. However, at neutral solution, the form was changed to cube/hexagonal mixture shape. In particular, it was transferred the $\alpha\text{-Al}_2\text{O}_3$ structure to the perfect hexagonal-shaped at $\text{pH} = 9$, and eventually it became huge square pillars of $1.5\sim 2.0\ \mu\text{m}$. However at higher pH, the shape was seemed to collapse.

The atomic compositions on the surface of the synthesized $\alpha\text{-Al}_2\text{O}_3$ powders were analyzed by EDS and the results are summarized in Table 1, which revealed the presence of Al and O as the only elementary components of two samples with an Al:O atomic ratio of about 6:4. In the samples synthesized in acidic solutions, the measured Al:O ratio revealed a little higher aluminum content than that in alkali solution of $\text{pH} 11$ in this study. However, at $\text{pH} = 9$ that represented $\alpha\text{-Al}_2\text{O}_3$ structure, the oxygen concentration was higher compared to the other phase's alumina.

Figure 3 presents the high-resolution spectra obtained from the quantitative XPS analyses of the as-synthesized four Al_2O_3 samples produced at various pHs. The survey spectra of materials contained Al_{2p} and O_{1s} peaks by XPS handbook [20]. It is well known that the $\text{Al}_{2p_{3/2}}$ orbital in α -type Al_2O_3 has a binding energy of $73.5\sim 74.2\ \text{eV}$, and this was assigned to Al^{3+} in Al_2O_3 and was almost same in $\text{pH} 4, 7, 9$, and 11 , which gave an $\text{Al}_{2p_{3/2}}$ orbital binding energy of $72.85\sim 73.29\ \text{eV}$. In general, a large binding energy indicates the presence of more oxidized states. In this study, the $\text{Al}_{2p_{3/2}}$ orbital binding energies were shifted to lower binding energy compared to the pure α -type Al_2O_3 represented in XPS handbook, which were assigned to reduced Al ions in Al_2O_3 . The O_{1s} region was decomposed into two contributions: metal-O ($\sim 530.2\ \text{eV}$) in the metal oxide and metal-OH ($531.0\ \text{eV}$). In general, a higher metal-OH peak indicates that particles are more hydrophilic. However, only a single peak was seen in all samples induced from $\text{pH} 4, 7, 9$, and 11 , at around $531\sim 532\ \text{eV}$, which was assigned to Al-O.

The BET surface areas of the materials were measured by nitrogen gas adsorption using a continuous flow method with a mixture of nitrogen and helium as the carrier gas. The pore size distribution is an important characteristic for porous materials. The relative pressure at which pore filling takes place by capillary condensation can be calculated from Kelvin's equation. By using Kelvin's equation, the pore radius in which the capillary condensation occurs actively can be determined as a function of the relative pressure (P/P_0). The mean pore diameter, D_p , was calculated from $D_p = 4VT/S$, where VT is the total volume of pores, and S the BET surface area. All isotherms belonged to type I-V according to the IUPAC classification [21]. The adsorption-desorption isotherms of N_2 at $77\ \text{K}$ for the four Al_2O_3 powders, were calculated as shown in Figure 4, and the values are also summarized in the table. All of Al_2O_3 samples in this study showed isotherms belong to III type in the IUPAC classification [22]. The synthesized Al_2O_3 samples in this study did not have any pores and however the BET surface area and pore volume were decreased in Al_2O_3 sample synthesized at $\text{pH} = 9$ to $26.18\ \text{m}^2\ \text{g}^{-1}$ and $0.249\ \text{cc/g}$, respectively, compared to the other Al_2O_3 samples. We expected from this result that the α -type Al_2O_3 derived from $\text{pH} = 9$ has a larger particle size and higher density.

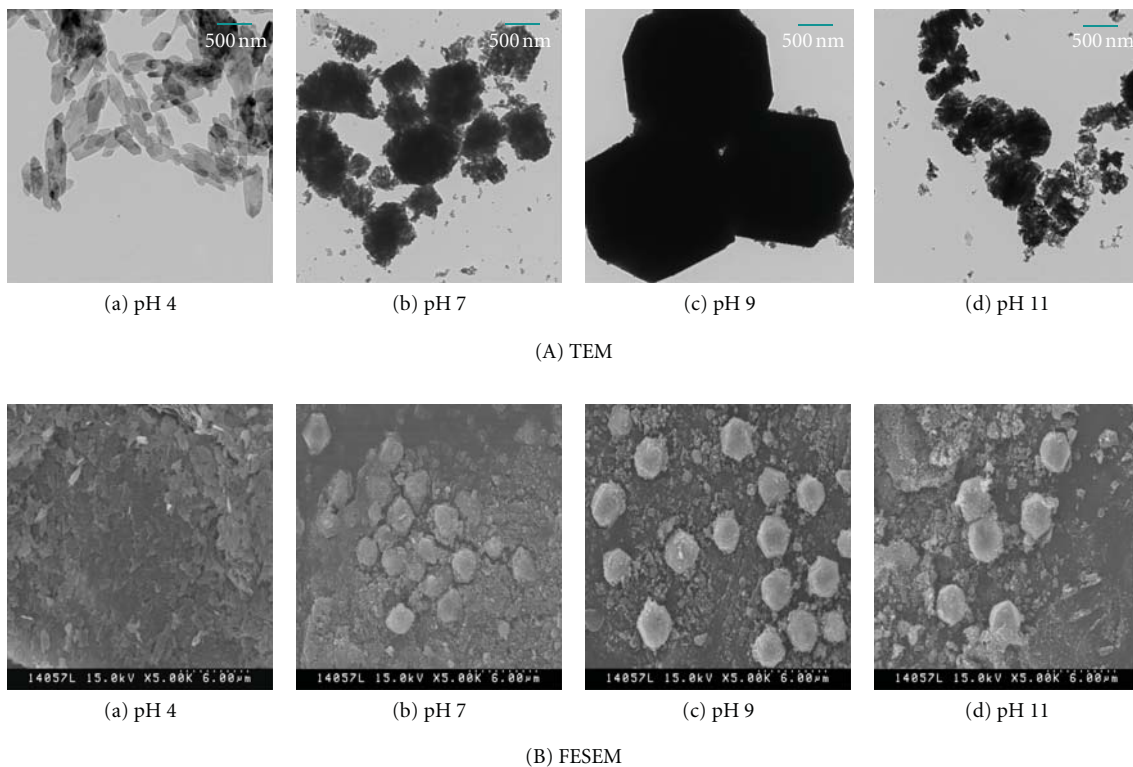


FIGURE 2: The TEM and FESEM images of the Al_2O_3 powders as-solvothermally synthesized according to pHs.

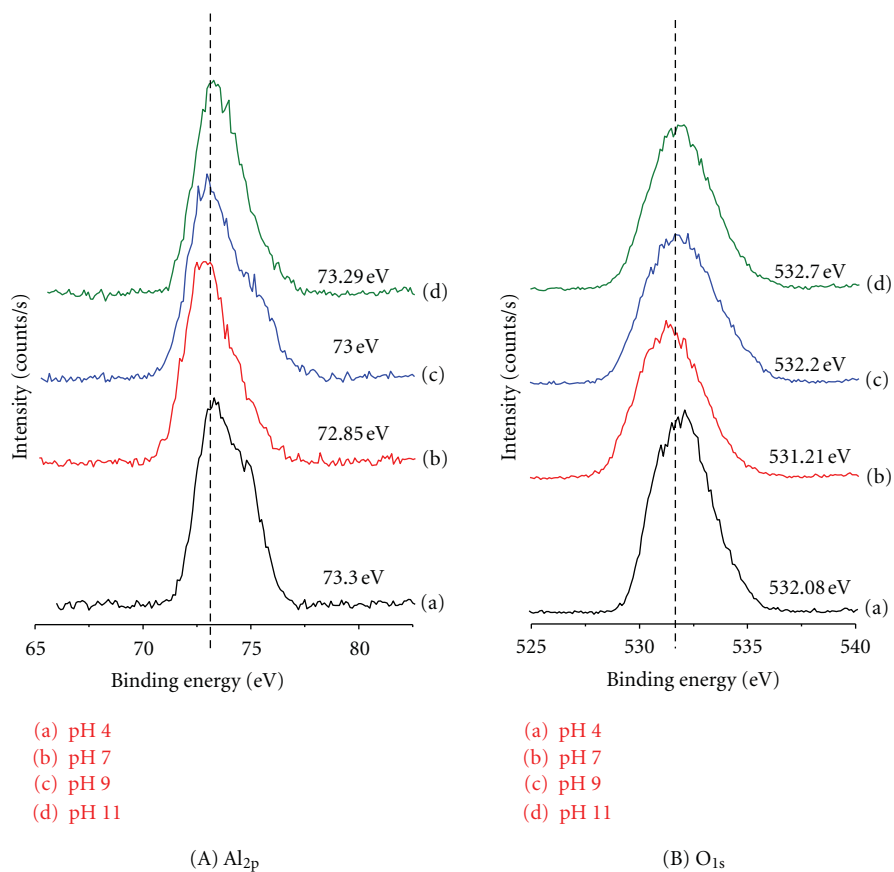
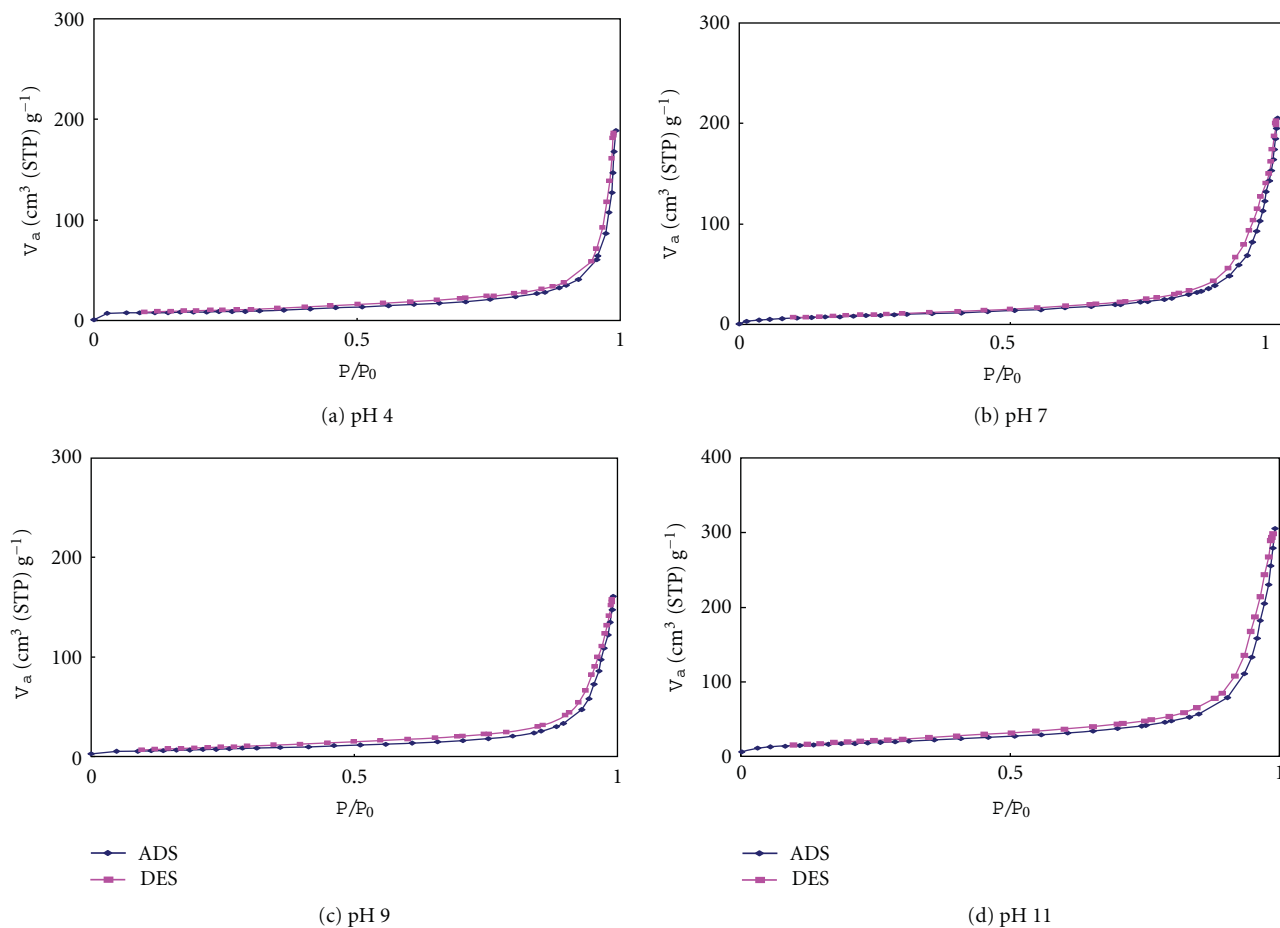


FIGURE 3: The XPS curves of the Al_2O_3 powders as-solvothermally synthesized according to pHs.



Samples	BET multipoint surface area (m ² /g)	Total pore volume (cc/g)	Bulk pore diameter (nm)
pH 4	28.02	0.292	41.69
pH 7	31.68	0.317	40.08
pH 9	26.18	0.249	37.99
pH 11	63.02	0.471	29.92

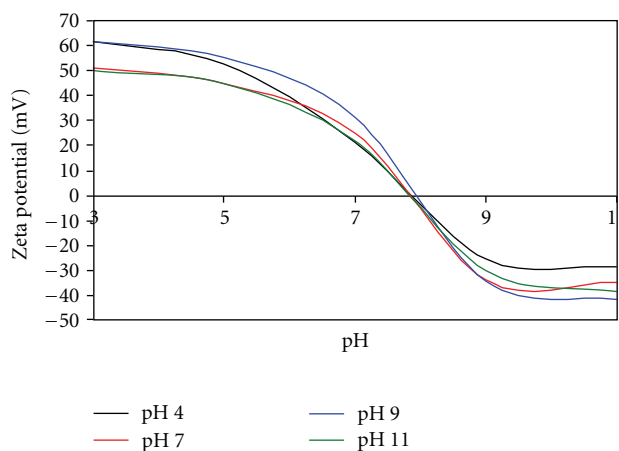
FIGURE 4: The adsorption-desorption isotherm curves of N₂ at 77 K on the Al₂O₃ powders as-solvothermally synthesized according to pHs.

TABLE 1: The atomic compositions analyzed by energy-dispersive X-ray spectroscopy (EDS) study on the Al₂O₃ powders as-solvothermally synthesized according to pHs.

Samples elements	pH 4		pH 7		pH 9		pH 11	
	Weight%	Atomic%	Weight%	Atomic%	Weight%	Atomic%	Weight%	Atomic%
O	55.89	68.12	49.37	62.19	45.79	58.76	51.15	63.85
Al	44.11	31.88	50.63	37.81	54.21	41.24	48.85	36.15
Total	100		100		100		100	

The zeta potential is an important parameter in colloidal stability, since it reflects the variation in surface potential for a specific material. These powders were derived from the solution route at low temperature; therefore, zeta potential studies were conducted to understand the surface charge

of these powders. Figure 5 shows the zeta potential data of an aqueous suspension of synthesized Al₂O₃ powders. No electrolyte was added to control the ionic strength of the solutions. The zeta potentials of all of the Al₂O₃ suspensions were significantly decreased with increasing pH. The surface



Samples pHs	pH 4		pH 7		pH 9		pH 11	
	A	B	A	B	A	B	A	B
pH = 3	61.49	797.3	51.06	1341.6	61.80	1893.4	50.10	1144.1
pH = 5	52.84	854.4	44.59	1418.7	55.26	2015.9	45.04	1378.5
pH = 7	21.28	1906.5	25.16	1681.4	31.14	2555.0	21.64	3997.4
pH = 9	-25.31	1051.7	-33.58	1581.6	-34.16	2319.5	-29.88	1934.4
pH = 11	-28.31	960.8	-34.99	1414.2	-41.60	2184.9	-38.49	1838.1

* A: zeta potential (mV) and B: aggregated particle size (nm) in aqueous solution.

FIGURE 5: The zeta potential data of an aqueous suspension of the Al_2O_3 powders as-solvothermally synthesized according to pHs.

charges were transferred from positive in acidic solution to negative in alkali solution. For $\alpha\text{-Al}_2\text{O}_3$ synthesized at pH = 9, the isoelectric point was at pH = 8 with large aggregation, and it positively charged to a maximum of 61.80 mV at pH = 3, which indicated that the $\alpha\text{-Al}_2\text{O}_3$ colloidal existed stably while having a small aggregation. Above this pH, the positive charge of the $\alpha\text{-Al}_2\text{O}_3$ particle was decreased with the same trend of mobility, resulting in an average aggregated diameter of 2,555 nm at pH = 7.

4. Conclusions

This study demonstrated the effect of pH in solvothermal synthesis to reduce the crystal growth temperature of $\alpha\text{-Al}_2\text{O}_3$ compared to ordinary methods. Most significantly, the solvothermal treatment produced rhombohedrally structured $\alpha\text{-Al}_2\text{O}_3$ with the hexagonal particle range of 1.5~2.0 μm at 300°C with pH = 9 and however the boehmite and mixed structures were seen at pH = 4, 7, and 11. The surface area was smaller in $\alpha\text{-Al}_2\text{O}_3$ synthesized at pH = 9. Electrophoretic light scattering (ELS) measurement in aqueous solution at pH = 3 revealed positive surface charges in the $\alpha\text{-Al}_2\text{O}_3$, which indicated that the $\alpha\text{-Al}_2\text{O}_3$ colloidal existed stably while having a small aggregation.

Acknowledgments

This research was financially supported by the Ministry of Education, Science and Technology (MEST) and National

Research Foundation of Korea (NRF) through the Human Resource Training Project for Regional Innovation.

References

- [1] S. M. Akselrod and J. F. Bruni, "Modern trends in crystal growth and new applications of sapphire," *Journal of Crystal Growth*, vol. 360, pp. 134–145, 2012.
- [2] W. J. Li, E. W. Shi, and Z. W. Yin, "Growth habit of rutile and $\alpha\text{-Al}_2\text{O}_3$ crystals," *Journal of Crystal Growth*, vol. 208, no. 1, pp. 546–554, 2000.
- [3] P. C. Borman and K. R. Westerterp, "An experimental study of the kinetics of the selective oxidation of ethene over a silver on α -alumina catalyst," *Industrial and Engineering Chemistry Research*, vol. 34, no. 1, pp. 49–58, 1995.
- [4] J. Goetz, M. A. Volpe, A. M. Sica, C. E. Gigola, and R. Touroude, "Low-loaded palladium on α -alumina catalysts: characterization by chemisorption, electron-microscopy, and photoelectron spectroscopy," *Journal of Catalysis*, vol. 153, no. 1, pp. 86–93, 1995.
- [5] A. Janbey, R. K. Pati, S. Tahir, and P. Pramanik, "A new chemical route for the synthesis of nano-crystalline $\alpha\text{-Al}_2\text{O}_3$ powder," *Journal of the European Ceramic Society*, vol. 21, no. 12, pp. 2285–2289, 2001.
- [6] P. K. Sharma, V. V. Varadan, and V. K. Varadan, "A critical role of pH in the colloidal synthesis and phase transformation of nano size $\alpha\text{-Al}_2\text{O}_3$ with high surface area," *Journal of the European Ceramic Society*, vol. 23, no. 5, pp. 659–666, 2003.
- [7] W. L. Suchanek, "Hydrothermal synthesis of alpha alumina ($\alpha\text{-Al}_2\text{O}_3$) powders: study of the processing variables and growth mechanisms," *Journal of the American Ceramic Society*, vol. 93, no. 2, pp. 399–412, 2010.

- [8] K. Laishram, R. Mann, and N. Malhan, "A novel microwave combustion approach for single step synthesis of α - Al_2O_3 nanopowders," *Ceramics International*, vol. 38, pp. 1703–1706, 2012.
- [9] F. Mirjalili, M. Hasmaliza, and L. C. Abdullah, "Size-controlled synthesis of nano α -alumina particles through the sol-gel method," *Ceramics International*, vol. 36, no. 4, pp. 1253–1257, 2010.
- [10] J. Li, Y. Pan, C. Xiang, Q. Ge, and J. Guo, "Low temperature synthesis of ultrafine α - Al_2O_3 powder by a simple aqueous sol-gel process," *Ceramics International*, vol. 32, no. 5, pp. 587–591, 2006.
- [11] S. Rajendran, "Production of ultrafine alpha alumina powders and fabrication of fine grained strong ceramics," *Journal of Materials Science*, vol. 29, no. 21, pp. 5664–5672, 1994.
- [12] J. Li, Y. Wu, Y. Pan, W. Liu, and J. Guo, "Influence of fluorides on phase transition of α - Al_2O_3 formation," *Ceramics International*, vol. 33, no. 6, pp. 919–923, 2007.
- [13] H. J. Kim, T. G. Kim, J. J. Kim, S. S. Park, S. S. Hong, and G. D. Lee, "Influences of precursor and additive on the morphology of nanocrystalline α -alumina," *Journal of Physics and Chemistry of Solids*, vol. 69, no. 5–6, pp. 1521–1524, 2008.
- [14] J. S. Lee, H. S. Kim, J. S. Lee, N.-K. Park, T. J. Lee, and M. Kang, "Synthesis of α - Al_2O_3 at mild temperatures by controlling aluminum precursor, pH, and ethylenediamine chelating additive," *Ceramics International*, vol. 38, pp. 6685–6691, 2012.
- [15] H. S. Kim, N.-K. Park, T. J. Lee, M.-H. Um, and M. Kang, "Preparation of nanosized α - Al_2O_3 particles using a microwave pretreatment at mild temperature," *Advances in Materials Science and Engineering*, vol. 2012, pp. 1–6, 2012.
- [16] N. S. Bell and J. H. Adair, "Adsorbate effects on glycothermally produced α -alumina particle morphology," *Journal of Crystal Growth*, vol. 203, no. 1, pp. 213–226, 1999.
- [17] A. Boumaza, L. Favaro, J. Lédion et al., "Transition alumina phases induced by heat treatment of boehmite: an X-ray diffraction and infrared spectroscopy study," *Journal of Solid State Chemistry*, vol. 182, no. 5, pp. 1171–1176, 2009.
- [18] H. Liu, G. Ning, Z. Gan, and Y. Lin, "Emulsion-based synthesis of unaggregated, spherical alpha alumina," *Materials Letters*, vol. 62, no. 10–11, pp. 1685–1688, 2008.
- [19] A. W. Burton, K. Ong, T. Rea, and I. Y. Chan, "On the estimation of average crystallite size of zeolites from the Scherrer equation: a critical evaluation of its application to zeolites with one-dimensional pore systems," *Microporous and Mesoporous Materials*, vol. 117, no. 1–2, pp. 75–90, 2009.
- [20] J. F. Moulder, W. F. Stickle, P. E. Sobal, and K. D. Bomben, *Hand Book of X-Ray Photoelectron Spectroscopy*, Perkin-Elmer Corporation, Eden Prairie, Minn, USA, 1992.
- [21] M. Khalfaoui, S. Knani, M. A. Hachicha, and A. B. Lamine, "New theoretical expressions for the five adsorption type isotherms classified by BET based on statistical physics treatment," *Journal of Colloid and Interface Science*, vol. 263, no. 2, pp. 350–356, 2003.
- [22] M. D. Donohue and G. L. Aranovich, "Classification of Gibbs adsorption isotherms," *Advances in Colloid and Interface Science*, vol. 76, pp. 137–152, 1998.

Research Article

Study on Nanostructures Induced by High-Current Pulsed Electron Beam

Bo Gao, Yi Hao, Ganfeng Tu, and Wenyuan Wu

School of Materials and Metallurgy, Northeastern University, Shenyang, Liaoning 110004, China

Correspondence should be addressed to Bo Gao, surfgao@yahoo.com.cn

Received 30 November 2012; Accepted 8 December 2012

Academic Editor: Jianxin Zou

Copyright © 2012 Bo Gao et al. This is an open access article distributed under the Creative Commons Attribution License, which permits unrestricted use, distribution, and reproduction in any medium, provided the original work is properly cited.

Four techniques using high-current pulsed electron beam (HCPEB) were proposed to obtain surface nanostructure of metal and alloys. The first method involves the distribution of several fine Mg nanoparticles on the top surface of treated samples by evaporation of pure Mg with low boiling point. The second technique uses superfast heating, melting, and cooling induced by HCPEB irradiation to refine the primary phase or the second phase in alloys to nanosized uniform distributed phases in the matrix, such as the quasicrystal phase $\text{Mg}_{30}\text{Zn}_{60}\text{Y}_{10}$ in the quasicrystal alloy $\text{Mg}_{67}\text{Zn}_{30}\text{Y}_3$. The third technique involves the refinement of eutectic silicon phase in hypereutectic Al-15Si alloys to fine particles with the size of several nanometers through solid solution and precipitation refinement. Finally, in the deformation zone induced by HCPEB irradiation, the grain size can be refined to several hundred nanometers, such as the grain size of the hypereutectic Al-15Si alloys in the deformation zone, which can reach ~ 400 nm after HCPEB treatment for 25 pulses. Therefore, HCPEB technology is an efficient way to obtain surface nanostructure.

1. Introduction

Nanomaterials are typically characterized by ultrafine grains [1]. They fundamentally possess several unique properties and behavior such as increased strength/hardness, enhanced diffusivity, enhanced thermal expansion coefficient, and superior soft magnetic properties [2] compared with the conventional coarse-grained materials. With continuous discovery of the unique properties of nanomaterials in recent years, various processing techniques have been developed to synthesize bulk nanomaterials, such as ultrafine powder consolidation [3], amorphous solid crystallization [4], ball milling [5], and severe plastic deformation [6].

High-current pulsed electron beam (HCPEB) technique, as a novel and valid method [7, 8] used for material surface modification, is long considered to be a very simple, reliable, and highly efficient method. The electron beam generates intense and superfast melting, evaporation, solidification, and even ablation on the surface of target materials together with the formation of thermal stress and shock waves. Therefore, the depth of the HCPEB modification zone can reach several hundred micrometers [9–12], which greatly

satisfies the modification demands for engineering materials. The combination of these influencing factors, peculiar to HCPEB treatment, can lead to the nanocrystalline formation in near-surface layers of metallic materials [13, 14].

Hence, four methods involving HCPEB technology were proposed to obtain surface nanocrystalline formation in this paper.

2. Experimental Procedures

2.1. Starting Materials and HCPEB Treatment. The starting materials in this experiment were pure Mg (99.7 wt%), $\text{Mg}_{67}\text{Zn}_{30}\text{Y}_3$ quasicrystal alloy (with a chemical composition of Zn (50.86 wt%), Y (7.02 wt%), and Mg balance), and hypereutectic Al-15Si alloy (with chemical composition of Si (15 wt%) and Al balance). Prior to HCPEB treatment, the samples were cut into $\Phi 10 \text{ mm} \times 9 \text{ cm}$ cylinders, with surfaces that were mechanically polished and washed by absolute ethyl alcohol. Then, the sample surfaces were treated through “Nadezhda-2” type HCPEB system, with the following working parameters: accelerating voltage, 23 kV;

energy density, 1 J/cm^2 to 3 J/cm^2 ; pulse duration, $\sim 1 \mu\text{s}$; and pulse number, 10 for pure Mg and quasicrystal alloy $\text{Mg}_{67}\text{Zn}_{30}\text{Y}_3$ and 25 for hypereutectic Al-15Si alloy.

2.2. Microstructural Analysis. The sample surface and cross-section morphologies were analyzed using a field emission gun scanning electron microscope (SEM) (Jeol JSM 6500 F) with EBSD acquisition camera and Channel 5 software. The beam control mode was applied for automatic orientation mapping with a step size of $0.04 \mu\text{m}$. Thin films for transmission electron microscopy (TEM) were prepared by grinding, dimpling, and ion-beam thinning, and the microstructure characteristics were observed in a transmission electron microscope (FEI-Tecna G220).

3. Results and Discussion

The characteristics of the obtained nanostructures according to the four techniques using HCPEB treatment are discussed as follows.

3.1. Surface Characteristics of Pure Mg after HCPEB Treatment. Figure 1 illustrates the surface SEM morphology of HCPEB-treated pure Mg for 10 pulses under energy density of 3 J/cm^2 . Several separated bulges are evident, and numerous fine particles were observed between and on top of these bulges. The chemical composition of the fine particles is determined to be pure Mg using EDS analysis, and the size of the fine particles ranges from several hundred nanometers to several micrometers. Pure Mg vaporizes on the top surface of the treated sample. The special morphology formation can be explained as follows. First, the surface temperature of the HCPEB-treated Mg reaches boiling point, vaporization occurs at a given depth determined by the energy density of HCPEB, and a considerable amount of bubbles form in the liquid Mg solution. Second, when the bubbles reach the top surface, the abruption of these bubbles induces shock effect on the nearby zone and a large number of fine particles will erupt simultaneously. Finally, these fine erupted particles fall to the top frozen surface under the effect of gravity, and the special surface morphology as seen in Figure 1 is formed.

Thus, vaporization behavior induced by HCPEB treating low-boiling point metal can produce abundant fine particles with sizes ranging from several hundred nanometers to several micrometers.

3.2. Microstructure Characteristics of $\text{Mg}_{67}\text{Zn}_{30}\text{Y}_3$ Quasicrystal Alloy before and after HCPEB Treatment. Figure 2 demonstrates the surface back-scattered electron (BSE) images of $\text{Mg}_{67}\text{Zn}_{30}\text{Y}_3$ quasicrystal alloy in the initial state and after HCPEB treatment for 10 pulses. Figure 2(a) depicts the initial microstructure characteristics of $\text{Mg}_{67}\text{Zn}_{30}\text{Y}_3$ quasicrystal alloy, consisting of gray matrix phase Mg_7Zn_3 , black dendrite α -Mg phase, and white petal-shaped quasicrystal $\text{Mg}_{30}\text{Zn}_{60}\text{Y}_{10}$ phase [15]. The phase contrast change is mainly attributed to the different contents of Mg element in the different phases. Two types of dendrites are both Mg-rich phases and have few solid solution of Y element. By contrast,

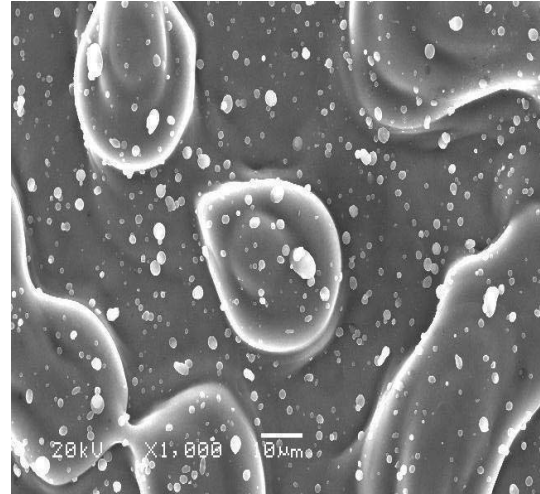


FIGURE 1: Surface SEM morphology of HCPEB-treated pure Mg with 10 pulses under energy density of 3 J/cm^2 .

the white petal-shaped phase consists of the following: Mg, 37.496%; Zn, 53.022%; and Y, 9.482%. Although a certain deviation from the quasicrystal $\text{Mg}_{30}\text{Zn}_{60}\text{Y}_{10}$ phase in standard ternary Mg-Zn-Y alloy is reported in [13], the phase should be the quasicrystal $\text{Mg}_{30}\text{Zn}_{60}\text{Y}_{10}$ from the typical petal morphology, and the deviation is probably caused by the EDS test error. Figure 2(b) illustrates the typical surface morphology of $\text{Mg}_{67}\text{Zn}_{30}\text{Y}_3$ quasicrystal alloy after HCPEB treatment for 10 pulses. The phase boundaries between different phases become clear, and the coarse petal phase disappears. During multiple HCPEB treatments, the top surface of the treated sample undergoes repeated melting and solidification. The chemical composition tends to distribute uniformly as a result of the chemical composition diffusion during the HCPEB process, forming the special morphology (Figure 2(b)). However, determining the accurate size of the quasicrystal $\text{Mg}_{30}\text{Zn}_{60}\text{Y}_{10}$ phase after 10-pulse treatment by SEM observation is quite difficult.

Figures 2(c) and 2(d) illustrate the TEM observations of the quasicrystal phase of the $\text{Mg}_{67}\text{Zn}_{30}\text{Y}_3$ quasicrystal alloy before and after HCPEB treatment. Figure 2(c) demonstrates the TEM bright field image of the initial sample and corresponding SAED pattern (five-fold symmetry). A black petal-shaped phase is observed under TEM view. Through the identification of the SAED pattern with five-fold symmetry, the petal-shaped phase is considered as quasicrystal $\text{Mg}_{30}\text{Zn}_{60}\text{Y}_{10}$ with icosahedral structure of quasiperiodic structure arrangement. This result further confirms the observations obtained from SEM. In addition, several fine branches are formed in the vicinity of the large petal-shaped quasicrystal phase, known as the two-fold axis of quasicrystal growth. Figure 2(d) illustrates the TEM bright field image of a 10-pulse-treated sample and corresponding SAED pattern (diffraction rings). After HCPEB treatment for 10 pulses, a considerable amount of nanosized particles with grain size of approximately 10 nm to 30 nm is uniformly distributed in surface layer. The interplanar

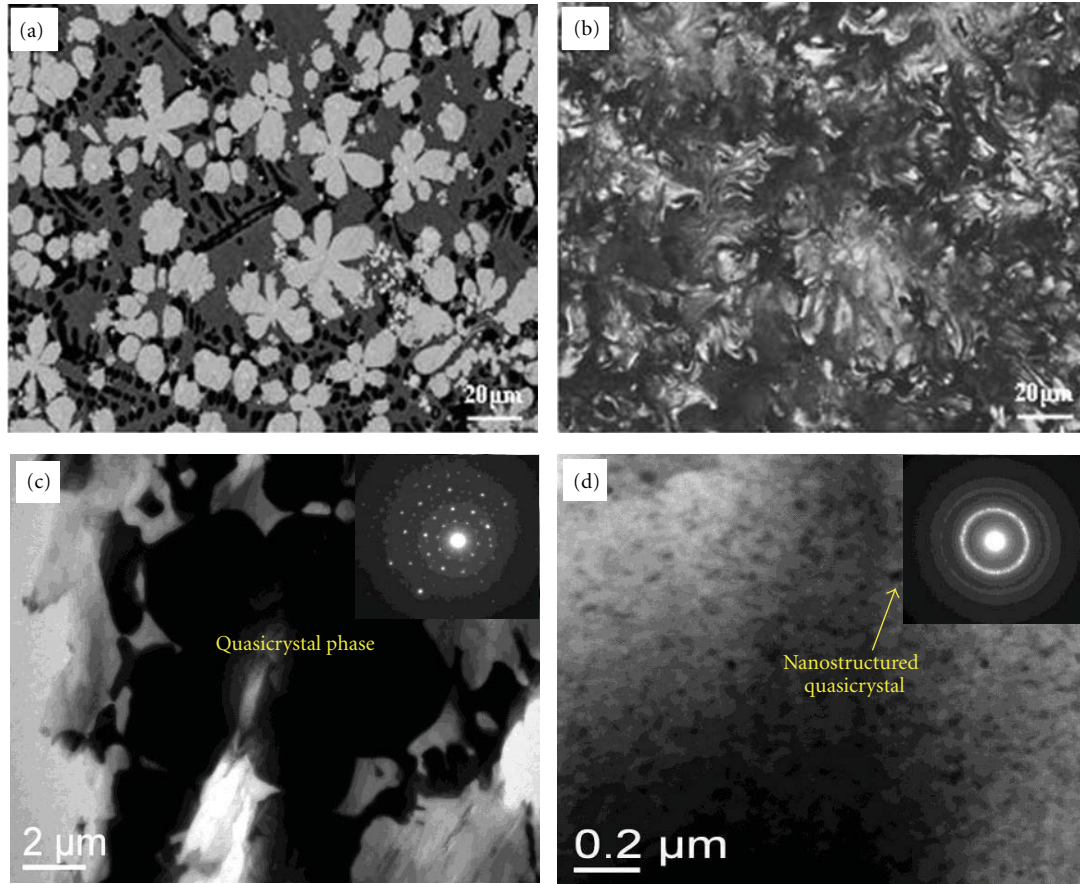


FIGURE 2: SEM and TEM morphology of quasicrystal $\text{Mg}_{67}\text{Zn}_{30}\text{Y}_3$ alloy before and after HCPEB treatment under energy density of $\sim 2.5 \text{ J/cm}^2$ and 10 pulses (SEM morphology of quasicrystal $\text{Mg}_{67}\text{Zn}_{30}\text{Y}_3$ alloy (a) before and (b) after HCPEB treatment, TEM morphology of quasicrystal phase (c) in initial sample and corresponding SAED pattern, (d) in treated sample and corresponding SAED pattern).

spacing values corresponding to each diffraction ring were calculated and compared with interplanar spacing (d_{stan}) values of acknowledged quasicrystal $\text{Mg}_{30}\text{Zn}_{60}\text{Y}_{10}$. Hence, the dispersed metastable nanocrystalline phase is identified to be the quasicrystal phase $\text{Mg}_{30}\text{Zn}_{60}\text{Y}_{10}$. Thus, a melted layer containing a large number of nanostructured quasicrystal phases is obtained by the HCPEB treatment.

Hence, using HCPEB multiple bombardments, the coarse petal quasicrystal phase $\text{Mg}_{30}\text{Zn}_{60}\text{Y}_{10}$ can be refined to dispersed distribution nanostructured quasicrystal phase.

3.3. Microstructure Characteristics of Hypereutectic Al-15Si Alloy before and after HCPEB Treatment. Figure 3 depicts the SEM surface morphology of hypereutectic Al-15Si alloy before and after HCPEB treatment under energy density of $\sim 3 \text{ J/cm}^2$. For the initial sample shown in Figure 3(a), the Al-Si eutectic structure in as-cast hypereutectic Al-15Si alloy is clearly observed by SEM. In addition, a small number of coarse primary Si phases with size of several ten micrometers are distributed randomly on the surface. For the 25 pulse-treated sample shown in Figure 3(b), the eutectic structure disappears completely after HCPEB treatment and numerous cellular cells ($\sim 100 \text{ nm}$ wide) are uniformly distributed

on the top surface. Additionally, a remarkable amount of Si nanoparticles is precipitated on the boundary of the nanocellular cell structure. Most of the eutectic Si phase of initial sample solid dissolves in the α -Al and forms the supersaturated solid solution. Some of the Si element precipitate from the supersaturated solid solution during the rapid solidification. The estimated size of the Si nanoparticles ranges from 5 nm to 50 nm. Thus, the size of eutectic Si phase can be refined to 5 ~ 50 nm after HCPEB treatment.

This process is the third way to obtain nanostructure by solid solution and precipitation refinement induced by HCPEB treatment.

3.4. Microstructure Characteristics of Deformation Zone of HCPEB-Treated Hypereutectic Al-15Si Alloy. A deformation zone can be found under the melted layer of the HCPEB-treated sample, but few studies on the grain size distribution in this zone have been reported. Figure 4(a) illustrates the SEM morphology image of this deformation zone (distance from the top surface approximately from $10 \mu\text{m}$ to $30 \mu\text{m}$). Several fine Si particles are distributed in this zone, and the initial eutectic Si phases are deduced to be transformed to

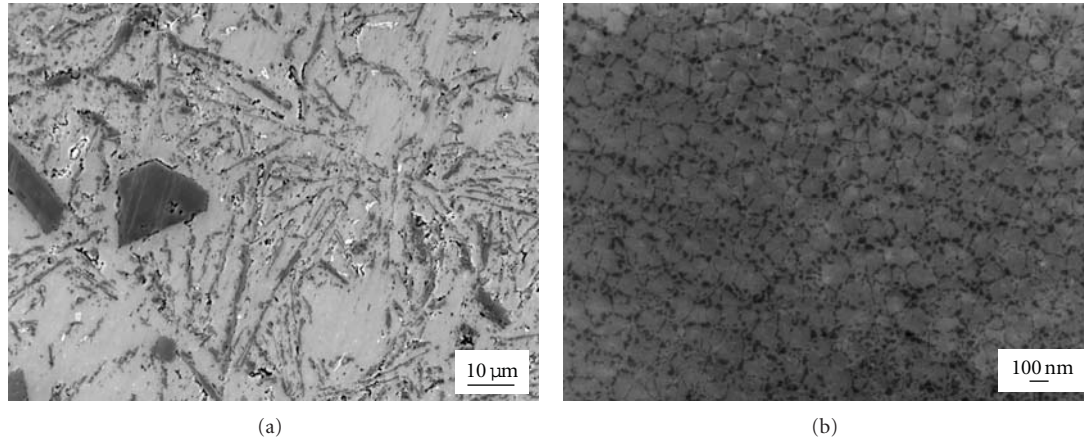


FIGURE 3: SEM surface morphology of hypereutectic Al-15Si (a) before HCPEB treatment and (b) after 25-pulse treatment under energy density of $\sim 3 \text{ J/cm}^2$.

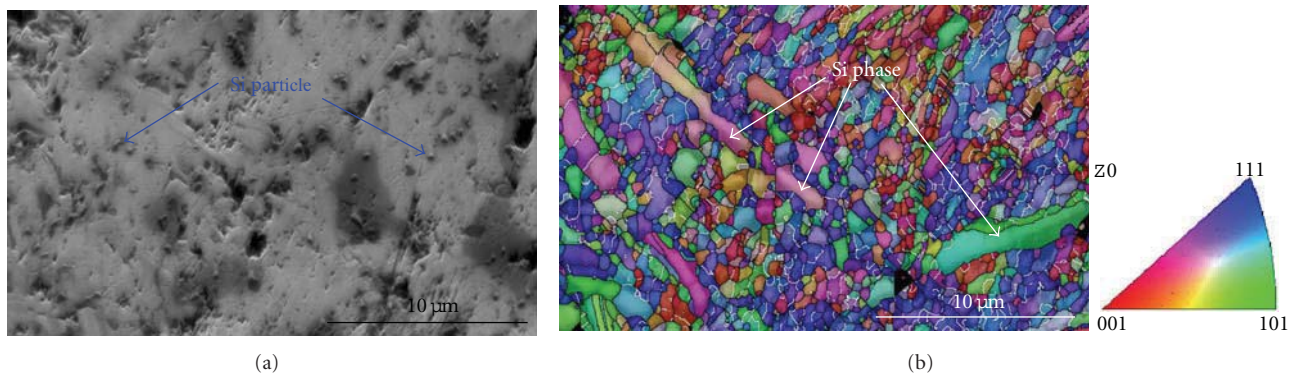


FIGURE 4: Cross-section morphology of HCPEB-treated hypereutectic Al-15Si alloy heat-affected zone for 25 pulses (a) and corresponding EBSD orientation map.

these fine particles as a result of microplastic deformation induced by multiple HCPEB shock wave impacts. From the corresponding EBSD orientation map (Figure 4(b)), several large lamellar primary Si phases were subdivided into several grains under multiple plastic deformations induced by the shock wave, and some Si phases release coupled stress as seen in Figure 4(b) and refined to several hundred nm. For the Al matrix, the grains were transformed from coarse dendrite crystal to fine equiaxed crystal with size of $\sim 300 \text{ nm}$ (Figure 4(b)). And the preferred orientation for Al phase in this zone is $[111]$ direction, which is parallel to propagation direction of shock wave.

To show the grain distribution clearly, Figure 5(a) illustrates the EBSD grain map, white lines present the low angel grain boundary (grain orientation difference between 3° and 10°), and black lines present the high angel grain boundary (orientation difference over 10°). Figure 5(b) provides the corresponding grain size distribution map in this zone with an orientation difference of over 3° . Figure 5(a) shows that numerous low-angel grain boundaries are formed resulting from severe plastic deformation induced by the HCPEB shock wave impact. Most of the grains are less than $1 \mu\text{m}$ in size, and the average grain size is approximately 460 nm from

statistical result of all the grain sizes in the deformation zone (Figure 5(b)).

Hence, the grain size in the deformation zone under melted layer can reach several hundred nanometers after multiple pulses treatment of HCPEB. This is the fourth way to obtain a nanostructure by HCPEB treatment.

4. Conclusions

This work investigated the different techniques involving HCPEB treatment to obtain nanostructure for pure Mg, quasicrystal Mg alloy $\text{Mg}_{67}\text{Zn}_{30}\text{Y}_3$, and hypereutectic Al-15Si alloy. The main results are as follows.

- (1) A considerable amount of fine particles with sizes from several hundred nanometers to several micrometers are distributed on the top surface of treated pure Mg sample as a result of vaporization behavior induced by HCPEB treating.
- (2) After 10 pulses of HCPEB treatment for quasicrystal Mg alloy $\text{Mg}_{67}\text{Zn}_{30}\text{Y}_3$, the phase boundaries between different phases become more apparent because of repeated melting and solidification. The surface

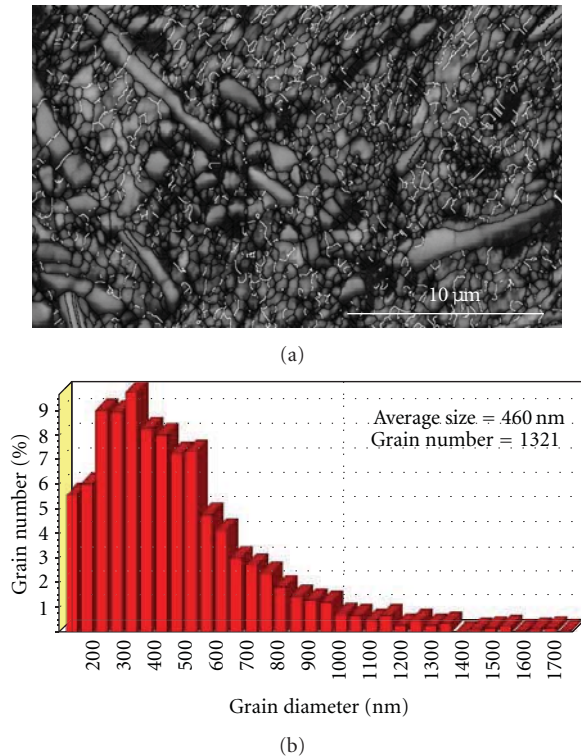


FIGURE 5: EBSD grain map of HCPEB-treated hypereutectic Al-15Si alloy heat-affectation zone for (a) 25 pulses and (b) corresponding grain size distribution under grain orientation difference of over 3° .

chemical composition tends to be homogeneously distributed. A large number of nano quasicrystal $\text{Mg}_{30}\text{Zn}_{60}\text{Y}_{10}$ phases are formed with size of approximately 10 nm to 30 nm.

- (3) After 25 pulses of HCPEB treatment for hypereutectic Al-15Si alloy, many cellular cells with ~ 100 nm diameter are uniformly distributed on the top surface. In addition, a number of Si nanoparticles (5 nm to 50 nm) are precipitated on the boundary of the nanocellular cell structure.
- (4) After 25 pulses of HCPEB treatment for hypereutectic Al-15Si alloy, the grain size in the deformation zone induced by multiple HCPEB shock wave impacts can reach several hundred nanometers.

Acknowledgments

The authors would like to acknowledge the support from the Fundamental Research Funds for the Central Universities (N090602009 and N100402010) and the key projects in the National Science & Technology Pillar Program during the eleventh five-year plan period (2009BAE80B01).

References

- [1] G. Liu, J. Lu, and K. Lu, "Surface nanocrystallization of 316L stainless steel induced by ultrasonic shot peening," *Materials Science and Engineering A*, vol. 286, no. 1, pp. 91–95, 2000.

- [2] C. Suryanarayana, "Nanocrystalline materials," *International Materials Reviews*, vol. 40, no. 2, pp. 41–64, 1995.
- [3] X. Zhang, H. Wang, M. Kassem, J. Narayan, and C. C. Koch, "Preparation of bulk ultrafine-grained and nanostructured Zn, Al and their alloys by in situ consolidation of powders during mechanical attrition," *Scripta Materialia*, vol. 46, no. 9, pp. 661–665, 2002.
- [4] T. Nagase, M. Nakamura, and Y. Umakoshi, "Electron irradiation induced nano-crystallization in $\text{Zr}_{66.7}\text{Ni}_{33.3}$ amorphous alloy and $\text{Zr}_{60}\text{Al}_{15}\text{Ni}_{25}$ metallic glass," *Intermetallics*, vol. 15, no. 2, pp. 211–224, 2007.
- [5] T. P. Yadav, N. K. Mukhopadhyay, R. S. Tiwari, and O. N. Srivastava, "Studies on the formation and stability of nano-crystalline $\text{Al}_{50}\text{Cu}_{28}\text{Fe}_{22}$ alloy synthesized through high-energy ball milling," *Materials Science and Engineering A*, vol. 393, no. 1-2, pp. 366–373, 2005.
- [6] M. N. Ahmadabadi, H. Shirazi, H. Ghasemi-Nanesa, S. H. Nedjad, B. Poorganji, and T. Furuha, "Role of severe plastic deformation on the formation of nanograins and nano-sized precipitates in Fe-Ni-Mn steel," *Materials and Design*, vol. 32, no. 6, pp. 3526–3531, 2011.
- [7] S. Hao, P. Wu, J. Zou, T. Grosdidier, and C. Dong, "Microstructure evolution occurring in the modified surface of 316L stainless steel under high current pulsed electron beam treatment," *Applied Surface Science*, vol. 253, no. 12, pp. 5349–5354, 2007.
- [8] T. Grosdidier, J. X. Zou, N. Stein, C. Boulanger, S. Z. Hao, and C. Dong, "Texture modification, grain refinement and improved hardness/corrosion balance of a FeAl alloy by pulsed electron beam surface treatment in the "heating mode"," *Scripta Materialia*, vol. 58, no. 12, pp. 1058–1061, 2008.
- [9] J. X. Zou, K. M. Zhang, S. Z. Hao, C. Dong, and T. Grosdidier, "Mechanisms of hardening, wear and corrosion improvement of 316 L stainless steel by low energy high current pulsed electron beam surface treatment," *Thin Solid Films*, vol. 519, no. 4, pp. 1404–1415, 2010.
- [10] Y. Qin, C. Dong, Z. F. Song et al., "Deep modification of materials by thermal stress wave generated by irradiation of high-current pulsed electron beams," *Journal of Vacuum Science & Technology A*, vol. 23, pp. 430–435, 2009.
- [11] J. X. Zou, T. Grosdidier, K. M. Zhang, B. Gao, S. Z. Hao, and C. Dong, "Microstructures and phase formations in the surface layer of an AISI D2 steel treated with pulsed electron beam," *Journal of Alloys and Compounds*, vol. 434-435, pp. 707–709, 2007.
- [12] J. Zou, T. Grosdidier, K. Zhang, and C. Dong, "Mechanisms of nanostructure and metastable phase formations in the surface melted layers of a HCPEB-treated D2 steel," *Acta Materialia*, vol. 54, no. 20, pp. 5409–5419, 2006.
- [13] Q. F. Guan, H. Zou, G. T. Zou et al., "Surface nanostructure and amorphous state of a low carbon steel induced by high-current pulsed electron beam," *Surface and Coatings Technology*, vol. 196, no. 1-3, pp. 145–149, 2005.
- [14] Y. Hao, B. Gao, G. F. Tu, S. W. Li, C. Dong, and Z. G. Zhang, "Improved wear resistance of Al-15Si alloy with a high current pulsed electron beam treatment," *Nuclear Instruments and Methods in Physics Research B*, vol. 269, no. 13, pp. 1499–1505, 2011.
- [15] A. P. Tsai, A. Inoue, and T. Masumoto, "Stoichiometric icosahedral phase in the ZnMgY system," *Journal of Materials Research*, vol. 12, pp. 1468–1471, 1997.

Research Article

Preparation and Hydrogen Storage Properties of Mg-Rich Mg-Ni Ultrafine Particles

Jianxin Zou,^{1,2} Haiquan Sun,¹ Xiaoqin Zeng,^{1,2} Gang Ji,³ and Wenjiang Ding^{1,2}

¹ Shanghai Engineering Research Center of Magnesium Materials and Applications and National Engineering Research Center of Light Alloy Net Forming, Shanghai Jiao Tong University, Shanghai 200240, China

² State Key Laboratory of Metal Matrix Composites, School of Materials Science and Engineering, Shanghai Jiao Tong University, Shanghai 200240, China

³ Unité Matériaux Et Transformations (UMET), CNRS UMR 8207, Université Lille 1, 59655 Villeneuve d'Ascq, France

Correspondence should be addressed to Jianxin Zou, zoujx@sjtu.edu.cn

Received 29 August 2012; Accepted 16 October 2012

Academic Editor: Kemin Zhang

Copyright © 2012 Jianxin Zou et al. This is an open access article distributed under the Creative Commons Attribution License, which permits unrestricted use, distribution, and reproduction in any medium, provided the original work is properly cited.

In the present work, Mg-rich Mg-Ni ultrafine powders were prepared through an arc plasma method. The phase components, microstructure, and hydrogen storage properties of the powders were carefully investigated. It is found that Mg_2Ni and MgNi_2 could be obtained directly from the vapor state reactions between Mg and Ni, depending on the local vapor content in the reaction chamber. A nanostructured $\text{MgH}_2 + \text{Mg}_2\text{NiH}_4$ hydrogen storage composite could be generated after hydrogenation of the Mg-Ni ultrafine powders. After dehydrogenation, MgH_2 and Mg_2NiH_4 decomposed into nanograined Mg and Mg_2Ni , respectively. Thermogravimetry/differential scanning calorimetry (TG/DSC) analyses showed that Mg_2NiH_4 phase may play a catalytic role in the dehydriding process of the hydrogenated Mg ultrafine particles.

1. Introduction

Mg-based alloys and composites are believed to be promising candidates as hydrogen storage carriers due to their high hydrogen storage capacity (7.6 wt% for MgH_2 and 3.6 wt% for Mg_2NiH_4), great abundance, and low cost [1]. However, the sluggish hydrogen sorption kinetics and high operating temperature of Mg (>573 K) limit its practical applications. Different methods, such as alloying, catalyst addition, and nanocrystallization, have been used to improve the hydrogen thermodynamics and sorption kinetics of Mg [2–4]. Consequently, various Mg-based alloys, composites, and compounds have been developed with superior hydrogen sorption kinetics over pure Mg. Among those Mg-based materials, Mg_2Ni intermetallic compound is well known to form Mg_2NiH_4 hydride with high reaction rate, which has a hydrogen storage capacity of 3.6 wt% [1]. However, it is difficult to obtain Mg alloys with accurately desirable compositions by conventional melt-cast methods due to following reasons: (1) Mg has low melting point (923 K) and high vapor pressure (133 Pa at 878 K); (2) Mg is quite active

in the presence of oxygen. Especially in the case of Mg-Ni binary system, casting is quite difficult because of the large difference in melting point between Ni (1728 K) and Mg (923 K). Furthermore, based on the binary phase diagram [5, 6], single phase Mg_2Ni cannot be simply obtained by casting as a phase separation occurs during solidification.

Mechanical alloying (MA) method has been widely used to produce nanostructured alloys or composites, especially to produce amorphous and nanocrystalline Mg_2Ni alloys. However, it usually takes a long time to prepare alloys by the MA method, the sample can be contaminated during the milling process, oxidation occurs even in a protective atmosphere [7]. Moreover, it is difficult to obtain a homogenous sample by the MA method [8]. It is known that nano- or ultrafine particles have a lowered melting point because of the small size and large specific surface area of the particles, which implies a possibility of preparing the Mg_2Ni compound by using magnesium and nickel nanoparticles. Lio et al. synthesized Mg_2Ni intermetallic nanoparticles by a two-step method [9]. First, Mg and Ni nanoparticles were prepared by hydrogen plasma-metal reaction. Second,

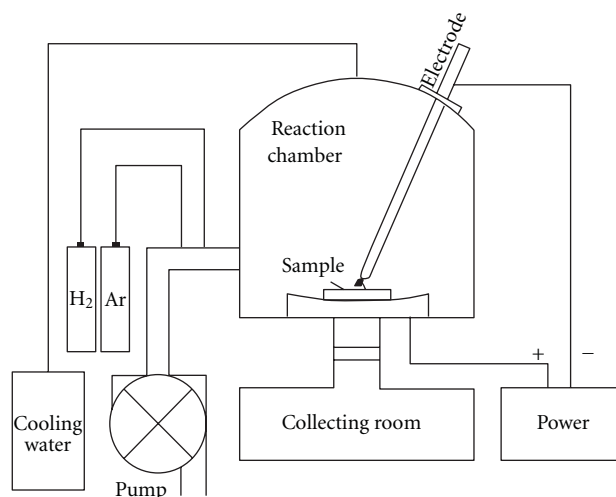


FIGURE 1: Schematic illustration of the DC arc plasma evaporation equipment.

the mixture of Mg and Ni nanoparticles in a 2:1 molar ratio was compressed into a pellet and was heated up to 623 K under a hydrogen pressure of about 40 bar to react with hydrogen. It is established that at 553 K and 3 MPa hydrogen pressure, Mg_2NiH_4 can be generated, and Mg_2Ni intermetallic phase was obtained with high productivity after hydrogen desorption. The obtained Mg_2Ni compound has excellent hydrogen storage properties and can absorb hydrogen to its maximum capacity in the first cycle at a high speed without any activation. Its excellent performance is due to the ultrafine particle size, large surface area, and internal defects.

In this paper, we have attempted the direct preparation of Mg-Ni composite ultrafine particles through vapor state reactions by using a DC arc plasma method. This process is similar to the in-flight plasma processes, which injected the metal powders into the plasma flame leaving the gasification. In this process, the metal vapor cooled down rapidly after leaving the plasma flame, reached saturation, then condensed and formed nano- or ultrafine powders [10].

2. Experimental

2.1. Sample Preparation. The Mg-Ni ultrafine powders were prepared using an arc plasma evaporation apparatus. Figure 1 shows a schematic illustration of the experimental equipment. It mainly consists of a reaction chamber and a collection room. Mg-Ni ultrafine particles were prepared by arc evaporation of the mixture of magnesium and nickel powders. Commercially available Mg and Ni powders with 99.9 wt% in purity and 100 μm in particle size were delicately mixed in a molar ratio of 1:2. The mixed powders were then compressed at room temperature to form cylinders with 10 mm in diameter and 7 mm in height by an uniaxial compressor under a pressure of 25 MPa. These cylinders, as anode materials, were put into the reaction chamber filled with mixed 0.75 atm Ar + 0.05 atm H_2 gas after the chamber

was evacuated to 5×10^{-2} Pa. The DC current is set at 140 A during arc evaporation. Before the Mg-Ni ultrafine particles were taken out from the reaction chamber, they were slowly passivated with a mixture of argon and air to prevent the particles from burning in air.

2.2. Characterization. The phase identification of the Mg-Ni nanoparticles before and after hydrogen absorption was carried out by X-ray diffraction (XRD) using a D/max 2550VL/PCX apparatus equipped with Cu-K α radiation source. The morphology and microstructure of the powders were observed by using a JEM-2100 transmission electron microscope (TEM), operated at 200 kV. The composition of the Mg-Ni powders was analyzed by inductive coupled plasma emission spectrometer (ICP). A conventional Sieviet-type pressure-composition-temperature (P-C-T) apparatus, which means measuring hydrogen content versus pressure by recording the change of gas pressure in a constant volume, was used to test the hydrogen sorption properties of the Mg-Ni ultrafine powders. The testing temperatures were set at 400°C, 375°C, 350°C and 325°C. The hydrogen desorption property of the prepared powders was analyzed by thermogravimetry/differential scanning calorimetry spectroscopy (TG/DSC) technique.

3. Results and Discussions

3.1. XRD Analysis. Figures 2(a), 2(b), and 2(c) show the XRD patterns of the as-prepared Mg-Ni ultrafine particles, the samples obtained after the hydrogen absorption and after desorption, respectively. From Figure 2(a), it is seen that the main phases of the Mg-Ni ultrafine particles prepared by DC arc plasma are Mg and Ni, with a small amount of MgO. Besides, the presence of Mg_2Ni and MgNi_2 phases is also detected. The peaks corresponding to MgNi_2 phase are fairly weak, indicating that the volume content of Mg_2Ni in the powders is very low. The MgO phase was formed when the Mg-Ni nanoparticles were passivated in the mixture of argon and air. The MgO layer at the surface of the magnesium particles can effectively prevent the further oxidation or even burning of the Mg particles when exposed to air. The existence of Mg_2Ni and MgNi_2 shows that the following reactions have occurred during the arc plasma evaporation:



These reactions occurred in vapor state depending on the local vapor concentrations of Mg and Ni. Indeed, Mg has much higher vapor pressure than Ni at the same temperature, resulting in the generation of a vapor rich in Mg during arc evaporation. ICP analysis shows that the average Mg and Ni content in the Mg-Ni ultrafine powders is 7:1 in molar ratio, much higher than the ratio 1:2 in the original mixture. However, the local vapor content may not be homogeneous during arc evaporation of the Mg-Ni mixture. Ni concentration might be higher than Mg in local regions inside the plasma. As a result, both reaction (1)

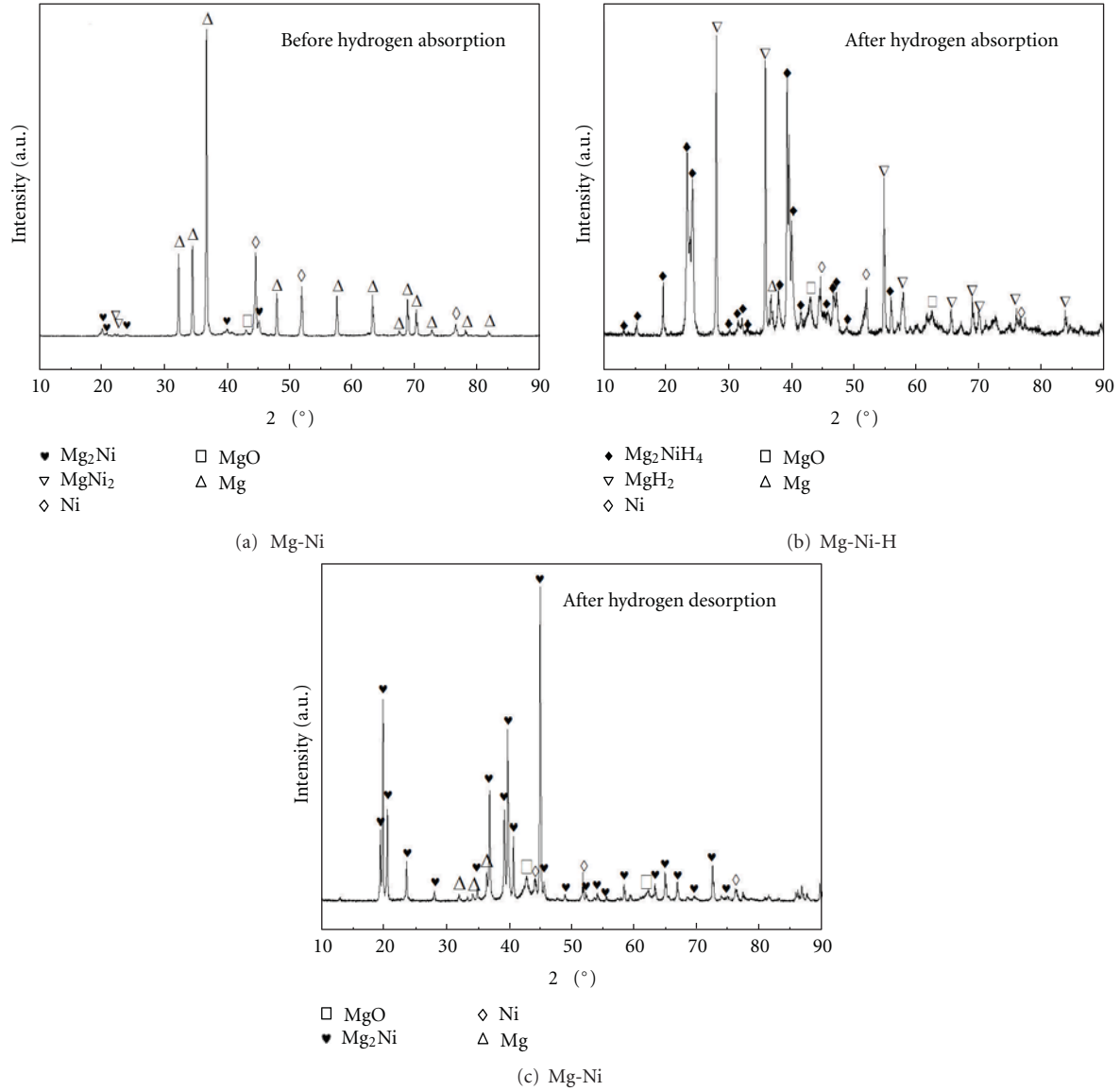


FIGURE 2: X-ray diffraction patterns of Mg-Ni ultrafine-particles (a), Mg-Ni ultrafine particles after hydrogen absorption at 400°C, 4 MPa, (b), and Mg-Ni ultrafine particles after hydrogen desorption (c).

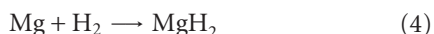
and reaction (2) could occur in the mixed vapor, leading to the formation of Mg₂Ni and MgNi₂ phases. As the vapor is highly rich in Mg, reaction (1) should be more important than reaction (2). As a result, the amount of Mg₂Ni should be higher than the amount of MgNi₂. The fact that the majority phases in the Mg-Ni ultrafine powders are pure Mg and Ni indicates that most of Mg and Ni vapors do not react with each other during evaporation. It has been established that the evaporation rate of metals plays a major role for the generation of the metal particles. According to the Ohno's model, the vapor generation rate of a metal through hydrogen plasma reaction method is proximately proportional to its reaction parameter, R_p , which can be expressed by the following equation:

$$R_p = \left(-\frac{\Delta H_r}{L_s} \right) \left[\frac{N_{H_2}(T)}{N_{H_2}(273)} \right], \quad (3)$$

where H_r is the reaction enthalpy between metal and hydrogen, L_s is the heat of vaporization of the metal at the temperature T , and $N_{H_2}(T)$ and $N_{H_2}(273)$ are densities of the hydrogen molecules in the metal at temperature T and 273 K. By inputting parameters for Mg and Ni into (3), it is estimated that $R_p = 1$ for Mg and $R_p = 0.17$ for Ni. The large difference in R_p values indicates that the evaporation rate for Ni is much lower than that for Mg. This is consistent with the ICP result for which the Ni content in the composite is lower than that in the mixed powders before arc evaporation.

From the XRD pattern in Figure 2(b), it can be seen that most of the Mg-Ni powders have transformed into MgH₂ and Mg₂NiH₄ hydrides after the hydrogen absorption at 400°C and 4 MPa. The mechanism for the formation of Mg₂NiH₄ hydride is thought to be the reaction (4)

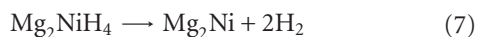
followed by reaction (5) occurred during the isothermal period:



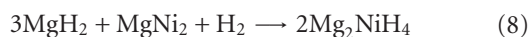
As the atomic ratio of Mg:Ni is 7:1 in the Mg-Ni ultrafine powders, the reactions (4) and (5) can be combined together into reaction (6). That is, when Mg-Ni ultrafine powders are completely hydrogenated, the molar ratio of MgH_2 to Mg_2NiH_4 should be around 5:1:



There is still a small amount of Mg phase observed in the sample after hydrogenation at 400°C, as seen in Figure 2(b). This is due to the fact that some relatively large Mg particles cannot be completely hydrogenated. It is observed from Figure 2(c) that after hydrogen desorption, MgH_2 decomposes completely and transforms into Mg, and Mg_2NiH_4 transforms into Mg_2Ni compound, as described by the following reaction:



This principle of the reactions (4), (5), and (7) is used to prepare Mg_2Ni compound by Shao et al. [12, 13]. Comparing Figures 2(a) and 2(b), it is worth noting that the diffraction peaks of MgNi_2 disappeared after hydrogen absorption. It is believed that MgNi_2 should react with MgH_2 to form Mg_2NiH_4 in the presence of high temperature and hydrogen atmosphere, as described by the following reaction:



3.2. TEM Observations of the Mg-Ni Ultrafine Particles.

Figures 3(a), 3(b), and 3(c) show typical bright field TEM micrographs of Mg-Ni composite powders before hydrogen absorption, the samples obtained after hydrogen absorption and after hydrogen desorption, respectively, with corresponding selected area electron diffraction (SAED) patterns. From Figure 3(a), it is observed that most of the particles have quasispherical shape with the particle size ranges from 50 to 600 nm. The corresponding SAED pattern consists of rings and overlapped dispersed spots. The rings are identified to be Mg and MgO phases. However, the spots are not indexed and could correspond to the Ni, Mg_2Ni , and MgNi_2 phases based on the result of XRD analysis (Figure 2(a)). Normally, Mg can be directly evaporated into gaseous atoms before melting in the high temperature plasma. This is due to the low melting point and small latent heat of evaporation for Mg. The fast vapor generation rate of the Mg results in the formation of relatively large particles [14]. After hydrogenation at 400°C in 4 MPa hydrogen atmosphere, MgH_2 and Mg_2NiH_4 phases formed in the composite. The typical morphology of these hydrides is shown in Figure 3(b). The particles became transparent having size in the range between 50 and 200 nm, smaller than the Mg particles

shown in Figure 3(a). In the corresponding SAED pattern, diffracted rings belonging to MgH_2 , Mg_2NiH_4 , MgO, and Mg phases can be detected. It is found from Figure 3(c) that after 4 hydrogen absorption and desorption cycles, those large Mg particles have been cracked and broken into smaller particles. The corresponding SAED pattern is mainly composed of well-defined rings belonging to pure Mg. Besides this, MgO and Mg_2Ni are also identified. Compared with that of the as-prepared particles obtained using the same SAED aperture (Figure 3(a)), it indicates the grain refinement of Mg particles after hydrogen sorption cycles. The grain refinement of Mg particles is expected to benefit from the hydrogen storage properties owing to the increased surface areas and reduced diffusion length for hydrogen. As a consequence of the reduction in particle size, fresh surface was generated during the hydriding/dehydriding cycles. The presence of new surfaces makes the Mg particles easier to be oxidized. As a result, the amount of MgO increases after hydrogen sorption cycles, as can be observed from the comparison between diffraction peaks of MgO phase in Figures 2(c) and 2(a).

3.3. Hydrogen Storage Properties. Figure 4 shows the P-C-T curves of the hydrogen absorption-desorption processes for the Mg-Ni ultrafine particles at 400°C, 375°C, 350°C, and 325°C. The data obtained from the P-C-T measurements are summarized in Table 1. Two plateaus of absorption and desorption are clearly visible on each profile. According to the XRD results given above, two types of hydrides, MgH_2 and Mg_2NiH_4 , formed after hydrogenation. Therefore, the two plateaus of the absorption and desorption are attributed to the formation and decomposition of MgH_2 and Mg_2NiH_4 . According to previous investigations on the Mg-rich Mg-Ni composite materials, the low plateaus are due to hydriding and dehydriding of Mg, while the high plateaus are the results of hydriding and dehydriding of Mg_2Ni [15, 16]. The maximum hydrogen absorption capacities at 400, 375, 350, and 325°C are 3.16, 3.05, 2.97, and 2.96 wt%, respectively, which are even lower than the theoretical value of 3.6 wt% for Mg_2Ni . This is due to the existence of MgO, the residual Mg and Ni in the hydrided Mg-Ni composite, as shown in Figure 2(b). Indeed, some large magnesium particles cannot be completely hydrogenated. From these PCT data, the van't Hoff plots ($\ln P$ versus $1000/T$) for the Mg-Ni composite are drawn in Figure 5. According to the linear fitting lines from the experimental data, the van't Hoff equations for the hydrogenation are $\ln(P_{\text{low}}) = -10/T + 15.16$ for Mg and $\ln(P_{\text{high}}) = -7.77/T + 12.27$ for Mg_2Ni . The van't Hoff equations for the dehydrogenation are $\ln(P_{\text{low}}) = -9.31/T + 13.84$ for Mg and $\ln(P_{\text{high}}) = -7.96/T + 12.23$ for Mg_2Ni . Therefore, the obtained values of the hydride formation enthalpies (ΔH_{ab}) are -83.1 kJ/mol for Mg and -64.6 kJ/mol for Mg_2Ni , while the dehydrogenation enthalpies (ΔH_{de}) are 77.4 kJ/mol for Mg and 66.2 kJ/mol for Mg_2Ni . These hydrogenation and dehydrogenation enthalpies of Mg and Mg_2Ni phases agree well with the values reported in the literature, for example, about -66.3 kJ/mol H_2 for hydrogenation of Mg_2Ni [10, 17] and -74.5 kJ/mol H_2 for hydrogenation of Mg [18].

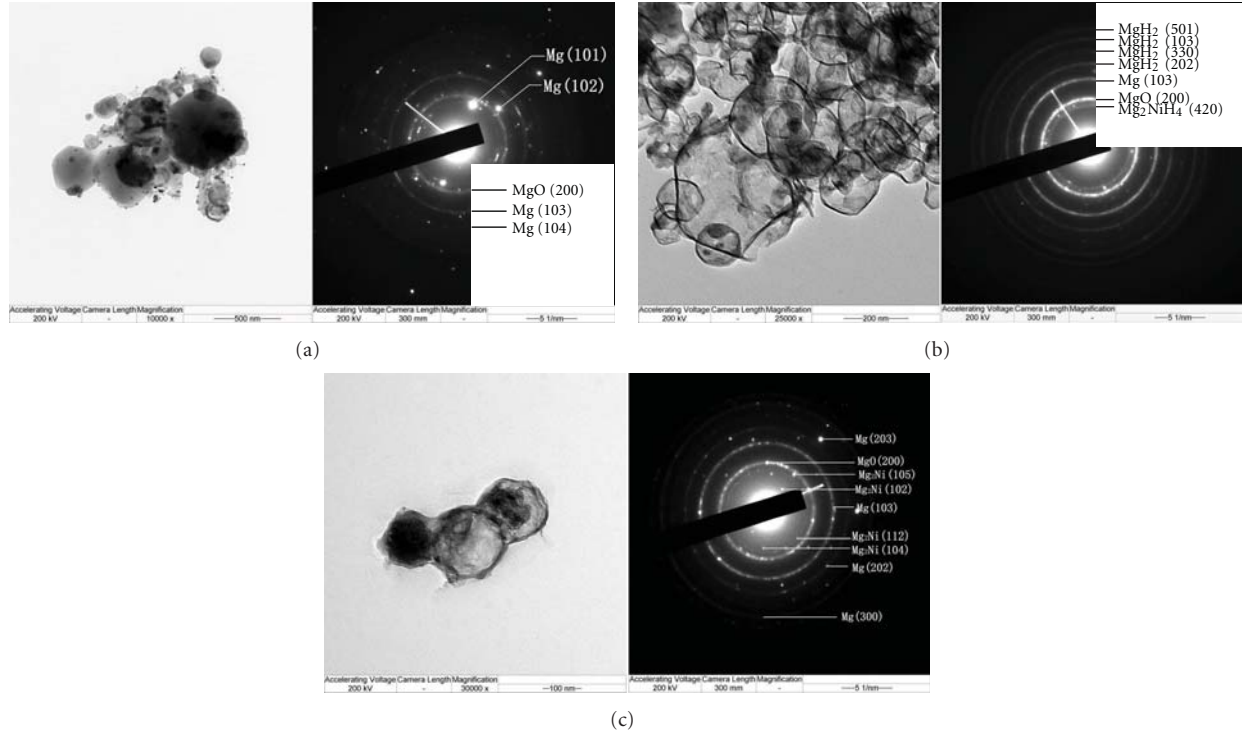


FIGURE 3: Bright field TEM micrographs of Mg-Ni nanoparticles before hydrogen absorption with SAED patterns inset (a), after hydrogen absorption with SAED patterns inset (b), and after hydrogen desorption with SAED patterns inset (c).

TABLE 1: The data of P-C-T tests.

Temperature/ $^{\circ}\text{C}$	Maximum H ₂ absorption/wt%	Low plateau of absorption/MPa	Low plateau of desorption/MPa	High plateau of absorption/MPa	High plateau of desorption/MPa
325	2.96	0.195	0.173	0.464	0.338
350	2.97	0.433	0.329	0.840	0.570
375	3.05	0.792	0.645	1.347	0.995
400	3.16	1.259	0.946	1.974	1.457

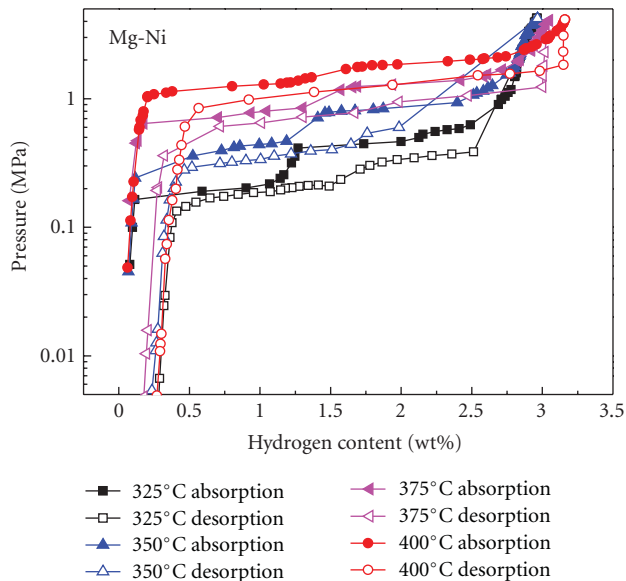


FIGURE 4: P-C-T curves of Mg-Ni ultrafine particles measured at 400°C, 375°C, 350°C and 325°C.

Figure 6 shows the TG/DSC curves of the hydrided Mg-Ni composite obtained in 4 MPa hydrogen atmosphere at 400°C. It is observed that three endothermic peaks appeared on the DSC curve measured from room temperature to 500°C. The small peak in the temperature range between 235°C and 250°C comes from the phase transformation of Mg₂NiH₄ from its low temperature form to its high temperature form [19]. While in the same temperature range, TG curve does not show any mass loss. Two strong endothermic peaks in the high temperature range between 365°C and 425°C are observed on the DSC curve together with a mass loss of 3.3 wt%. They result from the dehydriding of Mg₂NiH₄ and MgH₂. In order to understand the dehydriding processes of the hydrogenated Mg-Ni composite, a partially hydrogenated sample is prepared and studied by using DSC technique. The sample is hydrogenated at 350°C with 0.89 wt% of hydrogen absorption. Figure 7 shows the XRD pattern of the partially hydrogenated composite. From Figure 7, one can see that both MgH₂ and Mg₂NiH₄ phases exist after absorbing 0.89 wt% of hydrogen. The intensity of peaks from MgH₂ is relative higher than that of the Mg₂NiH₄ phase, indicating that the main product in this partially

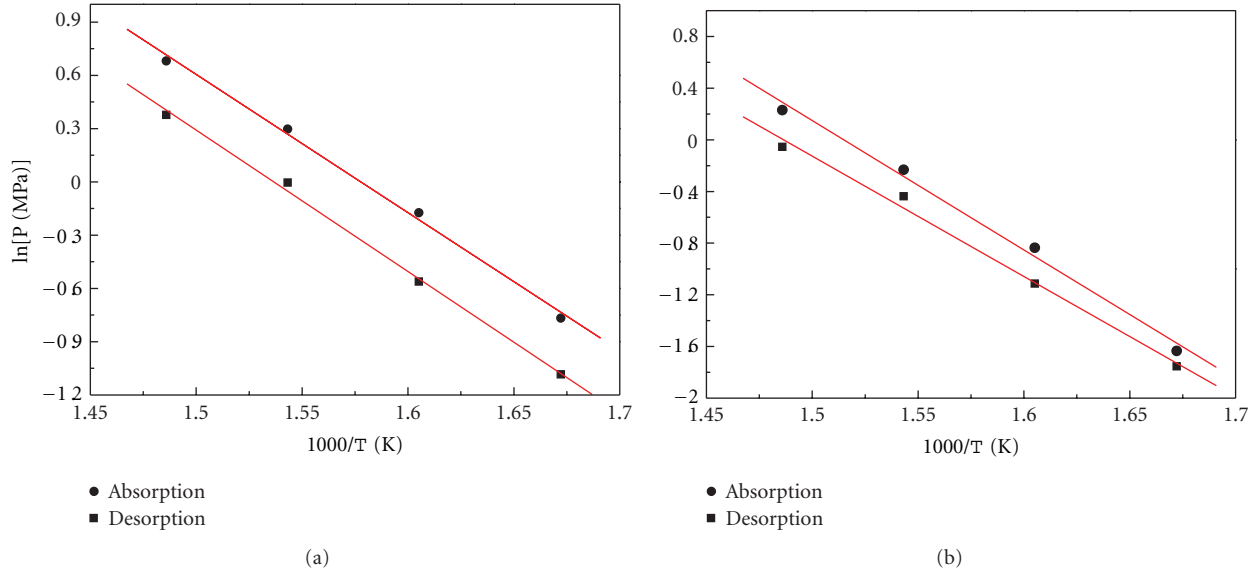


FIGURE 5: Van't Hoff plots based on the low plateaus (a) and high plateaus (b) on PCT curves for hydrogenation and dehydrogenation of the Mg-Ni composite.

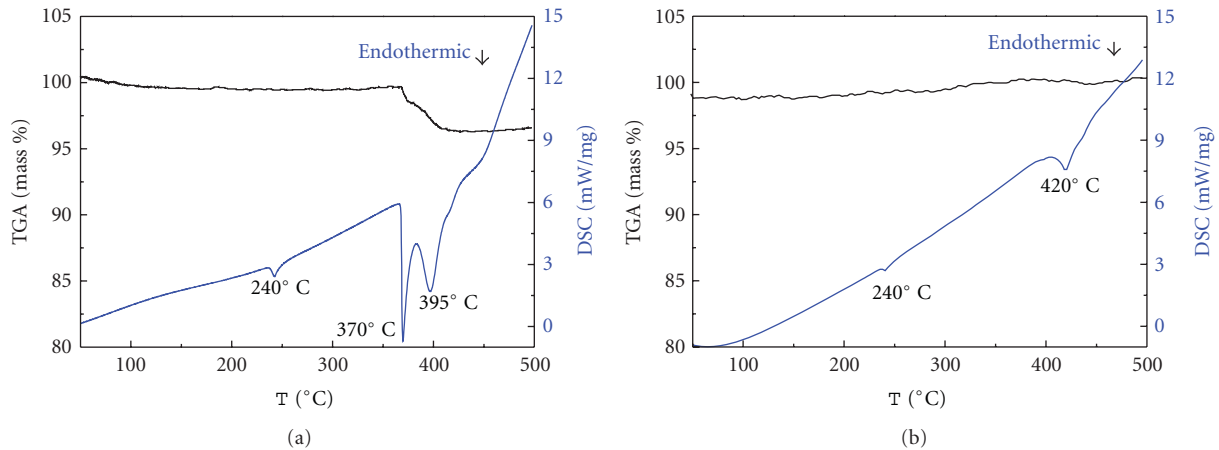


FIGURE 6: TG/DSC curves of the hydrogenated Mg-Ni composite samples (a) after absorbing hydrogen in 4 MPa hydrogen atmosphere at 400°C and (b) after absorbing 0.89 wt% of hydrogen at 350°C.

hydrogenated sample is MgH_2 . Therefore, the hydrogenation enthalpy calculated from the lower plateaus on the P-C-T curves actually comes from the formation of both MgH_2 (majority) and Mg_2NiH_4 (minority) phases. Figure 6(b) shows the TG/DSC curves of the partially hydrided Mg-Ni composite. In Figure 6(b), two peaks are visible. A very weak endothermic peak appeared at 240°C, which corresponds to the phase transformation of Mg_2NiH_4 . The other endothermic peak, with the onset point at 390°C and the peak point located at 420°C, must come from the dehydriding of MgH_2 . Therefore, the endothermic peak located at 370°C observed in Figure 6(a) is confirmed from the dehydriding reaction of $\text{Mg}_2\text{NiH}_4 \rightarrow \text{Mg}_2\text{Ni} + 2\text{H}_2$ while that of 395°C is from the dehydriding reaction of $\text{MgH}_2 \rightarrow \text{Mg} + \text{H}_2$. It is worth noting here that the dehydriding temperature of MgH_2 in the

fully hydrogenated powders is slightly lower than the partially hydrogenated powders. Also, the measured dehydrogenation enthalpy for MgH_2 (83.1 kJ/mol H_2) is slightly higher than its formation enthalpy (77.4 kJ/mol H_2). XRD analysis showed that the difference between the partially hydrogenated Mg-Ni powders and fully hydrogenated powders lies in the amount of Mg_2NiH_4 phase. Therefore, the Mg_2NiH_4 phase may play a role for the dehydriding of MgH_2 in the hydrogenated Mg-Ni composite powders. During dehydriding process, Mg_2NiH_4 decomposes prior to the MgH_2 . The decomposition of Mg_2NiH_4 into nanostructured Mg_2Ni may act as “hydrogen channels” for the decomposition of MgH_2 . Similar phenomena were also observed in Mg- Nb_2O_5 system for which the Nb_2O_5 act as hydrogen channels for hydrogen sorption of Mg [20, 21].

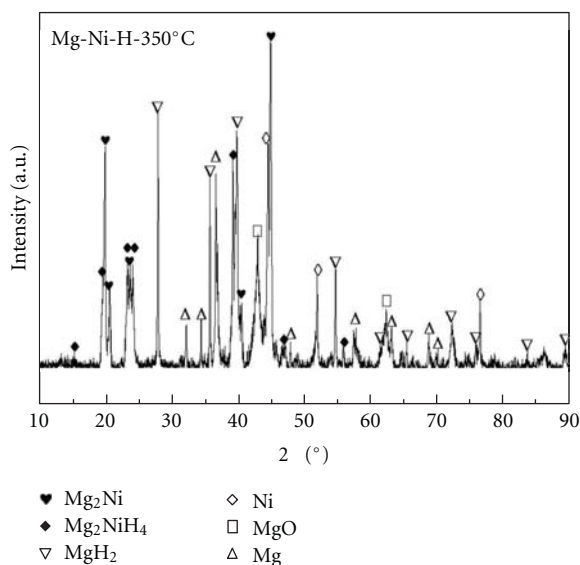


FIGURE 7: XRD pattern of the Mg-Ni particles after absorbing 0.89 wt% of hydrogen at 350°C.

4. Conclusions

Mg-rich Mg-Ni ultrafine powders were prepared through a DC arc plasma method. The results showed that Mg_2Ni and MgNi_2 phases could be obtained directly from the vapor state reactions between Mg and Ni vapors, depending on the local vapor content in the reaction chamber. After hydrogenation, a nanostructured $\text{MgH}_2 + \text{Mg}_2\text{NiH}_4$ hydrogen storage composite could be generated from the Mg-Ni ultrafine powders. After dehydrogenation, MgH_2 and Mg_2NiH_4 decomposed into nanograined Mg and Mg_2Ni , respectively. The hydrogenation enthalpy and dehydrogenation temperature of MgH_2 in the composite are significantly reduced. TG/DSC and XRD analyses on the fully hydrogenated sample and partially hydrogenated sample showed that Mg_2NiH_4 phase may play a catalytic role in the dehydriding process of the hydrogenated Mg ultrafine particles.

Acknowledgments

Professor J. Zou would like to acknowledge the financial support from Research Funds for the Doctoral Program of Higher Education of China (no. 20100073120007) and from Shanghai Education Commission (no. 12ZZ017). This work is partly supported by projects from the Science and Technology Committee of Shanghai no. 10JC1407700, no. 11ZR1417600, and no. 10dz2211000 and “Pujiang” project no. 11PJ1406000. This work was also partially supported by the French-Chinese collaboration project “XU Guangqi” (convention no. 27847SC).

References

- [1] H. Y. Shao, Y. T. Wang, H. R. Xu et al., “Preparation of Mg-based hydrogen storage materials from metal nanoparticles,” *Journal of Alloys and Compounds*, vol. 465, no. 1-2, pp. 527–533, 2000.
- [2] T. Z. Si, D. M. Liu, and Q. A. Zhang, “Microstructure and hydrogen storage properties of the laser sintered Mg_2Ni alloy,” *International Journal of Hydrogen Energy*, vol. 32, no. 18, pp. 4912–4916, 2007.
- [3] J. X. Zou, X. Q. Zeng, Y. J. Ying, P. Stephane, and W. J. Ding, “Preparation and hydrogen sorption properties of a nanostructured Mg Based Mg-La-O composite,” *International Journal of Hydrogen Energy*, vol. 37, no. 17, pp. 13067–13073, 2012.
- [4] N. Hanada, T. Ichikawa, and H. Fujii, “Catalytic effect of Ni nano-particle and Nb oxide on H-desorption properties in MgH_2 prepared by ball milling,” *Journal of Alloys and Compounds*, vol. 404–406, pp. 716–719, 2005.
- [5] T. B. Massalski, Ed., *Binary Alloy Phase Diagram*, American Society for Metals, 1986.
- [6] A. A. Nayeab-Hashemi and J. B. Clark, “The Mg–Ni (Magnesium–Nickel) system,” *Journal of Phase Equilibria*, vol. 6, no. 3, pp. 238–244, 1985.
- [7] C. C. Koch, “Synthesis of nanostructured materials by mechanical milling: problems and opportunities,” *Nanostructured Materials*, vol. 9, no. 1–8, pp. 13–22, 1997.
- [8] J. Huot, H. Enoki, and E. Akiba, “Synthesis, phase transformation, and hydrogen storage properties of ball-milled $\text{TiV}_{0.9}\text{Mn}_{1.1}$,” *Journal of Alloys and Compounds*, vol. 453, no. 1-2, pp. 203–209, 2008.
- [9] T. Liu, H. Y. Shao, and X. G. Li, “Oxidation behaviour of Fe_3Al nanoparticles prepared by hydrogen plasma-metal reaction,” *Nanotechnology*, vol. 14, no. 5, pp. 542–545, 2003.
- [10] J. F. Bisson and C. Moreau, “Effect of direct-current plasma fluctuations on in-flight particle parameters: part II,” *Journal of Thermal Spray Technology*, vol. 12, no. 2, pp. 258–264, 2003.
- [11] S. Ohno and M. Uda, “Generation rate of ultrafine metal particles in “hydrogen plasma-metal” reaction,” *Journal of the Japan Institute of Metals*, vol. 48, no. 6, pp. 640–646, 1984.
- [12] H. Y. Shao, H. R. Xu, Y. T. Wang, and X. G. Li, “Preparation and hydrogen storage properties of Mg_2Ni intermetallic nanoparticles,” *Nanotechnology*, vol. 15, no. 3, pp. 269–274, 2004.
- [13] H. Y. Shao, T. Liu, X. G. Li, and L. F. Zhang, “Preparation of Mg_2Ni intermetallic compound from nanoparticles,” *Scripta Materialia*, vol. 49, no. 6, pp. 595–599, 2003.
- [14] V. Bérubé, G. Radtke, M. Dresselhaus, and G. Chen, “Size effects on the hydrogen storage properties of nanostructured metal hydrides: a review,” *International Journal of Energy Research*, vol. 31, no. 6-7, pp. 637–663, 2007.
- [15] G. Liang, S. Boily, J. Huot, A. V. Neste, and R. Schulz, “Hydrogen absorption properties of a mechanically milled Mg-50 wt.% LaNi_5 composite,” *Journal of Alloys and Compounds*, vol. 268, no. 1-2, pp. 302–307, 1998.
- [16] J. J. Reilly and R. H. Wiswall, “Reaction of hydrogen with alloys of magnesium and nickel and the formation of Mg_2NiH_4 ,” *Inorganic Chemistry*, vol. 7, no. 11, pp. 2254–2256, 1968.
- [17] T. R. Jensen, A. Andreasen, T. Vegge et al., “Dehydrogenation kinetics of pure and nickel-doped magnesium hydride investigated by in situ time-resolved powder X-ray diffraction,” *International Journal of Hydrogen Energy*, vol. 31, no. 14, pp. 2052–2062, 2006.
- [18] H. Y. Shao, Y. T. Wang, H. R. Xu, and X. G. Li, “Hydrogen storage properties of magnesium ultrafine particles prepared by hydrogen plasma-metal reaction,” *Materials Science and Engineering B*, vol. 110, no. 2, pp. 221–226, 2004.

- [19] L. Li, T. Akiyama, and J. I. Yagi, "Reaction mechanism of hydriding combustion synthesis of Mg_2NiH_4 ," *Intermetallics*, vol. 7, no. 6, pp. 671–677, 1999.
- [20] K. F. Aguey-Zinsou, J. R. Ares Fernandez, T. Klassen, and R. Bormann, "Effect of Nb_2O_5 on MgH_2 properties during mechanical milling," *International Journal of Hydrogen Energy*, vol. 32, no. 13, pp. 2400–2407, 2007.
- [21] G. Barkhordarian, T. Klassen, and R. Bormann, "Fast hydrogen sorption kinetics of nanocrystalline Mg using Nb_2O_5 as catalyst," *Scripta Materialia*, vol. 49, no. 3, pp. 213–217, 2003.